Institute of Paper Science and Technology

ANNUAL RESEARCH REVIEW

CHEMICAL RECOVERY

March 23, 1992

Atlanta, Georgia

INSTITUTE OF PAPER SCIENCE AND TECHNOLOGY

Antitrust Notice

Guidelines for Meetings

Neither the Institute of Paper Science and Technology nor any committee or activity of the Institute shall be used or include discussions for the purpose of bringing about or attempting to bring about any understanding or agreement, written or oral, formal or informal, expressed or implied, among competitors with regard to prices, terms or conditions of sale, distribution, volume of production, or allocation of territories, customers or supplies.

No IPST activity shall involve exchange or collection and dissemination among competitors of any information regarding prices, pricing methods, costs of production, sales, marketing, or distribution.

Neither IPST nor any committee thereof shall make any effort to bring about the standardization of any product for the purpose of or with the effect of preventing the manufacture or sale of any product not conforming to a specified standard.

The Institute does not become involved in any product standards or endorsements. IPST policy as a tax exempt educational institution expressly precludes the establishment of product standards or the endorsement of any product or process and general provisions incorporated in IPST research contracts so state.

Rev. 10/90

NOTICE & DISCLAIMER

The Institute of Paper Science and Technology (IPST) has provided a high standard of professional service and has put forth its best efforts within the time and funds available for this project. The information and conclusions are advisory and are intended only for internal use by any company who may receive this report. Each company must decide for itself the best approach to solving any problems it may have and how, or whether, this reported information should be considered in its approach.

IPST does not recommend particular products, procedures, materials, or service. These are included only in the interest of completeness within a laboratory context and budgetary constraint. Actual products, procedures, materials, and services used may differ and are peculiar to the operations of each company.

In no event shall IPST or its employees and agents have any obligation or liability for damages including, but not limited to, consequential damages arising out of or in connection with any company's use of or inability to use the reported information. IPST provides no warranty or guaranty of results.

INSTITUTE OF PAPER SCIENCE AND TECHNOLOGY

Atlanta, Georgia

ANNUAL RESEARCH REVIEW

CHEMICAL RECOVERY

MARCH 23, 1992

TABLE OF CONTENTS

KRAFT BLACK LIQUOR DELIVERY SYSTEMS
PROJECT 3657-2

COMBUSTION OF BLEACH PLANT SOLIDS
PROJECT 3671

VALIDATED KRAFT RECOVERY
FURNACE MODELING CAPABILITY
PROJECT 3605

SIMULATION

EXPERIMENTAL

PROJECT 3657-2

KRAFT BLACK LIQUOR DELIVERY SYSTEMS

RESEARCH REVIEW

MARCH 23, 1992

H. Jeff Empie
Steven J. Lien
Douglas Samuels
Wen Rui Yang

TECHNICAL PROGRAM REVIEW REPORT

PROJECT TITLE:	Kraft Black Liquor Delivery Systems (Funded By U.S. Department of Energy)
PROJECT STAFF:	H. Jeff Empie, Steve Lien, Doug Samuels, Wen Rui Yang
BUDGET (FY 91-92):	$350,000
REPORTING PERIOD:	April '91 - March '92
DIVISION:	Chemical & Biological Sciences
PROJECT NO.:	3657-2

OBJECTIVE: Develop new and improved black liquor spraying nozzles by understanding the characteristics of spray behavior, enabling the fraction of undersize droplets to be reduced in order to avoid carryover and pluggage and facilitating the firing of higher solids liquors.

GOAL: Increase recovery boiler throughput and operating efficiency through improved liquor spraying technology at moderate capital cost.

PRIOR RESULTS: Early results were obtained on the performance of the three basic types of black liquor spray nozzles: the splashplate, the swirl cone, and the U- or V-jet. Data were presented on the flow and pressure drop characteristics of two of these nozzle types, the B&W splashplate and the SS U- and V-jets. Flow coefficient correlations for hot and cold black liquor were developed. The correlating parameter was Reynolds Number based upon the minimum flow diameter.

The formation of droplets from a black liquor stream required the prior formation of a fluid sheet by the nozzle. The ultimate droplet size could be directly related to the initial sheet thickness and velocity. Sheet thickness, and therefore liquor droplet size, were found to increase with liquor viscosity (and hence black liquor solids) for the B&W splashplate nozzle.

Data on droplet size distributions from a B&W splashplate nozzle and a CE swirl cone nozzle were obtained. Droplet size showed a weak dependence on liquor velocity and fluid physical properties. Furthermore, the size distribution was almost the same for all nozzles when the size data were normalized by dividing the actual droplet size by the mass median diameter.

Assembly of the new black liquor spray facility in Atlanta was completed, including installation of the spray chamber, viscometer, all of the piping, waste liquor storage tanks, a gas scrubber system, and all of the electrical sensor and control wiring. A data acquisition system was also connected so that information on liquor conditions is automatically recorded.

Windows on the front and back of the chamber were installed to allow the spray pattern to be videotaped. Lights and a translucent plexiglas screen are used to back-light the droplets. The high-speed video camera was tested and appeared to provide an adequate recording for the image analyzer, even with water. Black liquor produces an excellent high-contrast image.

Image analysis techniques have been developed for generating good, clear, two-dimensional representations of black liquor sprays from the raw video images. The use of image math and filters to remove background variation and noise resulting in enhanced video image quality was detailed.

A series of trials was conducted at James River's Camas Mill to study black liquor sprays in a recovery furnace environment. This was a joint effort between the Institute of Paper Science and Technology and James River Corp. High-speed video images of sprays were taken through a gun port on Camas' #4 Recovery Boiler. Three different nozzles were operated at two levels of liquor flow and fired liquor temperature. The major conclusions from analysis of furnace response data and high-speed video images of the sprays were (1,9):

1. Changing one nozzle and/or firing conditions for a short period of time did not produce significant changes in furnace operation as indicated by particulate count or lower furnace temperatures.
2. There was evidence of liquor sheet breakup by perforation which agrees with the findings of the IPST spray study. There was not a lot of evidence of wave fronts and associated breakup in the liquor sprays studied.
3. Differences in breakup between nozzles were seen in the video images; however, it was not possible to detect variation due to firing conditions. The video images were optically too dense to determine droplet size distribution by image analysis.

SUMMARY OF RESULTS SINCE LAST REPORT: A test series with three liquor nozzles (splashplate, swirlcone, and V-jet) has been completed, using a 3x3x3 matrix (solids of 50, 60, and 70%; viscosities of 270, 90, and 30 cP; and nozzle pressures of 15, 30, and 45 psi). Pressure vs. flow rate correlations have been derived as a function of Reynolds Number for the three primary nozzles. For the three tests at high viscosity (270 cP) and low pressure (15 psi), the flowrate was too low to produce sheet breakup. Another three tests at 70% solids and low viscosity could not be completed because the heat exchanger did not have the capacity to heat the liquor to well over the boiling point (265° F) in a single pass.

Video recordings of the spray pattern were made at four positions at distances of 34 to 44 inches from the nozzle. From the visual analysis of the video tape, it was apparent that the solids concentration of the black liquor had a strong effect on droplet formation. At low solids (50%), the majority of the drops were spherical, but at high solids (70%), most of the images were large, irregularly shaped drops connected to strings and filaments.

Several drop size distribution models have been tested to fit the experimental black liquor data; the best one continues to be the square root-normal distribution. This model has only two parameters, the mass median diameter and the standard deviation. The experimental data show that the ratio of mass median diameter to the square root of the standard deviation is essentially constant at a value of 0.2, and therefore that only one parameter is necessary to characterize the square root-normal model.

The ratio of mass median droplet diameter to nozzle diameter can be related to the product of Reynolds Number and Euler Number, each raised to some experimentally determined nonintegral power; similarly, Euler and Schmidt Numbers also correlate well. Both of these correlations can be broken down into a product of the individual physical parameters, each raised to some experimentally determined power. The design and operating parameters which most strongly influence mass median drop diameter are nozzle diameter and liquor density and velocity. Both density and velocity are related to the kinetic energy of the liquor leaving the nozzle, suggesting that the more energy that is dissipated, the smaller the median drop size. At high solids levels liquor viscosity becomes important. Finally, only velocity and temperature raised to appropriate powers were used in a correlation, with both operating variables showing drop size to decrease as either parameter increases.

A study of the behavior of spray nozzles at liquor temperatures above the boiling point was performed. A system of direct steam injection was installed so that adequate temperatures could be achieved. Three different nozzles were tested 65% and 68% solids and at temperatures ranging from 200° to 270° F. In general, as the temperature was increased, drop diameter gradually decreased; there was a transition temperature (above the boiling point) where the average drop size rapidly decreased by at least a factor of two, presumably due to flashing at the nozzle. This would result in a several-fold increase in the number of drops being fired into a furnace, increasing burning rates and possibly carryover rates.

Measurements were made of the local distribution of liquor flow in the spray pattern as a function of the angle from the sheet center line. Results for both the splashplate and V-jet nozzles show the mass flow distribution to be parabolic, with the maximum at the centerline and decreasing with increasing angle. Significance of this finding may be assessed by the recovery furnace model being developed at IPST, separately. Limited analysis of drop size as a function of angle from the sheet centerline showed no significant difference.

Present commercial black liquor nozzles do not provide a means for independently controlling droplet size distribution. The fluid dynamics of the spraying system is the main determining force; any significant change will require some externally applied forcing mechanism.

PLANNED ACTIVITY THROUGH FY '92:

- Complete analysis of drop size distribution data for three alternative liquors and make comparisons.
- Determine droplet formation characteristics for commercially available alternative nozzles (i.e. Delavan Raindrop ®) and compare with standard black liquor nozzle performance.

- Determine droplet formation characteristics for innovative spraying approaches ranging from modified splashplate designs to more complex configurations, such as vibratory assist.

- Examine less developed alternative liquor delivery systems featuring vortex shedding and impaction/coalescence.

- Secure DOE funding approval for two-year follow-up study to develop and commercialize most promising alternative technology identified in present study.

- Formulate and submit to DOE a research proposal which addresses the longer term goal of a commercial delivery system for high solids (i.e. 80%) black liquor. Extensive design modifications to the black liquor spraying equipment are anticipated.

PROJECT TITLE: KRAFT BLACK LIQUOR DELIVERY SYSTEMS
PROJECT NO: 3657-2

1.0 INTRODUCTION

1.1 OBJECTIVES

The research program detailed in this report represents an applied effort designed specifically to identify the optimum black liquor delivery system for the current kraft recovery boiler and to present it to the industry in a timely fashion. Only commercially viable (large capacity) delivery systems are being considered. Since the primary focus of this program is a system to deliver black liquor, a large number of experiments are being conducted with actual (well-characterized) liquors. The program will answer the following specific questions:

a. Exactly how good are the nozzles currently used for black liquor spraying?

b. Do other commercially available (off the shelf) spraying systems exist which perform better than liquor nozzles now in use?

c. Can vibratory assist or concepts from fluidics such as controlled vortex shedding be employed to develop significantly improved spraying systems?

d. Are there more radically different delivery systems not involving the spraying of droplets which offer the opportunity for quantum improvements in recovery boiler operations?

In order to answer these questions, the research program has the following main objectives:

a. To put in place a unique laboratory facility for the quantitative study of commercially viable black liquor nozzles which are tested with black liquors at typical operating conditions.

b. To quantify the performance (droplet size distribution, velocity, and mass distribution) of commercially available nozzles when spraying kraft black liquors at typical boiler conditions.

c. To test several potential techniques currently envisioned for improving the control of black liquor spray droplet size distribution with commercially viable nozzles.

d. To proceed beyond current spray technology to test several fundamentally different, but commercially viable, delivery systems.

This research effort will deliver the following:

a. A test facility capable of quantitatively assessing the performance of commercially viable spray systems while spraying kraft black liquors at typical boiler feed conditions.

b. The best commercial spray delivery system available with current technology.

c. An appraisal of the commercial viability of several fundamentally different black liquor delivery systems.

This past year has addressed "a" and "b" with details contained in this report.

2.0 REVIEW OF PAST PROJECT ACTIVITY

Early results were obtained on the performance of the three basic types of black liquor spray nozzles: the splashplate, the swirl cone, and the U- or V-jet. Data were presented on the flow and pressure drop characteristics of two of these nozzle types which allow judgment of the sensitivity of the flow to normal mill variations in liquor properties. Flow coefficient correlations for hot and cold black liquor were developed for two types of black liquor nozzles: the B&W splashplate and the SS U- and V-jets. The correlating parameter was Reynolds Number based upon the minimum flow diameter. Data were also presented on droplet size distribution. Considerations of nozzle stability with respect to flashing ahead of the nozzle showed that the minimum nozzle operating pressure would have to be significantly increased to suppress flashing ahead of the nozzle when firing high solids, viscous liquors.

The formation of droplets from a black liquor stream required the prior formation of a fluid sheet by the nozzle. The ultimate droplet size could be directly related to the initial sheet thickness and velocity. Sheet thickness, and therefore liquor droplet size, were found to increase with liquor viscosity (and hence black liquor solids) for the B&W splashplate nozzle. This change in nozzle performance at high solids should be mild enough to allow routine mill optimization of existing B&W nozzles without replacing them with a new design when changing to high solids firing.

Data on droplet size distributions from a B&W splashplate nozzle and a CE swirl cone nozzle were obtained. Droplet size did vary with operating conditions; however, it showed a weak dependence on liquor velocity and fluid physical properties. Furthermore, the size distribution was almost the same for all nozzles when the size data were normalized by dividing the actual droplet size by the mass median diameter.

Assembly of the new black liquor spray facility in Atlanta was completed, including installation of the spray chamber, viscometer, all of the piping, waste liquor storage tanks, a gas scrubber system, and all of the electrical sensor and control wiring. A data acquisition system was also connected so that information on liquor conditions is automatically recorded.

Windows on the front and back of the chamber were installed to allow the spray pattern to be videotaped. Lights and a translucent plexiglas screen are used to back-light the droplets. The high-speed video camera was tested and appeared to provide an adequate recording for the image analyzer, even with water. Black liquor produces an excellent high-contrast image.

Two issues were identified needing resolution before droplet analysis is possible: completeness of droplet breakup; and out-of-focus droplets. Because of the width of the spray pattern, the depth of field was too narrow to capture all of the drops in focus. The depth of field could be improved by reducing the aperture, but because of the requirement for a fast shutter speed, it was necessary to increase the light intensity to the chamber. The video data also indicated that the droplet formation process is not completed within the length of the spray chamber for all test conditions. This is especially true for the larger nozzles and at high viscosities. The length required for the drops to coalesce can be reduced by using smaller nozzles.

Image analysis techniques have been developed for generating good, clear, two-dimensional representations of black liquor sprays from the raw video images. The use of image math and filters to remove background variation and noise resulting in enhanced video image quality was detailed.

A series of trials was conducted at James River's Camas Mill to study black liquor sprays in a recovery furnace environment. This was a joint effort between the Institute of Paper Science and Technology and James River Corp. High-speed video images of sprays were taken through a gun port on Camas' #4 Recovery Boiler. Three different nozzles were operated at two levels of liquor flow and fired liquor temperature. The major conclusions from analysis of furnace response data and high-speed video images of the sprays were (1):

1. Changing one nozzle and/or firing conditions for a short period of time did not produce significant changes in furnace operation as indicated by particulate count or lower furnace temperatures.

2. There was evidence of liquor sheet breakup by perforation which agrees with the findings of the IPST spray study. There was not a lot of evidence of wave fronts and associated breakup in the liquor sprays studied.

3. Differences in breakup between nozzles were seen in the video images; however, it was not possible to detect variation due to firing conditions. The video images were optically too dense to determine droplet size distribution by image analysis.

4. The video equipment may prove to be a valuable industrial tool for rapid evaluation of nozzle performance in the field and for optimization of firing conditions.

3.0 DISCUSSION OF 1991 RESULTS

During the past year (Year 3 of the Black Liquor Delivery Systems Project), a large amount of experimental work was performed. The main test series during the third year was designed to produce drop size data over a wide range of test conditions. The variables studied include type of nozzle, solids content, liquor viscosity, and pressure at the nozzle. Three different nozzles were used in these tests: a B&W 12/45 splashplate; a CE swirl-cone; and a SS V-jet 11/65 nozzle.

For each test, video recordings were made of four different positions in the spray pattern. Analysis of these data provide a good starting point for the prediction of mean drop size and drop size distribution from the liquor properties and the other operating conditions.

Additional testing was performed to determine the correlation between the pressure drop and the velocity at the nozzle. This equation allows the nozzle flowrate to be estimated if the pressure and liquor conditions are known. This work (Section 3.2) used data from both test Series I and additional experimental work.

Next, tests were performed to determine the variations in flowrate around the spray angle of the nozzle. A sampling system was devised to collect liquor samples at 20 degree intervals around the perimeter of the spray. These data were measured for both the B&W splashplate and the Spraying Systems V-jet at various liquor pressures and viscosities. These data provide useful information for predicting the initial trajectory of the black liquor droplets.

A final series of higher temperature (above 230°F) tests has been performed, but the data have not been analyzed. These tests add some high solids and high temperature to the data set for test Series I. They also provide a set of data which describes what happens at temperatures above the boiling point of the black liquor.

All three of the liquors used during the past year were obtained from kraft mills pulping mostly southern softwood. Both of the first two liquors (BL #1 and BL #2) were from the Mead Corp. mill at Phenix City, Alabama mill, although they were collected several months apart. BL #1 was collected at the outlet of the concentrators at about 68% solids. Because the mill concentrators were down at the time, the second liquor (BL #2) was collected at an initial solids level near 50%. This liquor was then concentrated as needed in the spray chamber.

BL #1 was used primarily for start-up testing of the reconstructed spraying system, and therefore it was not submitted for chemical analysis. The second liquor (BL #2) was used for approximately three months of testing (Tests 7-A through 11-I). The failure of an electric heater which created a small hole on the bottom of the spray chamber made it necessary to transfer this black liquor supply to the waste holding tank.

At this point a new supply of mill liquor was collected from Inland Container's mill at Rome, GA and installed in the system. This black liquor supply (BL #3) was obtained at the outlet of the liquor gun feed pump and it includes the salt-cake make-up. In addition this liquor was concentrated in a direct contact evaporator. Tests 12-A through 18-I were performed with this liquor. In order to understand how these liquor supplies vary, samples were sent to an outside laboratory for chemical analysis. The results are listed in Table 1. As received samples of BL #2 and #3 were analyzed, and for BL #3 a sample after testing was completed was also analyzed to measure any change in the black liquor.

BL #3 shows high levels of carbonate (possible due to the use of direct contact evaporation in this mill). The carbonate shows a decrease after testing. There were hard deposits on the bottom of the spray chamber after the supply was removed, apparently due at least in part to carbonate precipitating out of solution.

The oxygen level in BL #3 showed a significant increase after testing, an indication of black liquor oxidation. This is confirmed by the drop in sulfide and a sharp increase in the thiosulfate level. Other than the carbonate and oxygen, no major changes in the composition of BL# 3 during the test series are apparent.

TABLE 1. CHEMICAL ANALYSIS OF BLACK LIQUORS.

Chemical Analysis of Black Liquors		(on a dry solids basis)	
Liquor No.	BLS #2	BLS #3	BLS #3
Liquor Type	Strong BL	Conc. BL with salt	Conc. BL after testing
Elemental Analysis			
Carbon (C) %	35.82	36.28	36.81
Hydrogen (H) %	3.37	3.36	4.66
Oxygen (O) %	31.50	32.82	36.12
Sulfur (S) %	5.66	4.37	4.44
Sodium (Na) %	20.67	18.28	16.12
Potassium (K) %	1.45	0.76	0.85
Chlorine (Cl) %	3.16	0.92	0.69
Total(%)	101.6	96.79	99.69
Sulfur ions			
Na2SO4 %	4.64	9.63	5.28
Na2SO3 %	<.04	0.06	<.04
Na2S2O3 %	5.20	0.66	7.32
Na2S %	2.05	4.68	4.08
Sulfur ions as S	3.99	4.37	5.84
NaCl %	2.89	1.51	1.14
Na2CO3 %	10.87	23.66	13.20
HHV (BTU/lb)	5888	5533	5453
Sample Solids (%)	48.9	61.5	62.9

3.1 VISCOSITY CORRELATIONS

One of the most important operating variables in the study of black liquor spray break-up and droplet formation is liquor viscosity. In addition to being a function of the specific liquor, viscosity is very closely related to the solids concentration and the temperature of the liquor. Viscosity and temperature data are routinely collected during the black liquor spraying tests. The viscosity is measured with an on-line Brookfield viscometer. Black liquor solids concentrations are determined from periodic liquor samples. Using these data, an equation was derived for each of the liquors tested, correlating the viscosity of black liquor to the percent solids and liquor temperature.

Several different types of correlations were tested. The form selected for the correlation equation is based on the reduced viscosity, that is the ratio of the black liquor viscosity to the viscosity of water at the same temperature. This type of correlation is typically used for polymer solutions. The percent solids and the temperature are also combined in a single term (T/SxT*). The equation for BL #1 is listed below.

$$Log\left(\frac{\mu}{\mu_w}\right)=\frac{1}{\left(65.62*\left(\frac{T}{SxT^*}\right)-0.6682\right)} \qquad (1)$$

where μ = liquor viscosity (cP)
μ_w = water viscosity at T (cP)
= 1000/ (36.6 xT - 10090)
S% = percent solids (%)
T = liquor temperature (K)
T^* = reference temperature (K)
= 373 K

The two correlations for BL #1 and BL #2 are plotted below as a function of (S%xT*/T) (Figure 1). The correlation lines for these first two liquors are very similar in shape and are nearly parallel, but the curve is shifted to a lower viscosity level for the second liquor. The difference in viscosity does not appear large on a log scale, but the viscosity of BL #1 is almost twice that of BL #2 at similar conditions. The correlation for BL #2 is:

$$Log\left(\frac{\mu}{\mu_w}\right)=\frac{1}{\left(69.67*\left(\frac{T}{SxT^*}\right)-0.689\right)} \qquad (2)$$

For BL #3 the correlation equation is:

$$Log\left(\frac{\mu}{\mu_w}\right)=\frac{1}{(46.49*(\frac{T}{SxT^*})-0.348)} \qquad (3)$$

There was more scatter in this set of viscosity data, possibly due to the presence of higher levels of undissolved salt particles in the black liquor which interfered with the rotating viscometer.

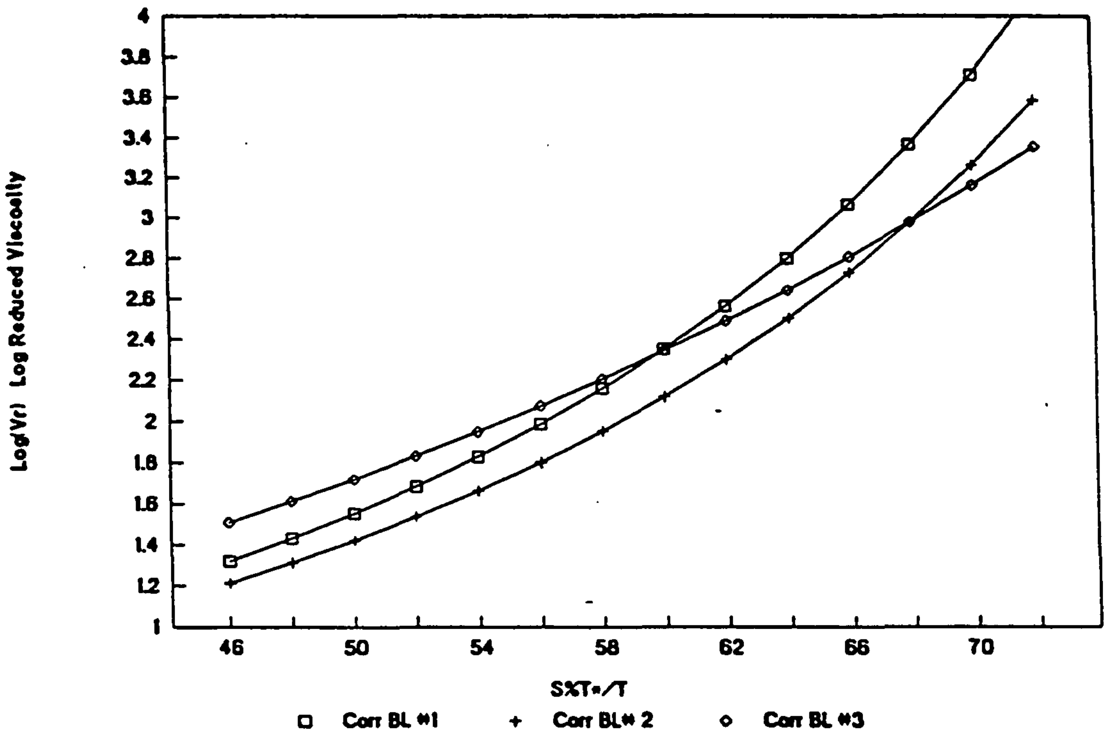

Figure 1. Viscosity Correlations for Black Liquors #1, #2, and #3.

The slope of the curve obtained for this liquor (BL #3) is much lower than the value for the two other liquors (Figure 1); i.e. the viscosity of this liquor is less sensitive to changes in solids or temperature. This is also apparent from the large change in the coefficients of the equation for BL #3.

In addition to providing a good correlation for viscosity data, these equations are very useful in the operation of the spray system. The current analytical method for determination of black liquor solids requires 24 hours to complete. These correlations allow calculation of the current solids concentration from the liquor temperature and viscosity, which are continuously monitored.

3.2 PRESSURE VS. FLOW RATE CORRELATIONS

Since the black liquor flow rate to a boiler is controlled by maintaining a constant header pressure, a correlation describing the relationship between nozzle pressure and black liquor flow rate at typical mill operating conditions will be very useful.

In the study of droplet formation from spray nozzles, testing has been carried out over a wide range of test conditions. Although most of these tests were performed to record high-speed video images of the spray pattern, data on the liquor conditions at the spray nozzle were also recorded via the computer-based data acquisition system. Some supplementary testing was also performed strictly to expand the data base for pressure vs. flow rate correlations.

In addition to various flow rates, the liquor has been sprayed over a range of solids content, viscosity, and temperature. Black Liquor supplies #2 and #3 were used to obtain these data. Table 2 below describes the range of conditions for the data analyzed.

Table 2. Range of Test Conditions for Pressure vs. Flow Rate Analysis

	Solids	Temp TC1	Viscosity VI1	Flow Rate F1	Velocity V	Reynolds Number Re	Pressure P1
	%	F	cP	gpm	m/sec		psi
Max.	45.8	89	27	3.8	2.1	69	4.0
Min.	72.8	249	541	52.7	19.9	8034	51.5

Six different nozzles were studied to develop these correlations (see Table 3.).

Table 3. Black Liquor Spray Nozzles

1. Splashplate Nozzles
   a. B&W 12/45
   b. B&W 15/52
   c. Tampella 18 mm
2. V-Jet Nozzles
   a. CE V-jet 15/
   b. SS V-jet 11/65
3. Swirl Cone Nozzles
   a. CE Swirl-Cone 12

From the Bernoulli equation for incompressible steady-state flow, an equation can be derived to describe the pressure drop across a flow nozzle.

$$\frac{\Delta P}{\rho}=\frac{V_n^2}{2}-\frac{V_o^2}{2}+h_f \tag{4}$$

where:

ΔP = *Pressure Drop(Pa)*

ρ = *Density (kg/m³)*

V_n = *Nozzle Velocity (m/sec)*

V_o = *Inlet Velocity (m/sec)*

h_f = *Friction loss (m²/sec²)*

By combining this with the continuity equation and a correlation for friction losses, this equation is modified to the following form:

$$\frac{\Delta P}{\rho}=\frac{V_n^2}{2}\left(1-\frac{D_n^4}{D_o^4}\right)+\frac{V_n^2}{2}f \tag{5}$$

where:

D_n = *Nozzle Diameter*

D_o = *Inlet Diameter*

f = *Friction factor*

This is then simplified to the final form by combining the last two terms into a single product of the velocity head times the flow coefficient.

$$\Delta P=\rho\frac{V_n^2}{2}C_f \tag{6}$$

where:

C_f = *Flow coefficient*

A similar type of correlation is used with head loss meters. For a venturi meter, C_f would generally be about 1.04. For an orifice meter the C_f value is about 2.7 for Reynolds Numbers over 20,000. Therefore we would expect our results to be somewhere in this range between 1 and 3.

Using measured pressure drop data and flow rates, along with the calculated nozzle diameter, C_f-values and Reynolds numbers were calculated for each test. These results were plotted and analyzed to determine the correlation between these numbers.

3.2.1 SPLASHPLATE NOZZLES

A graph showing C_f as function of the Reynolds number for all three of the splashplate nozzles is given in Figure 2. The curve is the same for all three nozzles. Using linear regression methods, the data were fit to an equation of the form below.

$$C_f = A + B*Re^c \tag{7}$$

The best fit for these data was found to be :

$$C_f = 1.24 + 458/Re^{0.9} \tag{8}$$

This correlation has an R-squared value of 0.912.

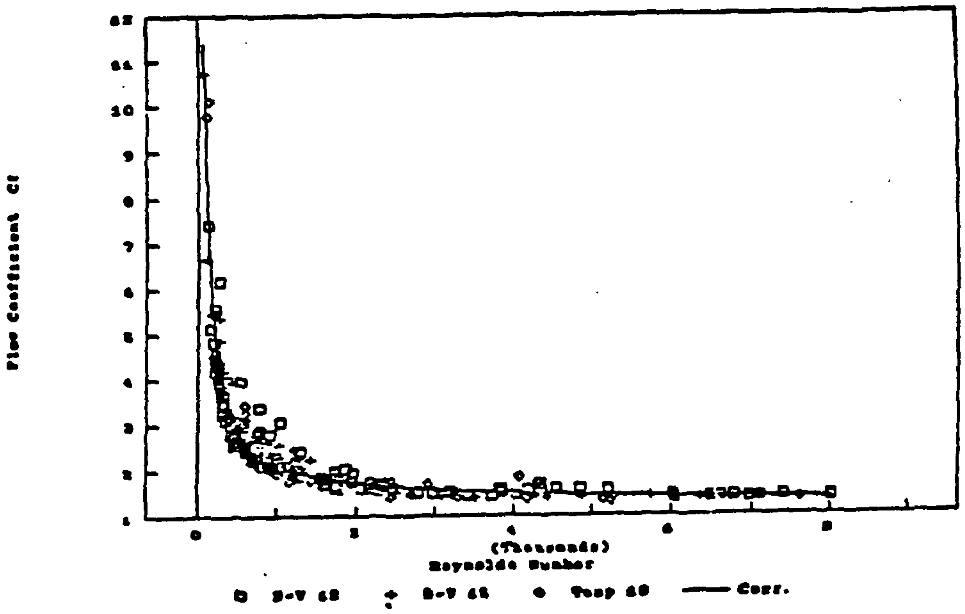

Figure 2. Flow Coefficient for Splashplate Nozzles.

3.2.2 V-JET NOZZLES

Two different V-jet nozzles were tested and two different correlations were obtained. The data are shown in Figure 3 below. For the smaller of the two nozzles, the SS V-jet 11/65, the relation between the flow coefficient and the Reynolds number is:

$$C_f = 1.09 + 540/Re^{1.35} \tag{9}$$

For the larger nozzle, the C_f was higher at all values of Re. The correlation for the CE V-jet 15 is:

$$C_f = 1.26 + 1089/Re^{1.35} \tag{10}$$

The R-squared values for these two equations were 0.697 and 0.779, respectively. The low R-squared values for these nozzles appear to be due to a sensitivity of C_f values to temperatures near the boiling point. At higher temperatures, the pressure drop is higher than what is predicted by the correlation.

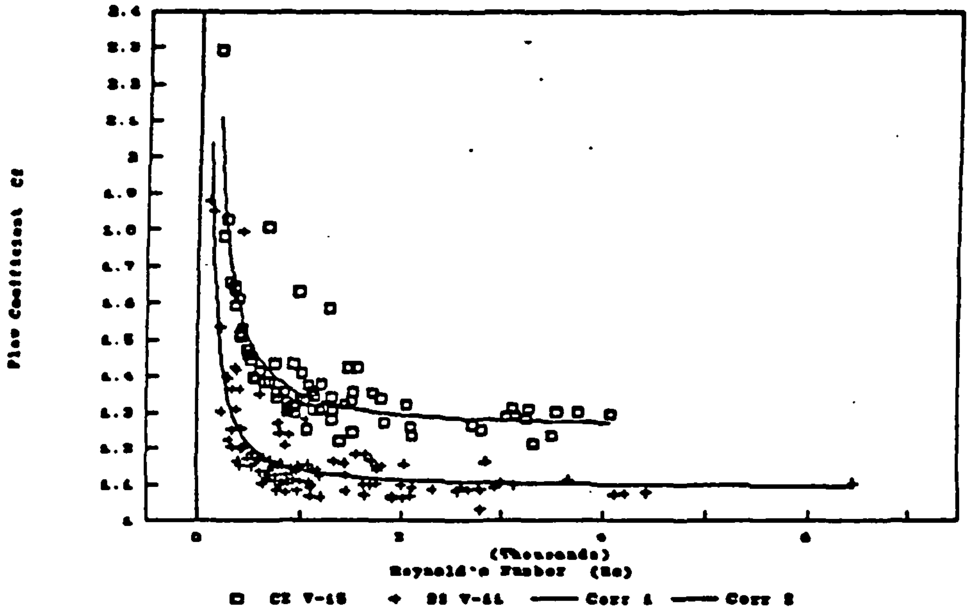

Figure 3. Flow Coefficient for V-jet Nozzles.

3.2.3 SWIRL-CONE NOZZLES

A good correlation between C_f and Re does not exist for the Combustion Engineering Swirl-cone nozzle. As shown in Figure 4, the flow coefficient is generally independent of the Reynolds Number, with an average value of 1.11. The variation in C_f does not correlate well with either the Reynolds Number or the liquor temperature.

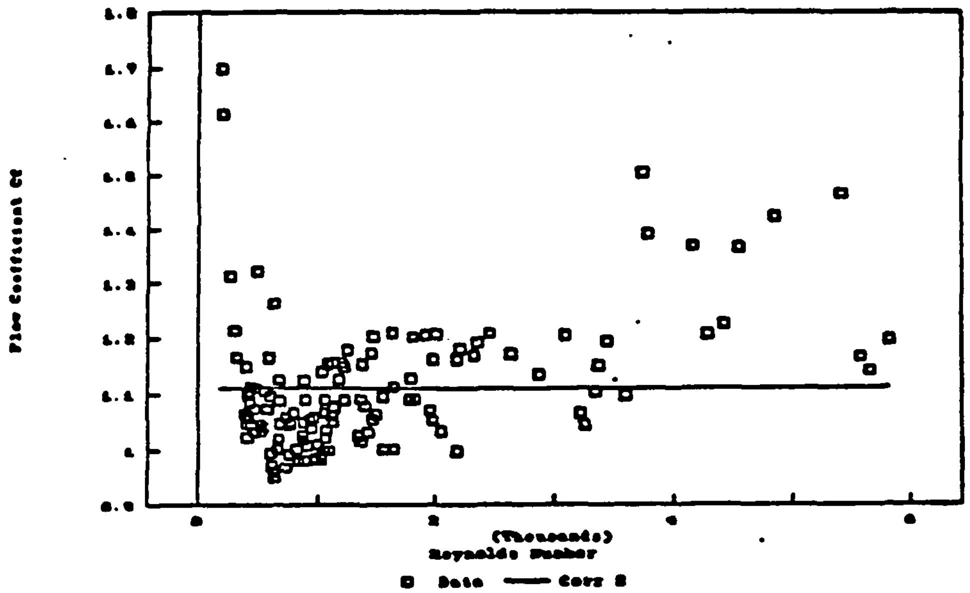

Figure 4. Flow Coefficient for CE Swirl-cone Spray Nozzle.

3.2.4 SUMMARY

Since the flow coefficient showed the same correlation with the Reynolds number for all three of the splashplate nozzles, this correlation appears to be independent of the nozzle diameter. This correlation was also the most accurate. Therefore this equation should be useful for the larger nozzles typically used in recovery boilers.

For the V-jet nozzles the correlation was somewhat different for the two different nozzles. Although there are not enough data available at this point to provide a good correlation for larger nozzles, the equation derived for the CE V-jet 15 should provide a reasonable estimate of the expected pressure drop for larger nozzles.

Because only one swirl-cone nozzle was tested, it is impossible to tell how accurate this average C_f-value will be for the larger nozzles used in recovery furnaces.

For both the splashplate and V-jet nozzles, the calculated flow coefficients behaved as expected. At high Reynolds Numbers they approached a limiting minimum value for C_f of slightly over 1.0. At lower Reynolds Numbers the flow coefficients were higher, which is the normal pattern for friction factors.

3.3 DROP SIZE DISTRIBUTION

3.3.1 ACCURACY OF THE IMAGE ANALYSIS METHOD

The accuracy of drop size analysis depends on the quality of video images. In order to create a binary image that correctly represents size information contained in a gray image, there must be a demarcation in the gray image to distinguish light intensities for the features to be measured from those for the background.

In order to determine the accuracy of the method, we have conducted several tests under simulated experimental conditions using spheres and cylinders of known dimensions. In one of the tests, a group of steel balls (refer to Table 4 for sizes) were glued on to two pieces of transparent plastic plates. Then the plates were mounted in the black liquor spray chamber spaced at three-inch intervals. Illumination and camera settings were similar to those for a real spray test. In another test, metal wires were used instead of steel balls because we did not have balls smaller than 2 mm in diameter. The plate interval in the wire test was 6 inches. Images for these tests were processed using the same procedures for images of sprays. For the metal balls, the sizes were measured by the image analyzer. For the metal wires, the wire thicknesses were measured manually on the screen. The results reported in Table 4 reveal that the absolute error of the image analysis method is approximately ±1 pixel, which is the smallest element the analyzer can detect. The actual size that a pixel represents in an image varies with the size of field-of-view. With a 80 x 80 mm^2 field-of-view and a 512 x 512 pixel monitor, each pixel represents a square of 0.156 x 0.156 mm^2. With this fairly constant absolute error, the relative error is inversely proportional to the size of an object to be measured.

In the above accuracy tests, the objects had regular shapes and were placed in the right focus range. This ensured that a minimum error limit would be attained. In an actual spray test, the drops may have irregular shapes which complicate drop diameter measurement, and appear outside the focus range, resulting in blurred images. The image of an out-of-focus droplet has smaller contrast than that of a droplet in focus. Consequently, when generating a binary image from a gray image, a droplet out of focus appears smaller than a droplet in focus. The actual measurement error can easily exceed those shown in Table 4.

TABLE 4. ACCURACY OF THE IMAGE ANALYSIS METHOD

OBJECT	SIZE (mm)	RELATIVE ERROR (%)	ABSOLUTE ERROR (pixel)
BALL	7.92	±2.0	±1.0
BALL	4.34	±4.4	±1.2
BALL	3.07	±5.7	±1.1
BALL	2.29	±7.0	±1.0
WIRE	2.29	±8.5	±1.3
WIRE	1.27	±6.0	±0.5
WIRE	1.07	±15	±1.0
WIRE	0.74	±22	±1.1
WIRE	0.64	±26	±1.1

3.3.2 PROCESSING IMAGES

Due to size limitations of the spray chamber, a black liquor spray may not have broken into individual droplets at the position for recording drop size, under certain test conditions. Images for these tests contain varying amounts of liquid strands, in addition to droplets. Since we are unable to predict how the strands break into droplets, images containing a significant portion of strands can not be analyzed for drop size distribution.

For images in which droplets are the major part and strands only occupy a small portion, it is fair to assume that the strands will break into droplets with the same size distribution as the droplets already in the images. Thus we can remove the strands from the images manually and analyze the size distribution from the remaining droplets. Even if the strands finally break into a somewhat different size distribution, and since they only occupy a small portion of the total spray, the final size distribution will not be altered significantly.

3.3.3 ESTIMATING DROP VOLUME

If all drops were spherical, drop volume could be calculated directly from diameters of two dimensional images. Since the drops are not always spherical, we need a proper way to estimate drop volume from two dimensional information.

Our observation reveals that non-spherical droplets generally have cylindrical shapes with hemispherical ends. Spacial orientation of the cylinders will not be considered. When a cylindrical shape appears in the image, we assume that it is the projection of a cylinder in a direction perpendicular to its axis. We further assume that the cylinder has two hemispherical ends. The volume of the image can be calculated from the length of the cylindrical part (L) and the radius (R):

$$V = \frac{4}{3}\pi R^3 + \pi R^2 L. \tag{11}$$

It is not accurate to let the image analyzer measure L and R directly, since sometimes the shape is irregular. A general parameter called ***Shape Factor*** (S) can be used to avoid measuring L and R directly. The definition of S is:

$$\frac{L}{R} = \pi\left[S - 1 + \sqrt{S(S-1)}\right] \tag{12}$$

For a circle (the projection of a sphere) S = 1, for any other shape S > 1. Then the ratio L/R can be calculated from S:

$$R = \sqrt{\frac{Area}{\pi + 2L/R}}, \tag{13}$$

and R and L can be calculated from the area and L/R:

$$L = \left(\frac{L}{R}\right)R. \tag{14}$$

When S = 1, L = 0, the model reverts to a sphere. For an irregular shape, the model calculates volume from an equivalent cylinder which has the same shape factor and area of projection as the irregular image.

Once the drop volume is obtained from equation (11), an equivalent diameter can be evaluated for a sphere which has the same volume as the droplet. This equivalent diameter is used in calculations of drop size distribution.

DROPLET SIZE DISTRIBUTION FUNCTION

The range of droplet sizes in most commercial sprays is very broad, more than two orders of magnitude between the smallest and largest diameter. Indeed, like many processes found in nature, there is no "smallest" or "largest" drop size in the spray. This is inherent in the normal, or Gaussian, distribution used to describe many naturally occurring phenomena. For most sprays the droplet diameter is not distributed in the manner of a normal curve. This was reported in the first annual report (2) on this project where black liquor spray size distributions for both CE swirl-cone and B&W splashplate nozzles showed S-shaped curves, with the top portions being much longer than the corresponding bottoms. Hence, it was concluded that black liquor spray droplet diameter is not normally distributed about the median, a common result for most spraying operations.

Several variable transformations have been successfully used to construct new variables from drop size so that the results can be described by the normal distribution function. Square Root-Normal (SQRT-N) and Upper Limit Logarithmic Normal (ULLN) are two such distribution functions which fit the data well. (c.f. Figure 4).

The parameters in the SQRT-N and ULLN functions are determined from drop diameters at certain cumulative volume fractions. The goodness of curve fitting can be better shown by plotting the data in straight lines. The data used in Figure 4 are plotted in another way in Figure 5, where the vertical axis (x_{exp}) corresponds to the horizontal axis of Figure 4 for the experimental data, and the horizontal axis (x) is the value on the standard normal curve at the point corresponding to the same cumulative volume fraction as x_{exp}. If the experimental data follow the distribution functions, they should form a straight line described by $x_{exp} = x$. Deviations from the straight indicate discrepancy between the distribution functions and the data.

Discrepancy at large drop size is often caused by an insufficient number of drops to form a smooth distribution curve. In most cases, the ratio of the volume of the largest drop to the total volume of all drops in a sample is less than 0.01. But sometimes the ratio can be as large as 0.03 when the total number of drops is small (<1000). Discrepancy at small drop size is often ascribed to the error due to a lower cutoff limit. Because the current image analysis method can only detect drops above a minimum size limit (about 0.5 mm), drops smaller than the lower limit are neglected. Therefore, experimental cumulative volume fraction starts from zero at the minimum size limit, whereas the theoretical cumulative volume fraction is larger than zero at the same point according to the normal distribution function. For most of the data, the error at small drop size is insignificant. The difference between x_{exp} and x may seem large, but the difference between the corresponding volume fractions is very small (<0.01). Therefore, their effect on the mass median diameter (D_m) is also very small.

The SQRT-N function is not sensitive to subtle changes at the ends of the distribution curves. This means that the function is less accurate at the ends. From another point of view, the parameters in the function are not severely affected by experimental errors, which are more significant at the ends of the distribution curve. The parameters in the SQRT-N function have clear physical meanings. Once a distribution curve is given, we

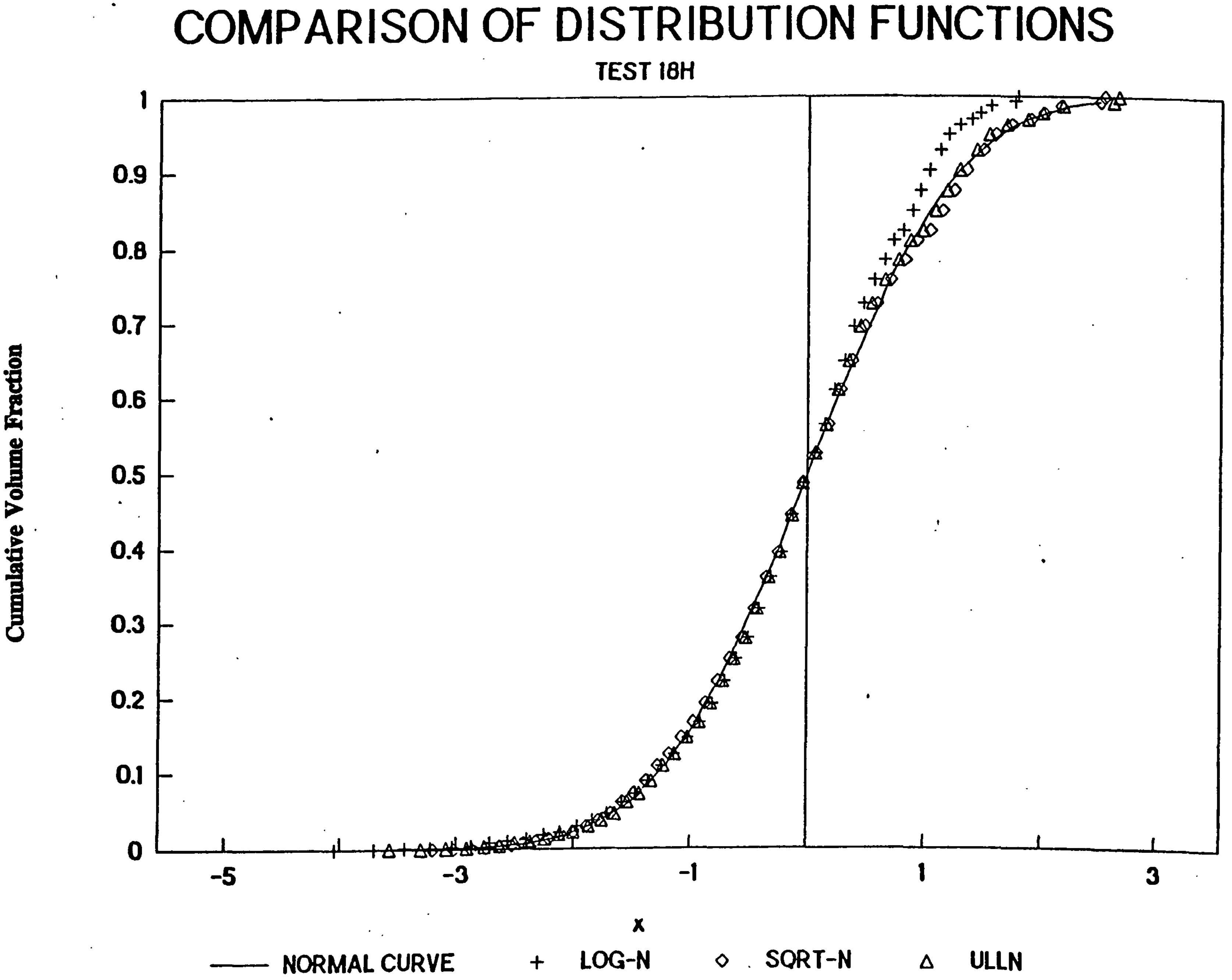
COMPARISON OF DISTRIBUTION FUNCTIONS
TEST 18H
Cumulative Volume Fraction
1
0.9
0.8
0.7
0.6
0.5
0.4
0.3
0.2
0.1
0
-5
-3
-1
1
3
x
NORMAL CURVE
+ LOG-N
◇ SQRT-N
△ ULLN

Figure 4.

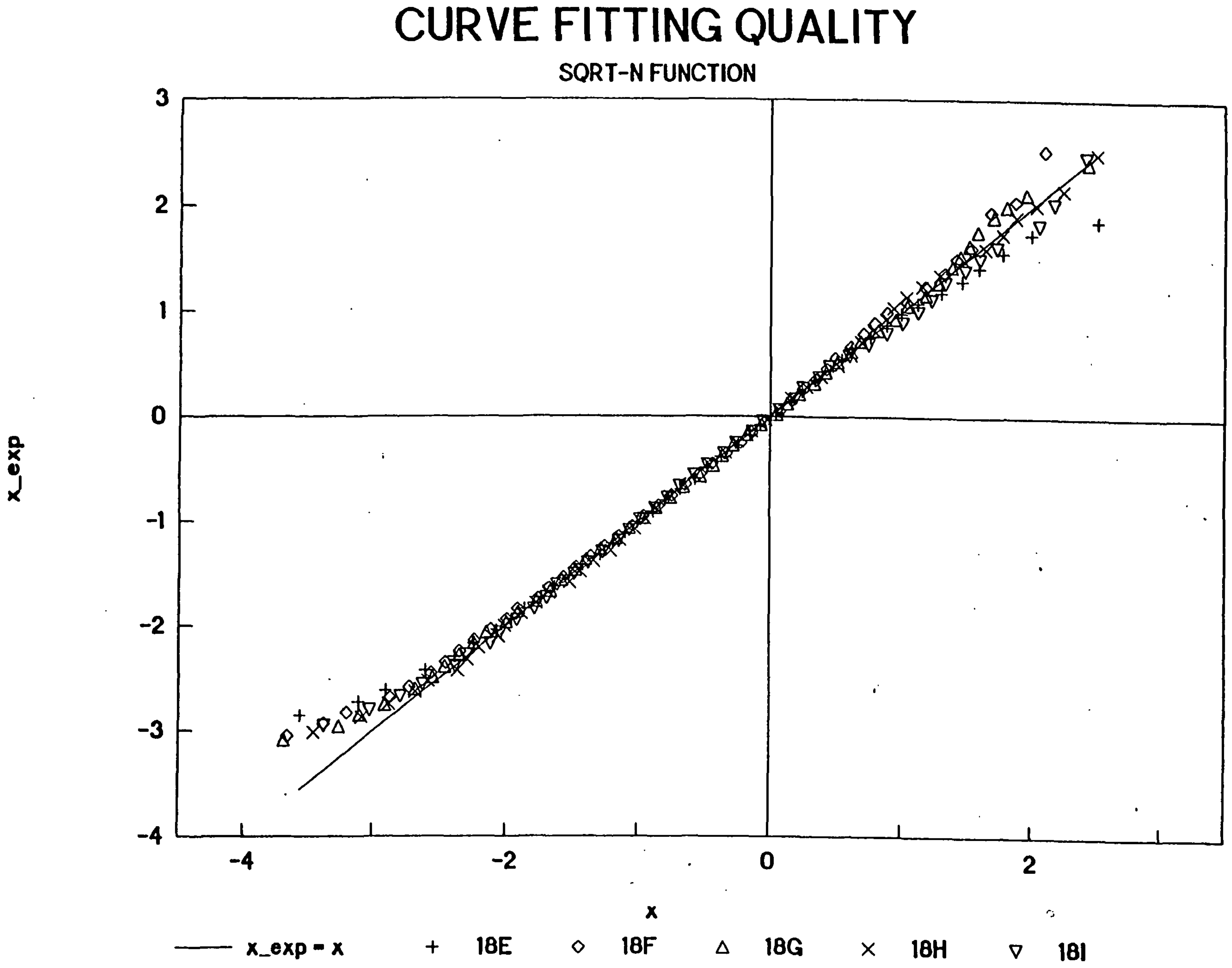
CURVE FITTING QUALITY
SQRT-N FUNCTION
x_exp
3
2
1
0
-1
-2
-3
-4
-4
-2
0
2
x
x_exp = x
+ 18E
◇ 18F
△ 18G
× 18H
▽ 18I

Figure 5.

Table 5. Test Conditions and Droplet Size Data Used in Dimensionless Group Correlations.

Test	Solids (%)	Spray Nozzle	Pressure (psi)	Temp. (°C)	D_m mm	s $mm^{1/2}$	$s/\sqrt{D_m}$
11A	50.2	CE swirl	8.3	32.0	2.67	0.31	0.190
11B	50.2	CE swirl	22.2	33.0	2.20	0.28	0.189
11C	50.2	CE swirl	31.6	33.9	2.16	0.28	0.191
11D	49.0	CE swirl	10.1	33.4	2.34	0.31	0.203
11E	48.9	CE swirl	21.5	34.4	2.22	0.29	0.195
11F	48.9	CE swirl	30.2	35.9	2.03	0.26	0.182
11G	48.5	CE swirl	30.5	53.8	1.95	0.24	0.172
11H	48.5	CE swirl	21.6	52.1	2.12	0.26	0.179
11I	48.3	CE swirl	11.0	51.0	2.38	0.25	0.162
12A	57.4	CE swirl	12.0	56.6	2.70	0.34	0.207
12B	57.3	CE swirl	17.1	56.3	2.37	0.30	0.195
12C	56.7	CE swirl	30.5	55.9	2.00	0.27	0.191
12D	54.9	CE swirl	30.0	68.6	1.85	0.23	0.169
12E	55.3	CE swirl	18.8	68.8	2.07	0.27	0.188
12F	55.7	CE swirl	9.7	72.0	2.11	0.29	0.200
12G	53.4	CE swirl	10.0	92.3	2.25	0.29	0.193
12H	53.4	CE swirl	19.2	92.7	1.93	0.25	0.180
12I	53.9	CE swirl	31.9	93.0	1.82	0.23	0.170
13B	61.9	CE swirl	22.1	74.1	2.14	0.27	0.185
13C	62.0	CE swirl	29.3	75.2	2.00	0.26	0.184
13D	61.7	CE swirl	29.3	91.8	1.66	0.24	0.186
13E	61.9	CE swirl	18.4	95.7	2.04	0.27	0.189
13F	62.3	CE swirl	10.1	99.7	2.18	0.28	0.190
13G	62.1	CE swirl	11.3	124.5	1.07	0.16	0.232
13H	60.6	CE swirl	20.3	120.4	2.00	0.24	0.170
13I	61.8	CE swirl	31.3	120.0	1.87	0.24	0.176

Table 5 (Continued).

Test	Solids (%)	Spray Nozzle	Pressure (psi)	Temp. (°C)	D_m mm	s $mm^{1/2}$	$s\sqrt{D_m}$
18A	52.1	SS V-jet/65	8.9	36.8	2.19	0.28	0.189
18B	52.3	SS V-jet/65	20.7	36.3	1.95	0.25	0.179
18C	52. 5	SS V-jet/65	31.8	35.8	1.86	0.23	0.169
18D	51.0	SS V-jet/65	30.9	53.2	1.72	0.22	0.168
18E	51.1	SS V-jet/65	18.9	53.6	1.90	0.27	0.196
18F	51.4	SS V-jet/65	9.4	53.4	2.23	0.29	0.194
18G	49.6	SS V-jet/65	9.2	68.5	2.08	0.27	0.187
18H	49.9	SS V-jet/65	20.9	70.0	1.73	0.23	0.175
18I	49.5	SS V-jet/65	32.7	74.4	1.68	0.23	0.177
17A	59.4	B&W 12/45	46.6	62.4	2.45	0.38	0.242
17B	59.2	B&W 12/45	31.2	66.2	2.44	0.36	0.230
17H	59.9	B&W 12/45	45.5	88.7	2.27	0.38	0.252
17I	60.5	B&W 12/45	29.4	91.5	2.10	0.32	0.221
17K	57.0	B&W 12/45	15.6	109.9	2.59	0.35	0.217
33D	60.9	B&W 12/45	25.3	103.8	2.36	0.32	0.208
33E	59.5	B&W 12/45	40.0	93.1	2.22	0.29	0.195
36G	56.2	B&W 12/45	19.5	100.6	2.64	0.35	0.215
36H	55.9	B&W 12/45	32.7	100.5	2.05	0.26	0.189

can find only one set of parameters, the mass median diameter (D_m) and the standard deviation (s), that will give the best curve fitting result.

Interestingly, the data show that the ratio of s to $\sqrt{D_m}$, called the normalized standard deviation, is essentially constant for a given nozzle, thus reducing the SQRT-N distribution to a one-parameter model, namely the mass median diameter. Based on the data in Table 5, the normalized standard deviations for the splashplate, swirl cone, and V-jet nozzles are 0.22 ± 0.03, 0.19 ± 0.02, and 0.18 ± 0.02mm ½, respectively. This is a highly significant result because it implies that all three nozzles gave essentially the same distribution width.

That this can be so may be rationalized through the basic laws of mass and momentum conservation. What is essential is the balance between viscous, inertial, pressure, and surface tension forces present in the system. These are dependent upon fluid properties, flow velocities, and nozzle dimensions, i.e. the fluid mechanics of the system. There are no independently applied forces to change or upset the naturally occurring balance. This would imply that changes in drop size distribution, both in shape and width, must come from a nozzle design that features some independent external force, such as vibratory assist.

The ULLN function generally fits experimental data better than the SQRT-N function at the ends of the distribution curves; however the parameters of the ULLN function are susceptible to measurement errors. In many cases, we found multiple values for the parameters that fit the same set of data with the same accuracy. This uncertainty of the parameters makes it futile to try to correlate the statistical parameters with physical parameters, nozzle design features, or operating conditions.

3.4 DEPENDENCE ON OPERATING PARAMETERS

3.4.1. CORRELATION BY DIMENSIONLESS GROUPS

In any applied study such as this one, it is necessary to relate statistical droplet size distribution results to physical and operating parameters (e.g. viscosity, density, surface tension, temperature, nozzle pressure, and nozzle design) that are controllable by the furnace operator. Traditionally, this is done through the use of dimensionless groups. If we employ the Square Root-Normal function for correlating droplet size distributions, we need only to relate the mass median diameter to appropriate physical and operating parameters, since the ratio $S/D_m^{0.5}$ we have found to be essentially constant.

Numerous correlations for various spray nozzles are given in the literature (3,4,5), and most are expressed in the form:

$$\frac{D_m}{D_n} = K\, Re^{\alpha} We^{\beta} \tag{15}$$

where: D_m = mass median diameter
D_n = nozzle diameter
Re = Reynolds No. ($D_n V \rho_L/\mu_L$)
We = Weber No ($D_n V^2 \rho_L/\sigma_L$)
K, α, β = empirical constants
σ_L = surface tension
ρ_L = liquor density
μ_L = liquor viscosity
V = liquor velocity at nozzle exit

Use of such dimensionless groups has some relationship to the physical world in that Reynolds Number represents the ratio of inertial to viscous forces, whereas Weber Number accounts for liquid/gas interactions and relates inertial and surface tension forces. For moderate temperature systems, these may be adequate descriptors. However, for black liquor spraying at or slightly above the atmosphere boiling temperature of water, some accounting for the vaporization of water may need to be included. Three additional dimensionless groups-the Ohnesorge Number, the Euler Number and the Schmidt Number-immediately suggest themselves:

$$Eu = \frac{g_c P_w}{V^2 \rho_L} \tag{16}$$

$$Sc = \frac{\mu_L}{\rho_L D_{WL}} \tag{17}$$

$$Oh = \frac{\mu_L^2}{\rho_L \sigma_L D_n} \tag{18}$$

where: P_w = vapor pressure of water in liquor
D_{WL} = diffusivity of water in liquor
g_c = gravitational constant

Physically, the Euler No. represents the ratio of pressure forces to inertial forces and would characterize the process of water wanting to leave the sheet in the form of vapor, resulting in the formation of perforations. In turn, the Schmidt No. relates mass and momentum transfer, characterizing the process of water molecules getting through the boundary layer at the gas-liquid interface surrounding the liquor sheet, again leading to perforations. The Ohnesorge Number is a dimensionless viscosity and interrelates the viscous and surface tension forces within the droplet (6).

Putting various combinations of these dimensionless groups in a functional form similar to eq. (15), and correlating these with the drop size distribution data, we concluded that the most accurate and most useful representations of the spraying data are:

$$\frac{D_m}{D_n} = K_1 (Re)^{a} (Eu)^{b_1} \tag{19}$$

$$= K_2 \ (Eu)^{b^2} \ (Sc)^{c} \tag{20}$$

where the K_i, a, b_i, and c, are empirical constants. The test conditions and size distribution data used in these correlations are summarized in Table 5. Correlations incorporating Weber or Ohnesorge Number were not undertaken because of a lack of surface tension data. Taking two groups at a time proved more effective than three in that the additional arbitrary parameter gave no significant improvement to the goodness of fit.

Table 6 presents values for the arbitrary parameters. There does not appear to be any significant difference between the two correlations shown.

TABLE 6. EMPIRICAL CORRELATIONS FOR THE DROP SIZES OF BLACK LIQUOR SPRAYS

TEST	k	a	b	c	r^2
11	0.6420	-0.1354	0.0943		0.9550
12	0.6837	-0.1774	0.1120		0.8515
13	0.5526	-0.1707	0.1246		0.9368
18	0.7312	-0.118	0.1121		0.9368
11	0.1041		0.1612	0.0894	0.9609
12	0.0563		0.1946	0.1154	0.8586
13	0.0443		0.2047	0.1153	0.6637
18	0.1426		0.1725	0.0811	0.9372

If the dimensionless groups are broken down in terms of their component parameters, the dependence of D_m emerges for the swirl cone nozzle:

$$D_m = \begin{cases} 0.64\,(D_n)^{0.86}\ (V)^{-0.32}\ (\rho)^{-0.23}\ (\mu L)^{0.14}\ (P_w)^{0.09} & \text{(21a)} \\ 0.10\,(D_n)^{1.00}\ (V)^{-0.32}\ (\rho)^{-0.25}\ (\mu L)^{0.09}\ (P_w)^{0.16}\ (D_{WL})^{-0.09} & \text{(21b)} \end{cases}$$

and for the V-jet:

$$D_m = \begin{cases} 0.73\,(D_n)^{0.88}\ (V)^{-0.34}\ (\rho)^{-0.23}\ (\mu L)^{0.12}\ (P_w)^{0.11} & \text{(22a)} \\ 0.14\,(D_n)^{1.00}\ (V)^{-0.35}\ (\rho)^{-0.25}\ (\mu L)^{0.08}\ (P_w)^{0.17}\ (D_{WL})^{-0.08} & \text{(22b)} \end{cases}$$

The functional dependencies exhibited in equations (21) and (22) give interesting interpretations. Droplet diameter decreases as both velocity and density increase. Both are related to the kinetic energy of the liquor issuing from the nozzle, implying the greater the energy that is dissipated, the smaller the drop size. Droplet diameter increases as both viscosity and water vapor pressure increase. This is seen as largely a viscosity dependence, since high vapor pressure of the liquor as it exits the nozzle gives higher solids and accompanying higher viscosity. The implication here is that strong viscous forces counteract the tendency to create high surface energy, as typified by smaller droplets with higher surface area per mass of liquor.

It is interesting to note the relative insensitivity of D_m to liquor physical properties, with exponents in equations (21) and (22) generally in the 0.1 to 0.3 range. (The apparent stronger dependence on nozzle diameter is artificial, since, in these correlations, nozzle diameter for each nozzle type was not varied).

The effect of nozzle diameter has been determined independently for the splashplate, as shown in Table 7. Drop size data were obtained for three different nozzle diameters (two manufacturers), using 56% solids liquor at 76-100° C, 0.07-0.215 kg/m/s, and velocities of 10-17 m/s.

TABLE 7. TEST CONDITIONS FOR SPLASHPLATE NOZZLES

Test	Nozzle	Dn mm	D_m/Dn	Solids (%)	VEL m/s	T1 (C)	VISC kg/m/s	DENS kg/m^3	Pw kg/ms^2
36A	B&W	9.525	0.3025	55.3	9.95	76.0	0.2150	1310	40187
36B	B&W	9.525	0.2101	55.9	14.73	79.5	0.1960	1303	46400
36G	B&W	9.525	0.2773	56.5	12.03	100.6	0.0713	1296	103680
36H	B&W	9.525	0.2153	57.3	16.28	100.5	0.0706	1296	103293
38A	B&W	9.525	0.2731	54.9	11.35	81.5	0.1247	1296	50202
38B	B&W	9.525	0.2290	55.3	15.50	83.7	0.1256	1297	54901
38C	B&W	11.9	0.2126	55.7	11.31	83.8	0.1341	1300	55035
38D	B&W	11.9	0.2000	55.9	16.27	85.0	0.1396	1301	57838
38E	TAMP	18	0.1756	56.6	12.78	84.9	0.1691	1305	57589
38F	TAMP	18	0.1183	56.5	16.89	85.2	0.1561	1304	58154

Using a modified dimensionless form,

$$\frac{D_m}{D_n} = K\, Re^{a}\, Eu^{b}\, Sc^{c}\, D_n^{d} \tag{23}$$

two correlations were obtained:

$$\frac{D_m}{D_n} = \begin{cases} = 0.0560\ (Re)^{-0.16}\ (Eu)^{0.21}\ (D_n)^{-0.61}, & r^2 = 0.836 \quad (24a) \\ = 0.0024\ (Eu)^{0.28}\ (Sc)^{0.11}\ (D_n)^{-0.81}, & r^2 = 0.836 \quad (24b) \end{cases}$$

If the dimensionless groups are broken down in terms of their component parameters,

$$D_m = \begin{cases} 0.0560\,(D_n)^{0.23}\ (V)^{-0.58}\ (\rho)^{-0.37}\ (\mu L)^{0.16}\ (P_w)^{0.21} & (25a) \\ 0.0024\,(D_n)^{0.19}\ (V)^{-0.56}\ (\rho)^{-0.39}\ (\mu L)^{0.11}\ (P_w)^{0.28}\ (D_{WL})^{-0.11} & (25b) \end{cases}$$

As with the swirl cone and V-jet results above, the liquor physical properties generally have exponents in the 0.1 - 0.3 range. Mass Median diameter decreases as velocity increases (approx. square root dependence) and increases as nozzle diameter increases.

3.5 EFFECT OF TEMPERATURE

3.5.1 DROPLET DIAMETER

The effect of temperature is difficult to determine from the dimensionless group analysis procedure. Density, viscosity, vapor pressure, and diffusivity are all functions of temperature, with ρ_L and μ_L dropping with increasing temperature and Pw and D_{WL} increasing. With the present data, velocity and temperature are the only operating parameters that varied significantly within each test, suggesting a parametric approach in terms of velocity and temperature only. If the diameter ratio is expressed empirically by:

$$\frac{D_m}{D_n} = K\, V^{a}\, T^{b} \tag{26}$$

where T is expressed in °C, correlations emerge for the swirl cone Test 11:

$$\frac{D_m}{D_n} = 1.30\ V^{-0.31}\ T^{-0.19} \qquad (r^2 = 0.89) \tag{27}$$

and for the V-jet:

$$\frac{D_m}{D_n} = 0.69\ V^{-0.34}\ T^{-0.09} \qquad (r^2 = 0.93) \tag{28}$$

where: V = velocity (m/s)
T = temperature (°K)

The basic conclusion here is that drop size decreases as temperature increases. This is consistent with the limited data of Bennington and Kerekes (5). The exponents for velocity are about the same as reported in equations (21 and 22) above, based on dimensionless groups; the exponents for temperature can then be expected to represent the combined temperature effects embodied in density, viscosity, and vapor pressure. The dimensionless group approach predicted drop size to decrease with increasing density, decreasing vapor pressure, and decreasing viscosity. Hence, the viscosity temperature dependence is consistent with this and outweighs the seemingly anomalous trends of vapor pressure and density. That this is true is because the temperature dependence of viscosity is much more sensitive than it is for density, and the exponential dependence of the parameters is strongest for viscosity.

During earlier experimental tests with black liquor spray nozzle, it was noted that there was a dramatic change in the behavior of the spray discharge from the nozzle above certain temperatures. Operating above this limit resulted in much smaller drops. This transition temperature was found at the upper end of the normal operating region for black liquor spraying, and the phenomenan appears to be due to operation above the boiling point, resulting in flashing occurring inside the nozzle. Since initial drop diameter is a critical parameter in the operation of recovery boiler and has a direct effect on the amount of carryover and the condition of the char bed, tests were performed to determine the operating conditions where this type of spraying will occur, and estimate the effect on droplet size and other operating characteristics.

The tests were performed by adjusting the nozzle pressure to a given flow level at a relatively low initial temperature (abount 200° F), then the liquor temperature was gradually increased by using the heat exchanger and the direct steam injection, until the transition temperature. The values listed in Table 8 represent time-averages of the parameters over the test period and not the specific transition values. Values during a typical test run are shown in Figure 6.

The liquor temperature where the transition to flashing occurs is not easy to determine precisely. It is expected that the transition temperature will be higher than the boiling point of the black liquor since the pressure at the nozzle will tend to suppress flashing. The atmospheric boiling point of the liquor was not determined experimentally for this liquor, but a reasonable estimate can be made using equation (29). Typical values of K range from 6 to 10 C, and the estimates were made with a K value of 7.5 C.

Table 8. Average Conditions During Test Runs.

TEST	NOZZLE	TEMP C	PRES. PSI	FLOW GPM	VISC. CP	SOLIDS %
25B	Swirl-cone	104.3	32.3	12.9	72.4	58.0
25A	Swirl-cone	107.4	21.2	10.4	62.3	57.6
26A	Swirl-cone	124.3	27.8	11.0	200.2	69.2
26B	Swirl-cone	122.4	20.4	8.6	199.0	69.1
24D	Splash-plate	105.8	29.2	14.0	80.7	59.6
24C	Splash-plate	109.1	23.0	11.5	124.7	60.5
26D	Splash-plate	124.0	31.4	10.7	169.7	68.6
26C	Splash-plate	122.6	24.1	8.6	171.7	68.3
24B	V-jet	106.6	28.3	14.6	129.2	63.1
24A	V-jet	107.8	14.8	10.5	88.6	60.6
26E	V-jet	122.4	21.9	10.0	258.1	70.7
26F	V-jet	122.3	30.7	12.5	320.8	72.3

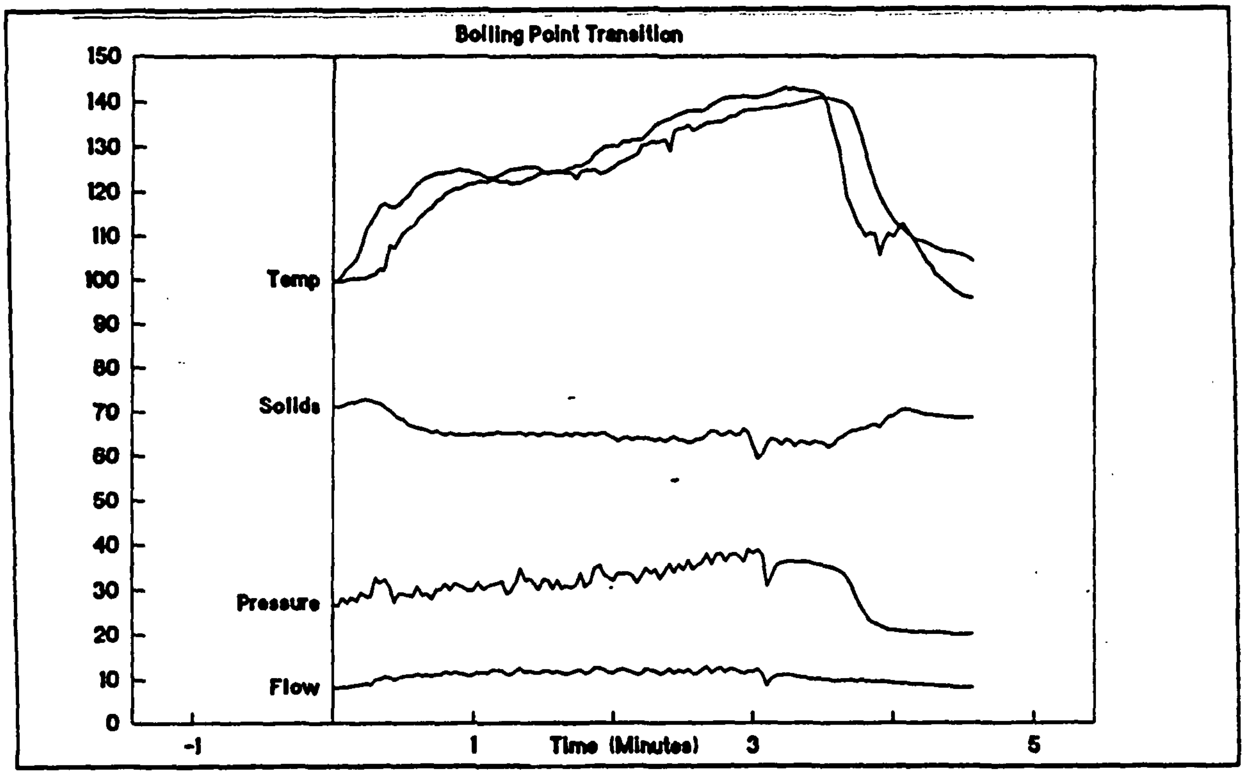

Figure 6. Test 26D with B+W 12/45 Splashplate Nozzle.

$$T_{BP} = 100 + K*\left(\frac{S\%}{100-S\%}\right) \tag{29}$$

Using the Clasius-Clapeyron Equation it is also possible to estimate the boiling point at a given pressure. This value was calculated for the pressure at the nozzle inlet. As expected, the transition temperature lies between the atmospheric boiling point and the pressurized boiling point which implies that the flashing is initiated somewhere in between the inlet and outlet of the nozzle. The transition temperature was about 5 °C above the boiling point at 60% solids and about 10 °C above the boiling point at 70% solids. A crude estimate of the flashing temperature can be made from this data.

$$T_{Flash} = 100 + 10*\left(\frac{S\%}{100-S\%}\right) \tag{30}$$

As the spray tests were performed and the temperature was gradually increased, a continuous video tape of the spray pattern was recorded. The image analysis of these tapes was performed by first analyzing the segment of the tape above the transition which appeared to have a minimum drop size. Two points before the transition temperature were also analyzed to measure the mass median drop size and standard deviation. In some cases two additional points were analyzed after the transition as the temperature was allowed to fall.

For each test three to five drop diameters were measured corresponding to different points in the test (Figure 7). Because the time of the video tape is not known with respect to the data collection, it is difficult to accurately correlate these drop sizes with the measured operating conditions at a given point in time.

To simplify the analysis, the largest median drop size was used as representative of the conditions below transition and the smallest median drop size is used for conditions above the transition. These data could then be correlated to operating conditions. The change in drop diameter ratio (Dm/Dn) due to the flashing was an average decrease from 2.46 to 1.64. The ratio of the drop size above the transition temperature to that before and after transition ranged from 0.45 to 0.77.

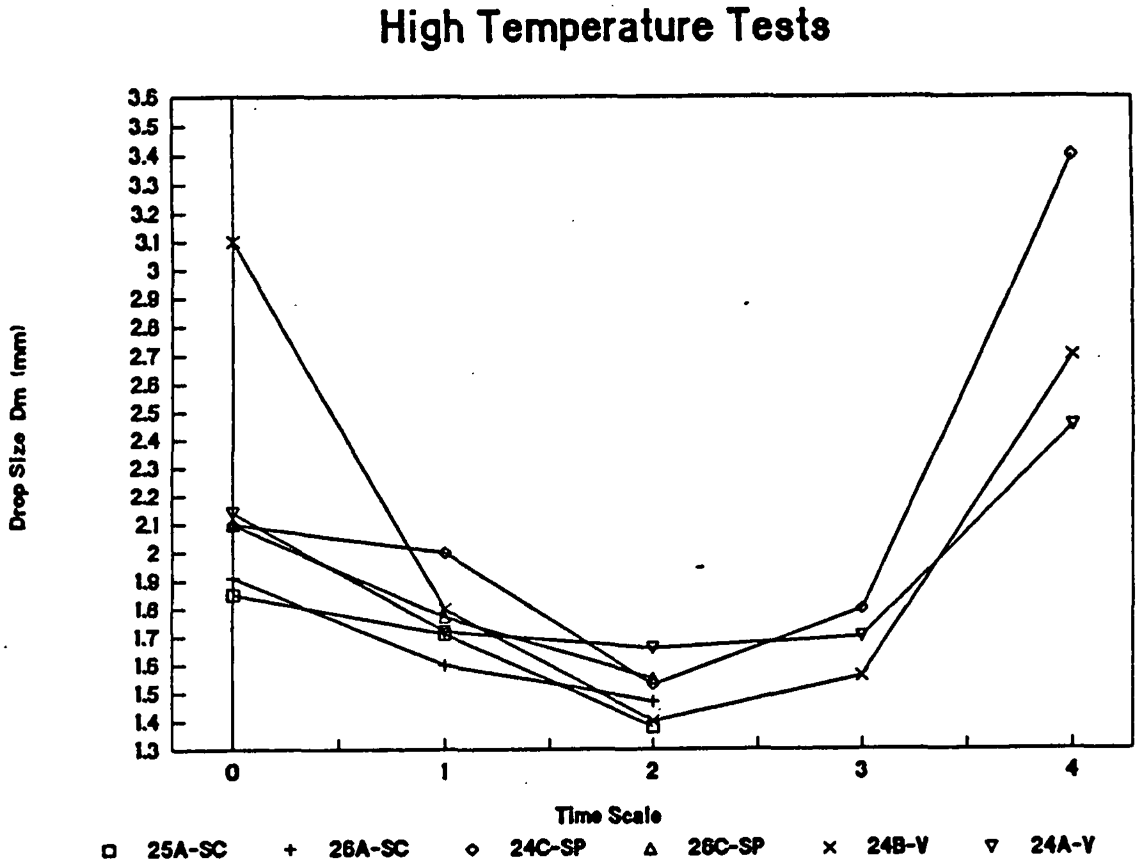

Figure 7.

In addition to measuring the median drop size, the standard deviation of a square-root normal distribution is also calculated for each test. Earlier, it was reported that the standard deviation is strongly correlated to the median drop size such that s/Dm^.5 is on average equal to 0.20. For these high temperature tests similar values of s/Dm^.5 were measured. Below transition the average value was 0.19.

The abrupt change of mass median diameter for liquor temperature above the boiling point is consistent with the observations reported by Galtung and Williams (7). That Bennington and Kerekes (5) did not report this phenomenon is probably due to the order-of-magnitude smaller droplets (0.2mm) they measured where surface tension forces may become more important.

3.5.2 PRESSURE DROP VS. FLOW RATE

The flow/pressure drop characteristics of nozzles operating above the transition temperature have been characterized. Results in this test series for conditions below the transition using splashplate nozzles and the SS V-jet agreed with equations (8) and (9), respectively. However, for operating conditions at or above the transition temperature, the flow coefficients were found to be higher than what the correlation would predict (i.e. higher ΔP than expected).

In the original calculations, the pressure drop across the spray nozzle was assumed to be equal to the inlet gauge pressure, since the outlet of the nozzle was at atmospheric pressure. For the high temperature tests where the temperature is still below the transition temperature, a simple correction can be made by using the difference between the inlet pressure and the vapor pressure of the black liquor. The flow coefficients calculated in this method closely agree with the correlations for the splashplate and V-jet nozzles (Figure 5). This confirms that the actual pressure at the outlet of the nozzle is equal to the vapor pressure of the liquor exiting the nozzle.

This technique does not yield reliable results with the swirl-cone nozzle. The geometry of the swirl-cone is more complex, with the liquor passing through two separate restrictions before discharge. In the previous analysis of flow coefficients at low temperatures, no correlation could be derived between C_f and Re, so it is not surprising that no correlation exists near the flashing temperature.

Above the transition temperature the flow coefficients are not reliable due to the formation of steam in the nozzle and two-phase flow. Flow coefficients are based on the Bernoulli equation, which uses a mechanical energy balance and assumes the enthalpy of the liquor is constant, so this would not be expected to hold at flashing conditions. Methods have been developed which allow prediction of two phase flow ΔP based on liquid flow ΔP and the ratio of gas to liquid that is present (8). Not enough data are available to perform a calculation. Typically, pressure drops for two phase flow can be twice those for single phase.

3.6 MASS FLOW DISTRIBUTION

For a complete understanding of black liquor spray nozzle operation, it is important to know the angle of the spray pattern produced by a given nozzle and flow conditions, and also how the mass flow of black liquor varies within the angle measured around the nozzle. This type of information is especially useful as input data for the current work at IPST to develop a computer model simulation of a recovery boiler.

Data were collected to measure the mass flow distribution of liquor sprays from different nozzles, the B&W 12/45 splashplate and the Spraying Systems V-jet 11/65. The data were collected at different nozzle operating pressures and liquor viscosities.

3.6.1 EXPERIMENTAL PROCEDURE

Samples of sprayed liquor were collected by using two different types of sampling devices. The first arrangement used a single box with a large 3 x 3 inch opening. A trap door on the front of the box could be opened for a fixed length of time (generally 5 to 10 seconds) and then closed. This was used with the SS V-jet nozzle and samples were collected at a distance of about 33 inches from the nozzle.

A second sampling device was constructed for the B&W Splashplate nozzle. Nine 1 x 1-inch metal sampling boxes were arranged on a half circle frame at 20° intervals. The radial distance from the nozzle to the front edge of each box was fixed at 4.5 inches. The boxes cut the liquor sheet into sections which could be collected and accurately weighed to determine the local mass flowrate at the nine different angles. Because the angle and position of the sampler is fixed with respect to the nozzle, these samples are slightly more reproducible than those collected with the V-jet sampling device, which had to be repositioned for each sample.

Two to four samples were collected and averaged for each data point. Measurements were taken at 5 to 9 points over the total spray angle for both the B&W 12/45 splashplate and the SS 11/65 V-jet. In all cases the entire sheet in the direction perpendicular to the sheet surface is being collected.

This work was performed at relatively low solids concentrations (55 to 65%), which allowed the experimental work to be performed at lower temperatures (120 to 185° F). This was an important safety consideration, since the experimental procedures for these tests required close access to the spray nozzle. Changes in the solids concentration are not expected to have a large influence on the mass flowrate distribution.

3.6.2 ANGLE OF SPRAY PATTERN

Three tests were performed with the SS V-jet nozzle, while five more tests were performed with the B&W 12/45 splashplate nozzle. All of the test conditions are listed below in Table 9. The overall spray angle (α) was also measured for each of these tests and ($\alpha/2$) is listed in the table. This represents the angle from the nozzle centerline to the outer edge of the spray sheet. The angle measurements were relatively unsophisticated and have an estimated confidence limit of ± 5%.

TABLE 9. Spray Angle α for B&W 12/45 Splashplate and SS 11/65 V-jet Nozzles.

Test	Nozzle	Liquor Viscosity cP	Nozzle Pressure psi	Reynolds Number	Spray Angle $\alpha/2$
30A	B+W 12/45 Splashplate	219.6	17.9	492	65.0
29A	B+W 12/45 Splashplate	224.2	25.9	605	70.0
30B	B+W 12/45 Splashplate	229.4	34.7	684	75.0
31A	B+W 12/45 Splashplate	50.1	18.3	2697	78.0
31B	B+W 12/45 Splashplate	65.5	34.9	2862	83.0
28A	S 11/65 V-jet	54.6	10.9	2120	28.5
28B	S 11/65 V-jet	67.5	19.9	2333	30.1
27A	S 11/65 V-jet	346.0	11.0	321	18.9

The variation of the spray angle seen in these test is typical behavior for pressure nozzles. The spray angle will increase with the operating pressure until it reaches a maximum value. Above this point the spray angle will decrease slightly with increasing pressure. Viscosity has a strong influence on the spray angle, with increasing viscosity causing a reduction in the spray angle.

The spray angle for the splashplate is much wider and approaches 180° at high flow-rates and low viscosities. The SS V-jet nozzle is classified as a 65° nozzle by the manufacturer and the measured values approach this at high flows and low viscosity.

3.6.3 SPLASHPLATE NOZZLE MASS DISTRIBUTION

In order to characterize a given spray nozzle, it is necessary to know how the mass flow varies with angular position in the spray sheet. This angle (ϕ) is measured with respect to the centerline of the splashplate. Because the sampling box has finite width, the measured flowrate represents an average value over the angle $\Delta\phi$. The measured values are presented as a normalized mass flow factor (Mf), which is the ratio of the measured flowrate at a given angular position to the total flow averaged over the entire spray angle.

$$Mf = \frac{\Delta M/\Delta\phi}{Mt/\alpha} \tag{31}$$

where ΔM = local mass flow (g/sec)
$\Delta\phi$ = angle measured (degrees)
Mt = total nozzle flow (g/sec)
α = total spray angle (degrees)

The mass flow factor is plotted as a function of the angle ϕ in Figures 8 and 9 for the B&W splashplate. All curves have a similar overall shape which does not appear to be strongly influenced by the viscosity or total flowrate over the range tested.

It could be seen by visually studying the spray sheets that there was a central core with a fairly uniform flowrate in the range from $-15° < \phi < 15°$. Outside of this region the flowrate drops off steadily almost to the outer edge. At the very edge of the sheet is a thick slow-moving rim and just inside this is a thin region.

For Test 29A, a different sampler was used to measure a narrower angle. This test shows the high flowrate at the rim. For the other tests this feature was lost in the average value of the wider angle measured.

Two of the tests showed an unusually high flow at about +20° from the centerline. This high flow was a relatively stable phenomenon which remained in the spray for several minutes and showed up consistently in the mass measurements with the B&W Splashplate nozzles. It is created by backwards flow on the splashplate, which travels around a recess that encircles the nozzle tip, and then forms a separate flow stream. The point where it contacts the sheet is a function of the nozzle orientation. Unlike the high-speed video work where the spray sheet is in a vertical plane, the mass measurements were made with the spray pattern in a horizontal orientation. The mass flow of the recycle stream itself is insignificant, but, it may have been shifting the splashplate flow off to one side during these tests.

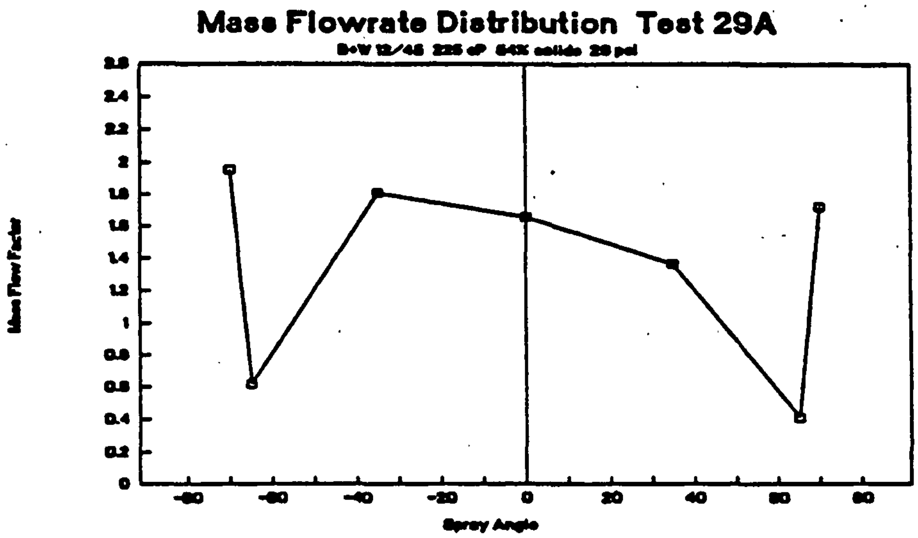

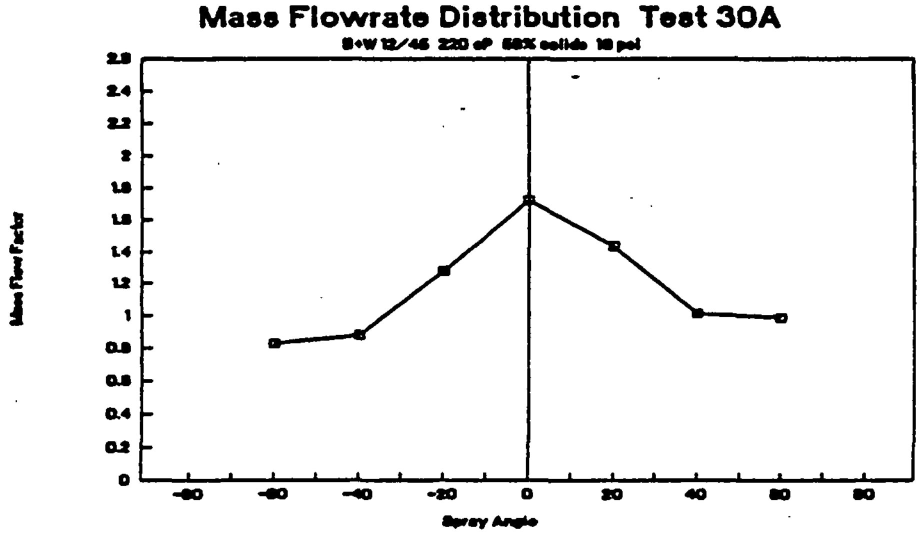

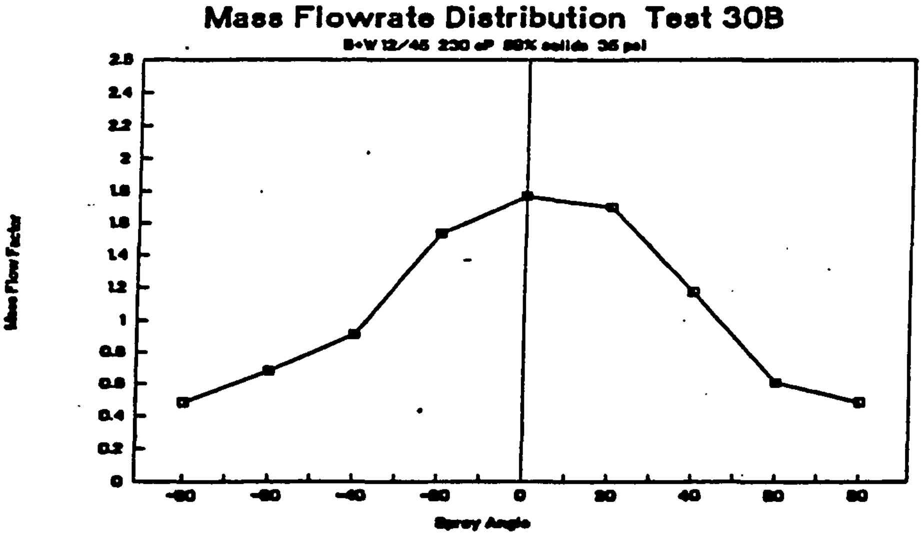

Figure 8. Mass Flow Distribution Curves for the B&W 12/45 Splashplate Nozzle at High Viscosity.

Mass Flowrate Distribution Test 31A

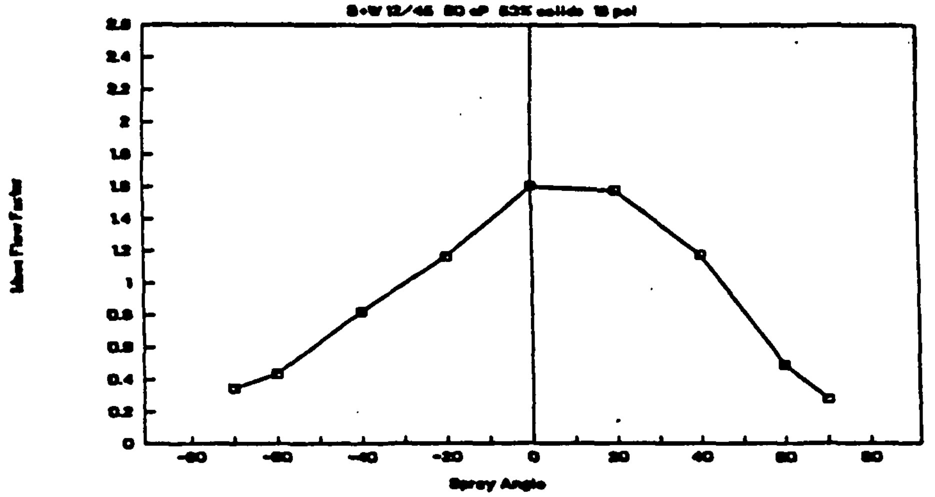

Mass Flowrate Distribution Test 31B

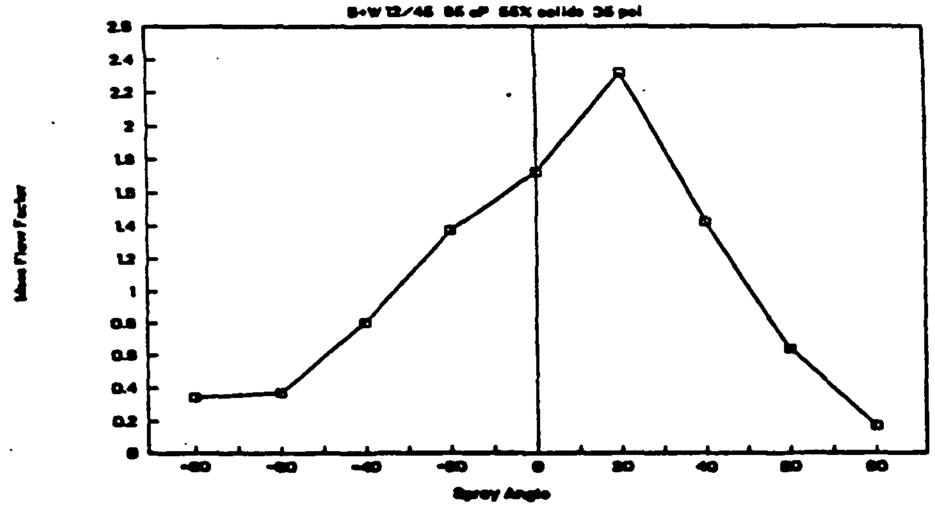

Figure 9. Mass Flow Distribution Curves for the B&W 12/45 Splashplate Nozzle at Low Viscosity.

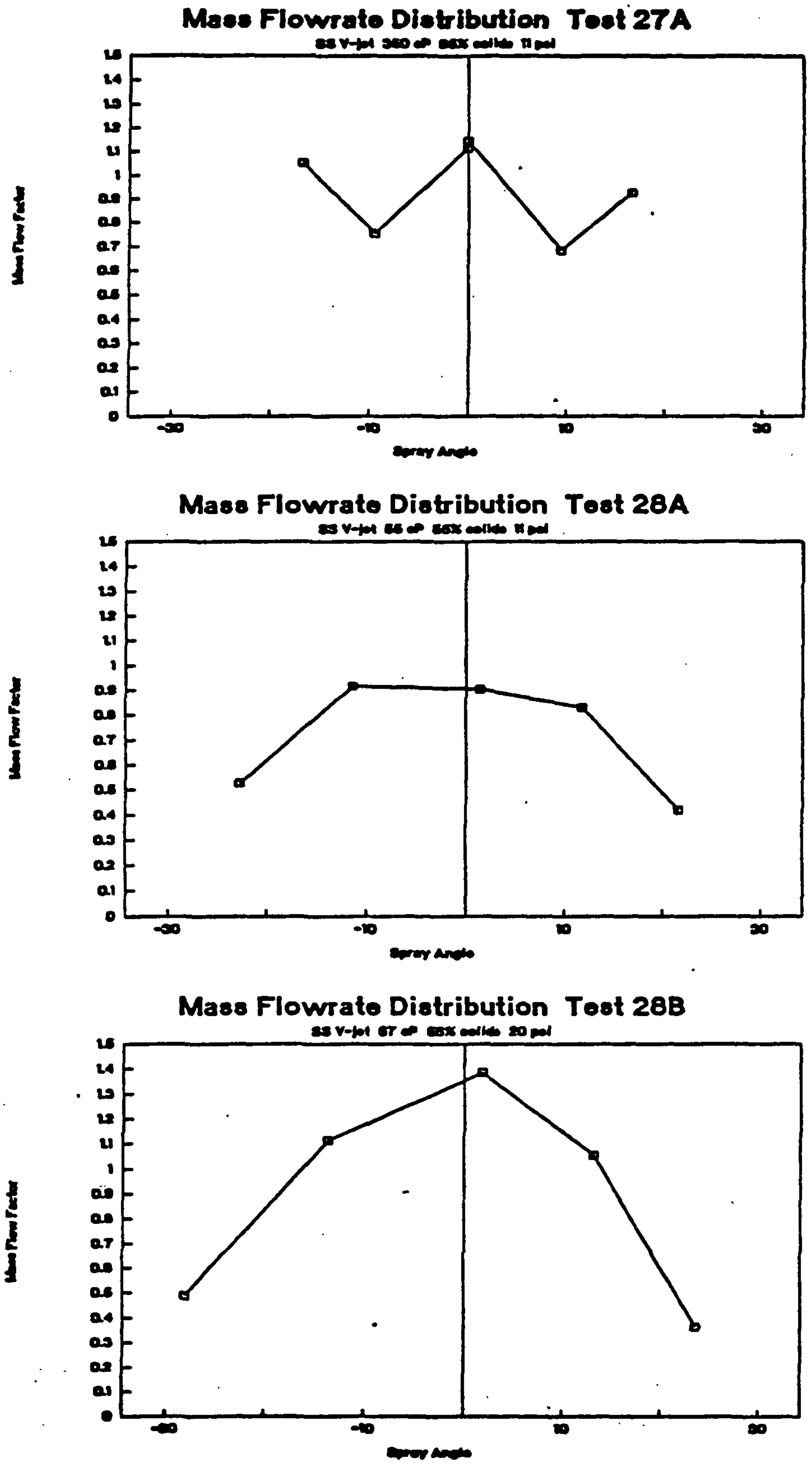

Mass Flowrate Distribution Test 27A

SS V-jet 360 cP 65% solids 11 psi

Mass Flowrate Distribution Test 28A

SS V-jet 55 cP 65% solids 11 psi

Mass Flowrate Distribution Test 28B

SS V-jet 67 cP 65% solids 20 psi

Figure 10. Mass Flow Distribution Curves for the SS 11/65 V-jet Nozzle.

3.6.4 V-JET NOZZLE MASS DISTRIBUTION

The spray pattern for the V-jet as shown in Figure 10 is much more sensitive to variations in the test conditions. At low viscosity and pressure (55 cP and 11 psi) the mass distribution is plug flow for much of the spray angle. Increasing the flowrate (67 cP and 20 psi) not only increased the overall spray angle, it also created a higher flow rate at the centerline and a steeper profile.

At high viscosity (350 cP and 11 psi) the mass distribution shows an unusual notched pattern, which appeared to be due to the formation of a thick outer rim and thin region inside of this rim. The Mf values for the V-jet are plotted along with the splashplate data in Figure 11 to provide a direct comparison between these two nozzles. The spray angle for the V-jet is much narrower.

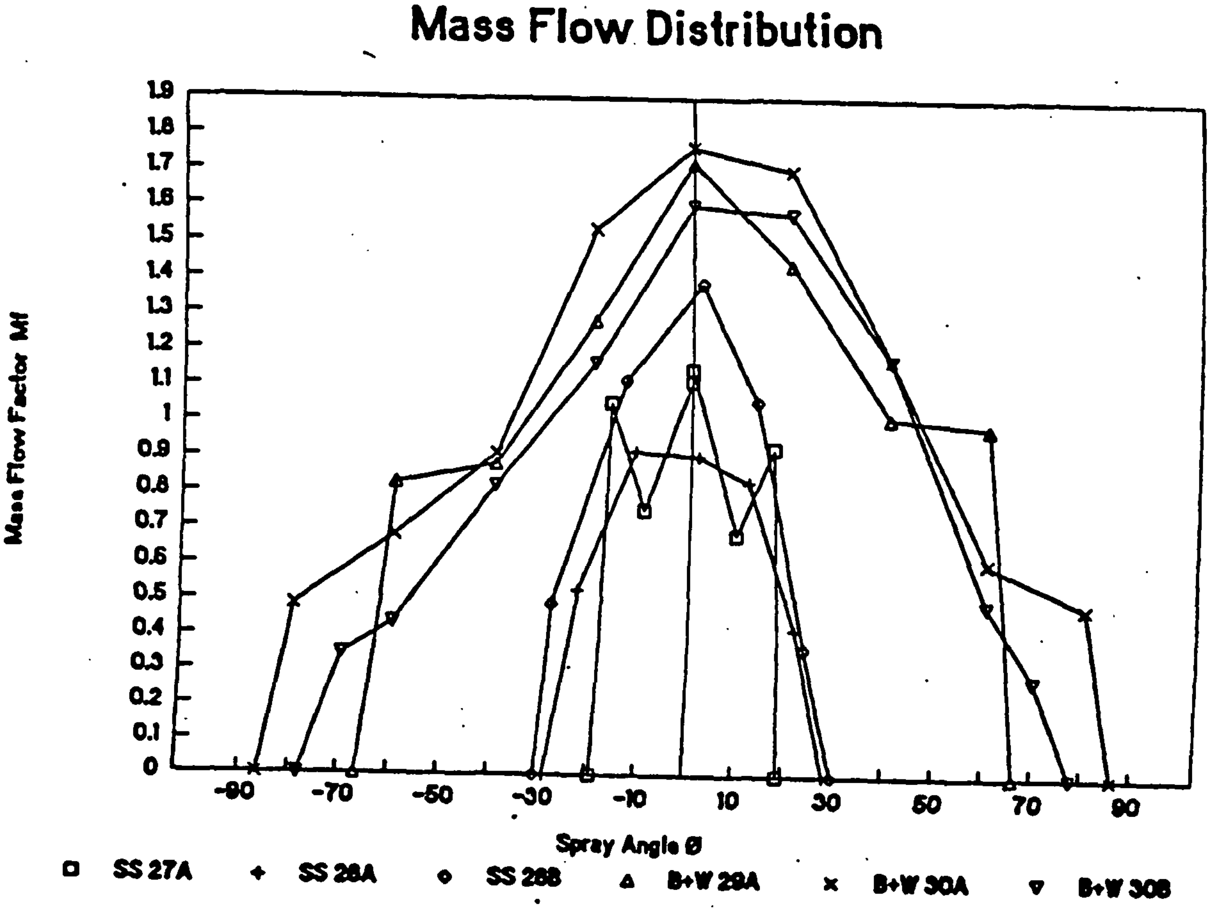

Figure 11. Mass Flow Distribution Comparison

3.6.5 CORRELATION AND ANALYSIS

A correlation of Mf vs. ϕ was derived to provide a mathematical prediction of mass flow distribution for typical operating conditions. A single correlation was derived for each nozzle which is independent of the flowrate and viscosity. The regression analysis indicated that either a linear or a parabolic correlation will produce a reasonable estimate of the mass flow factor Mf. Although the linear correlation has the advantage of simplicity, the slope of the line has a discontinuity at $\phi = 0$, whereas the actual curve is rather flat in this region. The parabolic curve was used, since it more accurately reflects the shape of the experimental curve near the centerline. For the B&W splashplate the correlation is:

$$Mf = 1.537 - 0.000221 * \phi^2 \qquad (32)$$

$$\text{where } \phi = \text{angular position (degrees)}$$

Earlier work on this project measured the sheet thickness and sheet velocity as a function of the spray angle ϕ from the centerline (2). Analysis of these data produced a linear correlation for the velocity:

$$\frac{V}{V_{AVG}} = 1.208 - 0.00584 * |\phi| \qquad (33)$$

$$\begin{aligned} \text{where } V &= \text{local sheet velocity (ft/s)} \\ V_{AVG} &= \text{average velocity (ft/s)} \end{aligned}$$

The mass flow at any point in the sheet is a product of the liquor density, velocity, and cross-sectional area for flow. From equation (31),

$$\begin{aligned} Mf &= \frac{\Delta M/\Delta\phi}{Mt/\alpha} = \frac{V * Z * R}{V_{AVG} * Z_{AVG} * R} \\ &= \frac{V}{V_{AVG}} * \frac{Z}{Z_{AVG}} \end{aligned} \qquad (34)$$

$$\begin{aligned} \text{where } Z &= \text{local sheet thickness} \\ Z_{AVG} &= \text{average thickness} \\ R &= \text{radial distance along sheet} \end{aligned}$$

Using this equation, the sheet thickness can be estimated from the two correlations for mass flow (32) and sheet velocity (33).

Therefore:

$$\begin{aligned} \frac{Z}{Z_{AVG}} &= \frac{Mf}{V/V_{AVG}} \\ &= \frac{1.537 - 0.00022 * \phi^2}{1.208 - 0.00584 * |\phi|} \end{aligned} \qquad (35)$$

The resulting curve for the normalized sheet thickness vs. spray angle is relatively flat in the central part of the spray, which agrees with visual observations of the spray pattern. The curves for all three of these values (Mf, V/V_{AVG}) are shown in Figure 12 below.

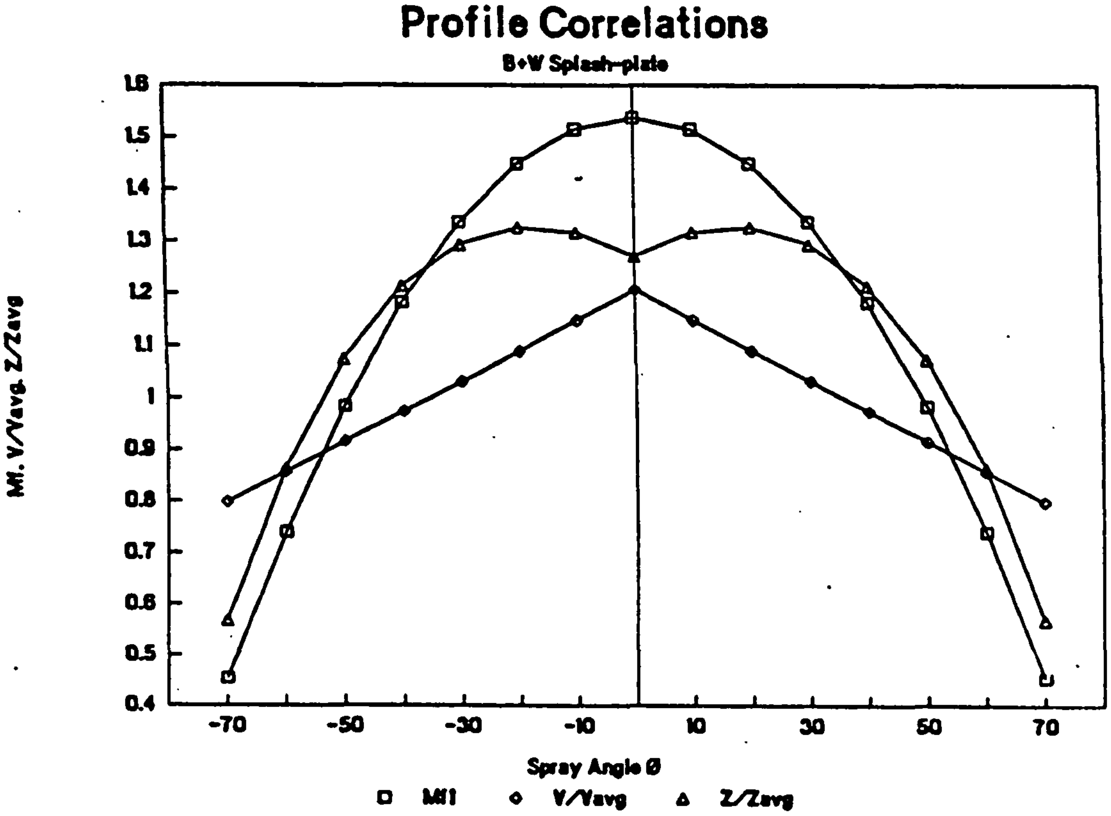

Figure 12. Flow, Velocity and Sheet Thickness Correlations for the B&W Splashplate.

Obuskovic (2) derived a theoretical expression relating the average sheet velocity to the Reynolds Number. This equation, corrected for the splashplate geometry is:

$$\frac{V_n}{V_{AVG}} = 1 + \frac{8}{Re} * \left(\frac{R}{D_n}\right)^3 \qquad (36)$$

where:

V_n = nozzle velocity (ft/s)
V_{AVG} = average sheet velocity (ft/s)
D_n = nozzle diameter (ft)
R = radial distance along splashplate (ft)

By a material balance it can be shown that.

$$V_n * (\frac{\pi D_n^2}{4}) = V_{AVG} R (\alpha \frac{\pi}{180}) Z_{AVG} \qquad (37)$$

where: Z_{AVG} = average sheet thickness (ft)

Inserting Equation (37) into (36), it can be shown that the sheet thickness is also a function of the Reynolds Number.

$$\frac{Z_{AVG}}{D_n} = [(\frac{D_n}{4R}) + \frac{2}{Re}(\frac{R}{D_n})^2](\frac{180}{\alpha}) \qquad (38)$$

Obuskovic (3) fit the actual data points to an equation of this form. For the splashplate nozzles, the average of the ratio (R/D_n) is about 3.0 where R is the distance to the edge of the splashplate. Because the sheet thickness measurements were taken at R-values inside the edge of the plate, the coefficients have been adjusted slightly, to predict the thickness at the edge of the plate. The average coefficients for the sheet thickness are given in the equation below. This equation also includes a correction for the overall spray angle (α).

$$\frac{Z_{AVG}}{D_n} = (0.0883 - \frac{32.6}{Re}) * (\frac{180}{\alpha}) \qquad (39)$$

Combining equations (35) and 39) means that the sheet thickness at the edge of the splashplate can be predicted for any set of operating conditions and spray angle.

$$\frac{Z}{D_n} = [0.0883 + \frac{32.6}{Re}](\frac{180}{\alpha})(\frac{1.537 - 0.00022\phi^2}{1.208 - 0.00584|\phi|}) \qquad (40)$$

Similarly it can be derived from the material balance (for $R/D_n = 3.0$) that the equation for the average sheet velocity is:

$$\frac{V_n}{V_{AVG}} = [1.06 - 392/Re] \qquad (41)$$

Combining Equation (33) and (41) produces the result that:

$$V = V_n * \left(\frac{1.208 - 0.00584|\phi|}{1.06 - 392/Re} \right) \tag{42}$$

The previous analysis applies strictly to the splashplate nozzle. For the V-jet nozzle, no velocity or sheet thickness data are available. Only the mass distribution can be estimated, using the following equation.

$$\mathrm{Mf} = 1.0751 - 0.000957 * \phi^2 \tag{43}$$

5.0 FUTURE ACTIVITY

The final part of this study is to look at alternative technologies for producing black liquor drops, including both those that are commercially available and innovative approaches requiring research and development activity. Both the median drop size and size distribution will be measured in order to determine if a method can be found for controlling these.

Examples of the commercially available type include the Delavan Raindrop ® and Spraying Systems Co. Fulljet ® nozzles. Both are designed to give relatively coarse droplets.

Innovative approaches range from splashplate design modifications (to better distribute liquor flow within the spray sheet) to more complex configurations, such as vibratory assist. Less developed alternatives in this category include vortex shedding and impaction/coalescence.

The experimental work will be completed by the end of August. The final project report will then be written, with DOE funding ceasing at the end of September.

A proposal has been submitted to the DOE for a two-year study aimed at developing and commercializing the most attractive alternative nozzle design concept emerging from the present contract study. Operating characteristics will be fully explored in the IPST spray facility; this will be followed by extensive mill testing on two or more operating recovery boilers.

A second proposal addressing a longer term goal of a commercial delivery system for high solids (i.e. 80%) black liquor will be written and submitted to the DOE. This will require extensive design modifications to the IPST black liquor spraying apparatus.

6.0 REFERENCES

1. Adams, T.N., et al., "Kraft Black Liquor Delivery Systems, Report No. 2," US DOE Contract No. DE-FC02-88CE40839, IPST (Dec. 1990).

2. Adams, T.N., et al., "Kraft Black Liquor Delivery Systems, Report No. 1, "USDOE Contract No. DE-FC02-88CE40839, IPST (Feb. 1990).

3. Stockel, I.H., "Research on Droplet Formation for Application to Kraft Black Liquors," Technical Report No. 4, US DOE Contract No. AC02-83CE-40626, Univ. of Maine (Oct. 1988).

4. Bousfield, D.W., ibid, Technical Report No. 5 (Jan. 1990).

5. Bennington, C.P.J. and R.J. Kerekes, "Effect of Temperature on Drop Size of Black Liquor Sprays," Proc 1985 Int'l Chem Recovery Conf., TAPPI, Atlanta, GA, 345-354 (1985).

6. Lewis, H.C., et. al., Ind. Eng. Chem. <u>40</u>, 67(1948).

7. Galtung, F.L., and T.J. Williams, "An Overall Control System for the Combustion Engineering Recovery Furnace," Proc. Inst. Soc. America, 131 (1975).

8. Whalley, P.B., <u>Boiling, Condensation, and Gas-Liquid Flow</u>, Ch. 5 Oxford Univ. Press, NY (1987).

9. Spielbauer, T., C. Verrill, B. Damon, & T. Adams, "Imaging Black Liquor Sprays in an Operating Recovery Furnace," presented to AIChE Ann Mtg., Los Angeles, Nov. 17-22, 1991.

PROJECT 3671

COMBUSTION OF BLEACH PLANT SOLIDS

RESEARCH REVIEW

MARCH 23, 1992

Kenneth M. Nichols
Donald Sachs
Lucinda B. Sonnenberg

TECHNICAL PROGRAM REVIEW REPORT

Project Title: COMBUSTION OF BLEACH PLANT SOLIDS
(funded by NCASI, Weyerhaeuser, IPST)
Project Staff: K. Nichols, D. Sachs, L. Sonnenberg
Budget (FY 91-92): $140,000
Reporting Period: Jan. '91 - Jan. '92
Division: Chemical & Biological Sciences
Project No./Code: 3671

OBJECTIVE:

Evaluate potential technologies for thermal destruction of chlorine-containing streams and other streams resulting from concentration of bleach plant effluents.

GOAL:

Part of overall IPST program goal to improve pulping and bleaching technology, with emphasis on environmental impact and waste disposal issues.

SUMMARY:

The work is the continuation of research into the feasibility of thermal destruction of chlorine containing concentrates which has been supported by both NCASI and Weyerhaeuser Company. Past efforts have been to characterize various concentrates for the chemical compositions, physical properties, and combustion behavior.

The more recent efforts have dealt with combustion of mixtures of bleach plant concentrates with black liquor. Experimental data show that the combustion rates and HCl emissions for black liquor combustion are not noticeably affected by addition of controlled amounts of E1 concentrate liquor (from ultrafiltration).

Recent combustion tests using the IPST single droplet furnace show clearly that the rate of burning 100% E1 concentrate liquor is dramatically slower (by about a factor of ten) than the burning rate of black liquor. This is explained by the liquor swelling behavior; the E1 concentrate liquor swells much less than black liquor. However, combustion of mixtures of E1 concentrate liquor with black liquor show that the combustion rate is unaffected when the level of E1 concentrate addition is below 25% (wt/wt basis). Comparison of heating values shows that the E1 concentrate solids net heating value (NHV) is at least as great as the NHV of black liquor solids, therefore adding E1 concentrate to black liquor will not result in derating of liquor fuel value.

Measured HCl emissions from lab scale burns of mixtures of E1 concentrate and black liquor showed that HCl emissions were unaffected by addition of E1 concentrate, until the level of addition was greater than 8%. These HCl data, however, are based on less than detectable levels of chloride in the HCl trap used which may have resulted in some masking of real effects. Additional data are necessary to validate these HCl data.

The levels of E1 concentrate addition expected at a typical mill are much less than 8%. Approximate material balance considerations show that if all the E1 effluent in a typical bleached-kraft mill were ultrafiltered, and all of the concentrate mixed with weak black liquor, the resulting liquor solids would consist of about 99% black liquor solids and 1% E1 concentrate solids.

INTRODUCTION

There is a potential for moving toward closed cycle technologies at existing bleached kraft mills. A major technical difficulty slowing implementation of closed cycle technologies in bleach plants is a lack of generally accepted methods for concentrate disposal. Closed cycle technologies such as ultrafiltration, polymer treatment, resin treatment and activated carbon treatment produce concentrated effluent streams that contain high concentrations of lignin, inorganic chlorides, and chlorinated organics. These streams have to be treated either through recycling within the process or in a separate treatment system.

At present the only demonstrated technology for treating these concentrated streams is through additional concentration in multiple-effect evaporators followed by burning in the recovery furnace. A potentially serious adverse impact of burning these concentrated streams in the recovery furnace is the effects of increased levels of chloride and chlorinated organics on the combustion process and its associated emissions. Data are not available on how the addition to black liquor of concentrates high in chlorine will affect flue gas emissions (such as HCl and chlorinated organic compounds).

REVIEW OF PAST PROJECT ACTIVITY (Jan. '90 - Jan. 91)

The efforts of the past year have been focused primarily on characterizing various concentrates. Closed-cycle concentrates were simulated by laboratory-scale ultrafiltration of C/D and E1 effluents from two bleached-kraft mills (both using 30% ClO_2 substitution). Data are presented on the chemical compositions, heating values, viscosities, densities, and combustion rates of these concentrates. The concentrates were found to be very similar to typical kraft black liquor in carbon contents, heating values, and densities. Viscosities of concentrates were similar to or slightly above the range of typical black liquor viscosities. The C/D concentrates contained approximately 20% chlorine (weight % of moisture-free solids) and a molar excess of chlorine over sodium, while the E1 concentrates contained approximately 10% chlorine and a molar excess of sodium over chlorine.

Upon combustion of E1 concentrates in air, all of the organic-bound chlorine was converted to inorganic chlorine and retained in the non-combustible ash. The rate of this chlorine trapping increased with increasing temperature but was zero order with respect to concentration of organic chlorine. The non-combustible ash consisted primarily of sodium, chloride, carbonate, and sulfate and exhibited complete melting at a temperature comparable to the melting point of pure sodium chloride.

Burning rates for the concentrates were found to be similar to previously reported rates for black liquor burning. Isothermal rate data showed rapid initial mass loss due to volatiles evolution followed by less rapid mass loss due to heterogeneous oxidation of char. Volatiles yields were 46-50% (of moisture-free solids), increasing slightly with increasing temperature.

Char yields were strongly dependent on temperature, increasing from near zero at 600 °C to 42% at 1000 °C. Overall burning rates are predicted from a global model which includes a first order rate expression for volatiles evolution and a pseudo-first order rate expression for char burning.

The similarities between concentrates and black liquor suggest that combustion of ultrafiltration concentrates with black liquor in the recovery furnace may be feasible, as long as adequate chloride purge can be maintained to prevent excessive chloride buildup and de-rating of black liquor heating value. Combustion of E1 concentrates in alternative devices appears feasible since the heating values are relatively high (compared with black liquor) and since chlorine trapping will quantitatively convert organic-bound chlorine to NaCl.

DISCUSSION OF 1991 RESULTS

The present year's efforts have been focused primarily on the subject of combining bleachery concentrates with kraft black liquor. Data have been collected on how adding concentrate to black liquor affects the composition, the burning rate, and the HCl emissions.

Elemental Compositions

Samples of black liquor and of the concentrate from ultrafiltration of E1 effluent have been obtained from a bleached-kraft mill pulping softwood. Elemental compositions are compared in Table 1.

Carbon contents and heating values are similar. The E1 concentrate higher heating value (HHV) is somewhat lower, but the E1 concentrate has much less sulfur. When the energy required to convert the sulfur from sulfate to sulfide is accounted for, the E1 concentrate has a slightly greater net heating value (NHV). This is consistent with the earlier reported observation (1) that E1 ultrafiltration concentrates have heating values at least as great as black liquors. This indicates that mixing of E1 concentrate with black liquor will not result in derating of the liquor heating value.

As noted in Table 1, the E1 concentrate has about 20 times more chlorine than black liquor. Approximate material balance considerations show that if all the E1 effluent in a typical bleached-kraft mill were ultrafiltered, and all of the concentrate mixed with weak black liquor, the resulting liquor solids would consist of about 99% black liquor solids and 1% E1

TABLE 1.
ELEMENTAL COMPOSITIONS OF BLACK LIQUOR AND E1 CONCENTRATES

As received compositions, wt/wt% of solids

	Black Liquor	E1 Concentrate
C	36.9	39.2
H	4.71	3.29
O	32.5	32.4
S	4.90	0.51
Na	18.5	14.2
Cl (Org)	--	5.95
Cl (Inorg)	0.46	4.43
HHV	6,320	5,720 (BTU/lb)
NHV	5,250	5,340

concentrate solids. This would give a hybrid fuel with a chlorine content of 0.56 wt/wt%, an increase of 21% in the fuel chlorine level. This would be on the first pass; with recycle in the chemical recovery cycle, the black liquor chlorine concentration would build to greater than 0.46 wt/wt%. The steady state level would depend on the various rates of chlorine purge from the recovery cycle.

Chlorine Trapping

The E1 concentrate composition shown in Table 1 is on the as-received concentrate. Elemental analyses made on the oven dried solids from this concentrate reveal a difference in chlorine content, as shown in Table 2.

TABLE 2.
EFFECT OF DRYING ON CHLORINE CONTENT OF E1 CONCENTRATE

wt/wt% of solids

	As Received	Oven Dried Solids
C	39.2	37.0
H	3.29	3.38
O	32.4	31.0
S	0.51	0.51
Na	14.2	12.8
Cl (Org)	5.95	3.32
Cl (Inorg)	4.43	5.20

The organic chlorine content (determined in both cases by AOX) decreased significantly (by 43%) during drying, while the inorganic chlorine content increased. This is similar to the chlorine trapping observation reported earlier (1). The drying was performed at 70-90 °C under a partial vacuum in N_2 gas. The final drying period was when the highest temperatures were used; the solids were heated at 90 °C for about 3 hours. This rate of trapping is consistent with the rate and activation energy reported earlier for trapping observed in the 600-800 °C temperature range.

The increase in total chlorine was not sufficient to account for all of the loss in organic chlorine during drying, indicating that some chlorine was volatilized during drying. This may have been in the form of volatile compounds such as chloroform.

Combustion Characteristics

Previously reported data (1) showed that the char burning rate of E1 concentrate was similar to the burning rate of black liquor. These experiments were conducted using small quantities (50 mg) of moisture-free solids. For consideration of firing concentrate with black liquor in a recovery furnace it is of interest to know how the concentrate burns as a liquor.

Tests were done with the IPST single droplet combustion furnace. Liquor at 65% solids concentration was formed into droplets of 2-3 mm which were suspended on small nichrome wires, and injected into the furnace. Furnace conditions were 800 °C, upflow gas velocity of 2 ft/sec, gas composition of 5% O_2 in 95% N_2. Droplet combustion behavior was recorded by a video camera through the transparent wall of the quartz combustor tube.

Results for burning times are shown in Figures 1-3. Each data point is the average of 5 burns at that condition. Addition of levels up to 100% concentrate had no noticeable effect on drying and pyrolysis times. Addition of up to 25% of bleach plant solids to black liquor solids did not noticeably affect char burning times. Addition beyond 25% resulted in nearly an order of magnitude increase in char burning times.

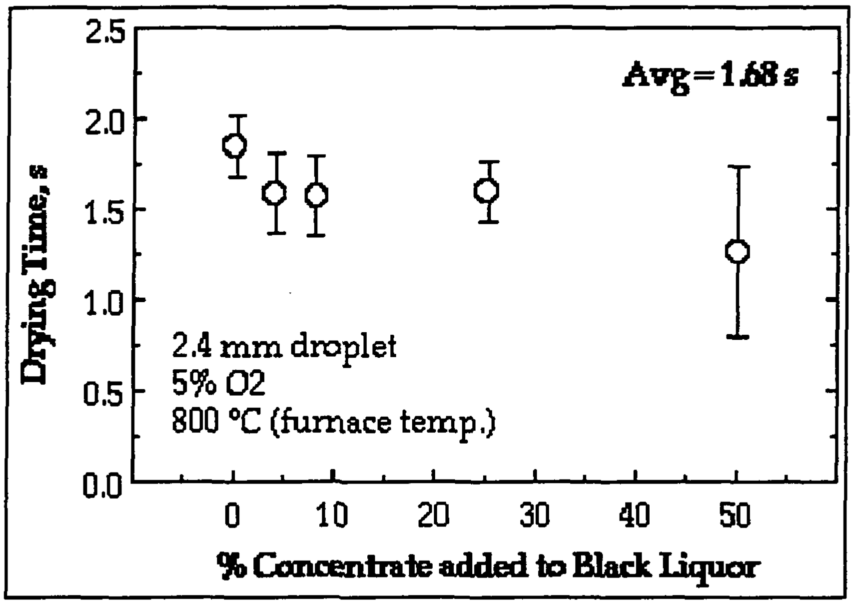

Figure 1. Drying times for mixtures of E1 concentrate and black liquor.

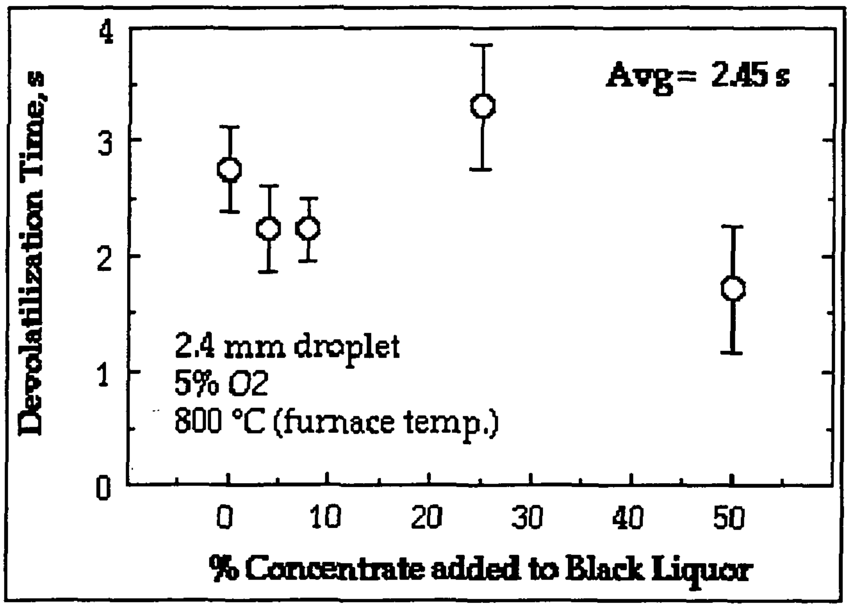

Figure 2. Devolatilization times for mixtures of E1 concentrate and black liquor.

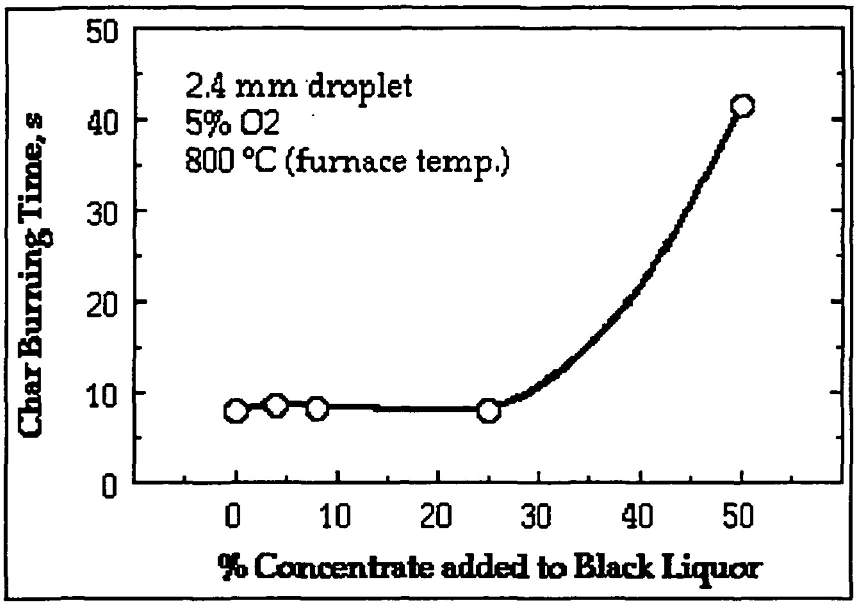

Figure 3. Char burning times for mixtures of E1 concentrate and black liquor.

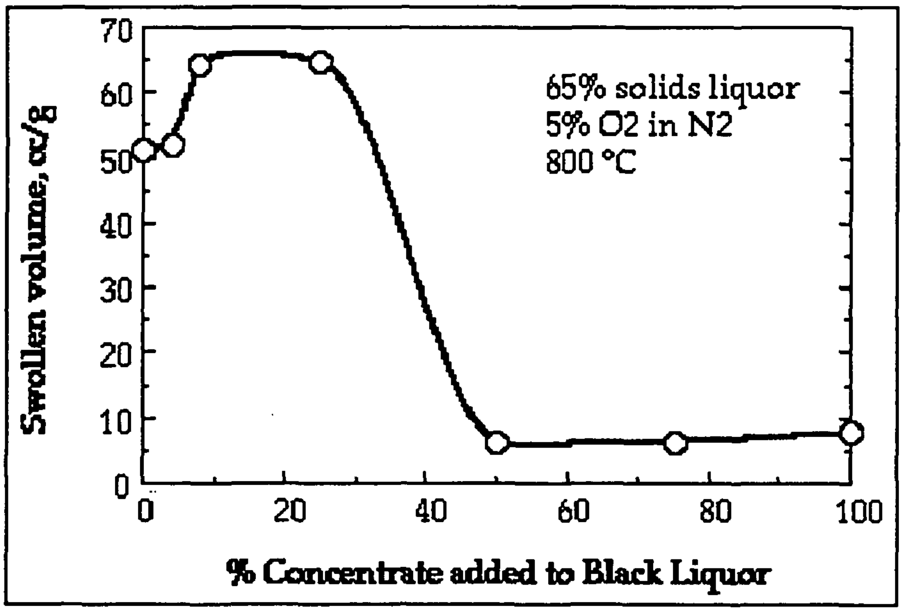

Figure 4. Maximum swollen volumes for mixtures of E1 concentrate and black liquor.

At least a partial explanation for the dramatic increase in char burn time is the swelling behavior. Black liquor droplets swell slightly during drying, and undergo tremendous swelling during devolatilization. It has been shown that liquors which swell less burn slower. The maximum swollen volumes for the test burns with E1 concentrate added to black liquor are shown in Figure 4. At less than 25% addition, swelling actually increased. But at levels greater than 25%, swelling decreased by a factor of ten. With this much decrease in swelling, the char burn time is expected to increase, as seen in Figure 3.

The implications of this data for recovery furnace burning are important. Burning of mixtures at or near 1% (approximately the expected steady state addition level) should not affect swelling or burning time. However, addition at higher levels (> 20%) could have tremendous impacts on swelling, and greatly decrease the burning rate.

HCl Emissions

The HCl emissions from burning mixture of E1 concentrate and black liquor were evaluated using a laboratory scale quartz combustion tube placed in a muffle furnace. The combustion equipment used is shown in Figure 5. Moisture-free solids placed in a ceramic (alumina) boat were inserted into the end of a 2.5 cm ID quartz combustion tube. Air was drawn through the tube at a rate of 5 slpm. The air and furnace temperatures were 800 °C. The product gas was cooled, filtered, and bubbled through an HCl trap. Chloride analyses were made on each of (1) the trap solution, (2) the solution used to dissolve the residue remaining in the boat after the test, and (3) the solution used to rinse out the combustion tube and system up to and including the filter.

The HCl results are shown in Figure 6. The level of emissions for the 100% black liquor were less than 100 ppm. Emission levels did not appear to increase up to 8% addition. It should be noted however, that all of these HCl data (at 8% or less) resulted in less than enough chloride in the trap to measure with the HPLC technique used. Thus, if more sensitive measurement techniques are used, a trend may exist which is not apparent in Figure 6.

Beyond 8% E1 concentrate addition, HCl emission levels increased, to a maximum of about 470 ppm for 100% concentrate. This represents about 5% of the total E1 concentrate chlorine converted to HCl. This is consistent with the earlier reported chlorine trapping data (1) which showed that most all of the organic chlorine was trapped as NaCl rather than emitted as HCl.

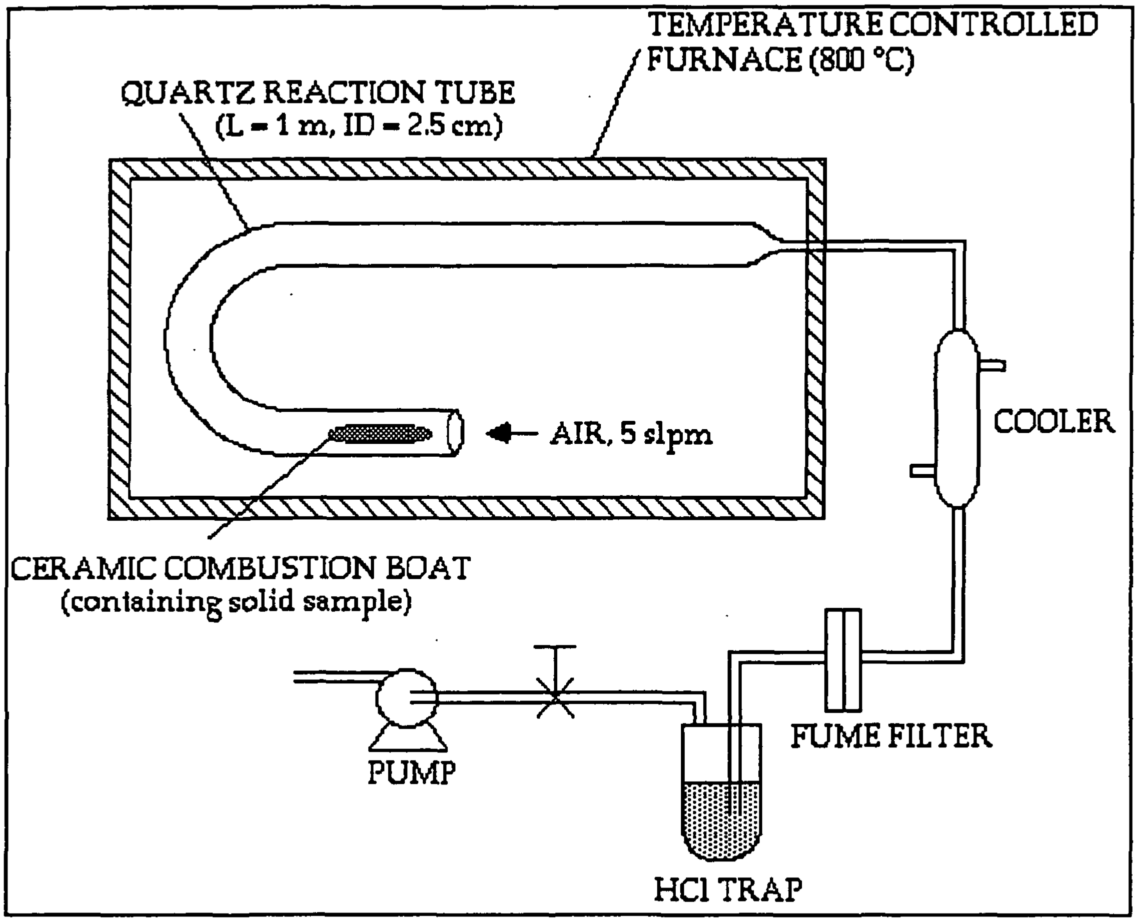

Figure 5. Laboratory scale combustion equipment.

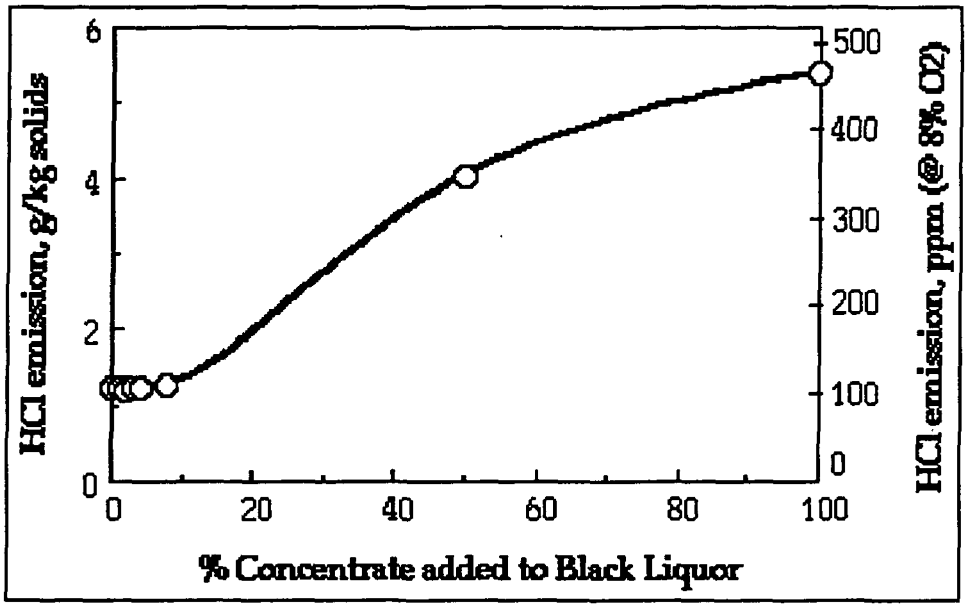

Figure 6. Effect of E1 concentrate addition on HCl emissions from black liquor combustion.

CONCLUSIONS/RECOMMENDATIONS

The implications of this data for recovery furnace burning are important. Burning of mixtures at or near 1% (approximately the expected steady state addition level) should not affect fuel heating value, swelling, or burning time. However, addition at higher levels could have tremendous impacts on swelling, and greatly decrease the burning rate. The combustion rate does decrease dramatically, at addition levels beyond 25%, and HCl emissions increased for addition levels beyond 8%.

The rate of burning for 100% E1 concentrate liquor is dramatically slower (by about a factor of ten) than the burning rate of black liquor. This is explained by the liquor swelling behavior; the E1 concentrate liquor swells much less than black liquor.

FUTURE ACTIVITY

The direction of future work in this area of combustion of bleach plant concentrates is aimed at the study of concentrates from more modern effluents, such as from 100% ClO_2 substitution bleaching, or from total chlorine free bleaching. Efforts will be made to secure samples from mills operating at 100% ClO_2 substitution, and from mills operating total chlorine free bleaching. These effluents will be concentrated (using a technology such as ultrafiltration), and the concentrates will be examined for elemental compositions, heating value, physical properties, combustion rates, and fate of chlorine during combustion. Methods used will be similar to the methods employed in obtaining the data reported in this review, and in the previous work. Other combustion methods besides recovery furnaces will be considered.

REFERENCE

1. Nichols, K. M. The Feasibility of Thermal Destruction of Chlorine-Containing Concentrated Streams from Closed Cycle Processes. Final Report to the National Council of the Paper Industry for Air and Stream Improvement, Institute of Paper Science and Technology, Atlanta, GA (December 1990).

PROJECT 3605

VALIDATED KRAFT RECOVERY FURNACE MODELING CAPABILITY

RESEARCH REVIEW

MARCH 23, 1992

Terry N. Adams
Robert R. Horton
Steven J. Lien
Kenneth M. Nichols

TECHNICAL PROGRAM REVIEW REPORT

Project Title: VALIDATED KRAFT RECOVERY FURNACE MODELING CAPABILITY (Funded by U.S. Department of Energy, American Paper Institute and IPST)

Division: Chemical and Biological Sciences

Project No.: 3605

Project Staff: Terry N. Adams, Robert R. Horton, Steven J. Lien, Kenneth M. Nichols

FY 91-92 Budget: $965,000
(IPST - $601K, UBC - $185K, Frederick - $91K, Grace - $88K)

IPST GOAL:

Increase the efficiency and capacity of kraft recovery boilers.

OBJECTIVE:

Integrate knowledge and descriptions of black liquor droplet and char bed combustion into a comprehensive model of a kraft recovery boiler.

PRIOR RESULTS:

This four-year program was started on September 30, 1990. It involves cooperative research efforts at IPST, the University of British Columbia (UBC), Jim Frederick at Abo Akademi and Oregon State University (OSU), and Tom Grace.

The intention of the recovery boiler modeling project is to produce a computational model which can be used to improve the design and operation of these units. By combining the techniques of Computational Fluid Dynamics (CFD) modeling with combustion modeling specific to black liquor, the processes occurring throughout the boiler can be simulated. CFD modeling focuses on the fluid flow within the furnace and tube banks of the boiler, accounting for the effects on furnace gas flow of air nozzle layout, number, and size along with the effects of char bed shape. Combustion modeling focuses on the individual steps of black liquor droplet combustion, drying, devolatilization, and char burning as well as the steps and chemistry of char bed combustion. Together CFD and combustion modeling can reveal the detailed pattern of black liquor combustion, heat release, fume evolution, and carryover.

During the initial period of this project the detailed analytical models for the steps in black liquor combustion were recast and simplified into models suitable for inclusion in a computational fluid dynamics code. As well, experiments on CO_2/H_2O gasification of char and experiments on fume release during black liquor droplet combustion were initiated. The basic code for fixed-flow-field calculations was also transferred to the IBM RISC 6000 computer located at IPST.

SUMMARY OF RESULTS SINCE LAST REPORT:

The individual steps in black liquor droplet combustion are now well understood and reliable models describing each step have been developed. Black liquor is notorious for the range and variability in its combustion behavior. However, the key differences in liquor parameters which cause this, such as the degree of swelling during devolatilization and the amount of carbon in the resulting char, have been identified. Data are available which establishes the range of most of these parameters so the expected range on combustion behavior can be anticipated and modeled.

The description of black liquor droplet combustion is fundamental to developing an overall recovery boiler model. It is a key element in the pattern of heat release and distribution of material to the char bed, walls, gas phase, and entrained carry over. This has been demonstrated by Bob Horton's research on the interaction of gas flow and droplet combustion described below.

The combustion of char beds has been the focus of research at the Institute for several years. Tom Grace has summarized the data on char bed combustion for a paper to be presented at the International Recovery Conference. It is now reasonably established that the rate of heterogeneous combustion of carbon on the char bed with oxygen is limited only by the rate of oxygen mass transfer to the bed. Gasification of char carbon by CO_2 and H_2O also occurs and can be important in overall char bed combustion. The chemical kinetics of the gasification are slower than for oxidation. Tom has identified a range of temperatures over which the control of gasification rate shifts from kinetically controlled to mass-transfer controlled. The methodology for assessing this for particular bed and air system configurations has also been developed.

In the process of analyzing the char bed data Tom has identified other areas of char bed processes which need to be investigated. The physical structure of the bed and the cohesiveness of its top surface are still not well understood. These will be important in determining the char bed shape and its effect on gas flow patterns in the furnace.

Bob Horton has completed the development of the three-dimensional fixed-flow-field model. This model makes use of simple isothermal, non-reacting recovery furnace CFD calculations to establish realistic flow patterns. These patterns include the effects of the char bed and the individual air nozzles at the secondary and tertiary level. These patterns for flow are then fixed along with those for gas temperature and $O_2/CO_2/H_2O$ concentration. The models for black liquor sprays and black liquor droplet combustion are then used with the fixed gas fields to predict the droplet trajectory and pattern of liquor combustion.

Initial calculations with this fixed-field combustion model show that volatile release from the black liquor occurs in a region of relatively low gas mixing. They also show that there are two important pathways for getting deposition of smelt onto the wall surfaces. Further calculations will be needed to test the influence and sensitivity of the predicted results to various spray and combustion parameters.

The issue of recovery boiler pluggage has also been investigated with a CFD code. Previous work on this issue by a number of researchers has shown that gas temperature, surface temperature, and inorganic melting characteristics all affect deposition on superheater and boiler bank tubes. The complex gas temperature profiles in this region have been investigated with a commercially available CFD code. The initial study focused on the influence of the bullnose shape and bullnose size on gas flow patterns. Though the complete results are complicated, a fairly simple interpretation of the effect of the bullnose is possible. The bullnose acts as a nozzle entry to the upper furnace cavity. Changes in the size and shape of the bullnose which would increase the velocity of the gas cause greater penetration of the flow into the upper furnace cavity. This causes the gas to flow through the upper portion of the tube banks and leads to poor utilization of the heat transfer surface.

Ken Nichols has led research in three areas important to recovery boiler modeling: CO_2/H_2O gasification, fume release during black liquor droplet combustion, and NO_x formation in recovery boilers.

The CO_2/H_2O gasification rates for char are important both for in-flight combustion and char bed combustion. The rates are considerably slower than oxidation so could be rate-limiting in many areas of lower temperature and high mass transfer rate. Data has been taken for CO_2 gasification of char and H_2O gasification will be studied next.

Fume release in the recovery furnace is important for convective section pluggage. One of Ken's graduate students has measured the fume release during the pyrolysis stage of black liquor combustion. These measurement corroborate those of Abo Akademi which show that a very large percentage of the fume can be released during this stage. This is contrary to previously understanding of fuming and may explain some of the observations made on recovery boiler concerning the rate of fume release as a function of operating condition.

Finally, a program of study has been initiated on the mechanism of NO_x formation in recovery furnaces. A review of the NO_x formation mechanism has been completed. Initial indications are that temperature levels in recovery furnaces are too low for significant "thermal NO_x" formation, but black liquor nitrogen levels are high enough to account for the observed NO_x levels from the "fuel-bound nitrogen" mechanism. Experiments have been initiated in the large IPST/DOE, black liquor combustion facility to test this initial indication. Both synthetic air (oxygen plus argon) and synthetic black liquor (free of fuel nitrogen) will be used to determine which NO_x formation mechanism is dominant in recovery furnaces.

PLANNED ACTIVITY THROUGH FISCAL YEAR 1991/1992:

Work in each of the research areas will continue. Single droplet work will emphasize sodium and sulfur release rates rather than direct droplet combustion. The issue of mass transfer to the char bed will be investigated both to determine the rate of oxidation and gasification. This rate is important both for overall bed burning and for determining whether kinetic rates or mass transfer rates dominate the gasification rate under normal furnace conditions. Data will also be taken on the kinetic rate of H_2O gasification.

Work on the char bed will also be extended in order to establish important physical aspect of bed combustion. Bed structure and particle entrainment from the bed will both be investigated.

The fixed-field combustion work will be extended to cover a broader range of parameters for sprays and combustion. It will also be extended to other gas flow fields.

The experiments on NO_x generation will be carried out to determine the most probable mechanism, either thermal NO_x or fuel-bound nitrogen.

THE EFFECTS OF BLACK LIQUOR SPRAY PARAMETERS ON COMBUSTION BEHAVIOR IN RECOVERY FURNACE SIMULATIONS

Robert R. Horton, Thomas M. Grace, and Terry N. Adams

The Effects of Black Liquor Spray Parameters on Combustion Behavior in Recovery Furnace Simulations

Robert R. Horton, Thomas M. Grace, and Terry N. Adams

ABSTRACT

A three-dimensional kraft recovery furnace model has been developed in order to investigate certain critical aspects of the in-flight combustion of black liquor sprays. The model determines the composite behavior of many liquor drops as they move through prescribed gas concentration, temperature, and flow fields in the furnace. Realistic gas flow fields can be developed independently of the combustion simulation. For this study a flow field was developed which reasonably portrays the flow field observed in isothermal physical models of recovery boilers including features such as recirculation, channeled flow, and flow in a horizontal plane due to jet interaction.

The combustion model describes the in-flight combustion of the black liquor in terms of volumetric rates of drying, volatile release, and char carbon combustion. These rate fields (or clouds) can be characterized in terms of centroids and measures of dispersion. The combustion model also determines the location and state of the black liquor material as it leaves the gas-phase combustion zone, either by landing on the bed, striking a wall, or carried out the top.

Spray variables which are studied include: mean drop size, breadth of size distribution about the mean, angular width of spray pattern, and angle at which liquor is sprayed into the furnace. The results of these simulations provide quantitative relationships between the spray variables and resultant combustion behavior. Drying zones, volatile release zones, and char burning zones can be defined and their locations varied as a result of liquor spray parameters.

INTRODUCTION

Combustion of black liquor in recovery furnaces is an extremely complex process. Liquor sprays are characterized by broad spacial distribution and broad droplet size distributions. The resulting individual droplets burn in stages while being acted on by strongly non-uniform gas flow patterns. Direct observation or measurement of this process is frustrated both by the physical size of these process units and by the hostile environment in the lower furnace. Computational techniques to model this type of flow and reaction process have advanced substantially in recent years. However, the geometric intricacies of many small air inlet ports and the complication of multistage in-flight and char bed combustion still limits comprehensive modeling of recovery boilers. In order to circumvent some of this difficulty and gain insight into the interaction between spray combustion and gas flows an intermediate approach has been developed. This approach makes limited use of Computational Fluid Dynamics (CFD) modeling techniques to develop a furnace gas flow pattern then uses this pattern in a fixed-flow-field to examine the trajectory and combustion of black liquor sprays.

Recovery furnace processes represent very complex applications for CFD techniques. However, without the liquor spray and with non-reacting, isothermal flow the recovery furnace problem becomes tractable with commercially available CFD codes. The accuracy of the predicted flows can still be tenuous depending on the selection of the grid layout and assumptions concerning turbulence models and other factors. There have been many recent attempts to mathematically model (1-7) and physically model (8-13) recovery furnaces. Many of the larger features of recovery furnace flows are now well established such as: dominantly channeled flow, high velocity horizontal air jets, and multiple recirculation zones. However, neither the detailed flow generated by a specific air system nor an understanding of what constitutes an optimum flow is yet available. For the present purposes any flow pattern which captures the general recovery furnace features would be suitable for examination of the degree of interaction between flow and black liquor droplet combustion.

Unlike the flow field which must be based on computed results, ample data is now available to accurately model the characteristics of black liquor sprays (14-18). The process of droplet formation from a specific nozzle flow is a complex one which proceeds in stages. The results of this process can be characterized by relative mass distribution with respect to direction from the nozzle centerline and by the size distribution of the resulting droplets. Both of these have been investigated for commercially available black liquor nozzles.

The purpose of this paper is to present the results from the fixed-flow-field model for the impact of spray characteristics on the distribution of black liquor droplet combustion within a recovery furnace. The remainder of the paper is divided into three sections. In the Model Description Section, three models will be presented: the isothermal, non-reacting CFD model, the fixed-flow-field combustion model, and the black liquor spray model. Predicted results for a variety of spray conditions will be presented in the Results and Discussion section. Finally, the conclusion derived from the study will be presented in the Conclusions section.

Model Description

Isothermal, Non-reacting, CFD Model

A commercially available CFD code has been used to generate the flow field used in the fixed-flow-field model. The code used was FLUENT v. 3.02 distributed by Fluent, Inc., Lebanon, NH. The description of the geometry and boundary conditions used will be presented below. The case considered involved only the gas flow as there were no sprays or other condensed phase materials specified. The flow was assumed to be non-reacting and isothermal, so calculations involved no heat transfer between the gas and walls or the char bed.

A front and side elevation of the schematic for the CFD model is shown in Figure 1. It shows many of the features found in recovery boilers. The furnace is an open box with square cross section measuring 10 m x 10 m (32.8 ft. x 32.8 ft.). Only one half of the furnace was modeled due to the assumed symmetry across the vertical center plane running from the front to the back of the furnace. The furnace was modeled only to the level of the bullnose at 30 m (98.4 ft.) which is located on the back wall. The bullnose was taken as a flat horizontal plane blocking 40% of the flow area of the furnace outlet. A solid char bed occupies the floor of the furnace. The char bed surface constitutes lower boundary for computational domain. The edge of the bed at the walls is taken at zero elevation. The bed rises to a maximum elevation of 1.8 m (5.9 ft.) at a distance of 4.2 m (13.8 ft.) from the walls forming a truncated pyramid. Air is injected into the furnace from three elevations. The elevation, number, size and spacing of the three air levels is given in Table 1:

Table 1
Specification of the Air System Layout

Air Level	Elevation m (ft)	Number of Ports	Size of Ports cmxcm (in x in)	Spacing
Primary	0.2 (0.66)	Slot	9 cm high (3.9)	Continuous
Secondary	2 (6.6)	6 per wall	33 x 36 (13 x 16.5)	Uniform along wall
Tertiary	8 (26.2)	4 on F/B	33 x 45 (13 x 17.7)	Uniform F/B unl.

The computation of gas flow patterns were carried out using the physical properties for air at 1000°C (1830°F), for the operating conditions listed in Table 2:

Table 2
Specialization of the air system operating conditions

Air Level	Inlet Velocity u/s (ft/s)	Approximate injection pressure Pa (inches of H_2O)	Fraction of Total Air
Primary	50 (164)	1000 (4)	35%
Secondary	78 (256)	2000 (8)	45%
Tertiary	83 (272)	3000 (12)	20%

The computational domain was defined as a 32 x 17 x 62 grid (33,728 nodes) using a nonuniform grid. The k-ϵ turbulence model was used and the solution converged in approximately 10 hours so that the sum of the residuals was less than 10^{-3}. The computer used was an IBM RISC Workstation model 6540 using the AIX operating system.

Output from a CFD calculation involves a very large amount of information; the three components of gas velocity, the pressure, the turbulent energy and dissipation rate of turbulence each for all nodes in the computational field. For the present purposes of obtaining a fixed-flow-field, only the three components of velocity were used. Resulting flow patterns showed some of the features observed in physical models of recovery furnaces: channeled flow and recirculation zones near the walls. Figure 2 shows the constant velocity magnitude contours for a vertical plane running front-to-back and slicing through the line of tertiary air ports closest to the center plane of the furnace. the tertiary jets are quite visible and the recirculation zone particularly on the back wall is visible.

The velocity contours give a somewhat misleading impression of the smoothness of the flow. For comparison, several parcels of secondary air have been traced in Figure 5. These traces show the path taken by the ten small parcels of secondary air as they enter the furnace and are affected by the overall flow and turbulence. Their flow paths are varied and complex. Some go smoothly up and out, but most are strongly affected by turbulent motion and by the tertiary air flow.

Gas flow in the center of the furnace had velocities with large upward velocity components. This feature has been referred to as a high velocity central core or as a chimney effect. In order to further characterize the central core, Figure 4 shows the upward component of velocity plotted versus horizontal position for three locations in the furnace; one just below the liquor guns at 5 m elevation, above the tertiary air ports at 15 m, and another at 25 m just before the bullnose. Upward velocity components as high as 30 m/s were observed in the CFD flow field simulations in the center of the furnace geometry.

Fixed-Flow-Field Combustion Model

The fixed-flow-field was taken directly from the CFD results. Only the three velocity components were used. As a result, the motion of the droplets from the black liquor spray is unaffected by random turbulence. This results in smoother path lines for the droplet trajectories, but there is a potential that the drag and combustion rate could be affected by this. Future work will examine the influence of turbulence on the droplet trajectories predicted by the fixed-flow-field model.

For the results reported here the gas temperature was taken as 1000°C (1830°F). All gas properties used in the calculation of droplet drag are based on the properties of air at this temperature. All three stages of black liquor droplet combustion are dependent on the surrounding gas temperature. Because of this, the assumption of uniform gas temperature at 1000°C (1830°F) somewhat limits the direct applicability of the results. However, this temperature is near that prevailing in recovery furnaces so that trends and sensitivities to spray parameters should be reasonably portrayed.

The black liquor droplet combustion model used here closely follows that proposed by Frederick (19). Some modifications were made in order to account for radiation exchange between the droplet and the surrounding gas, and to account for the potential interference between the char oxidation reaction and the char gasification reactions. These modifications are fully discussed elsewhere (20).

Several parameters in the equations for black liquor droplet combustion are user specified. The values used here are listed in Table 3. These were derived from extensive comparison to data on individual black liquor droplet combustion.

Table 3. Model Parameters Used in Fixed-Field Combustion Simulations.

Firing Solids = 65%
Volatiles Mass Fraction = 45% (based on total solids)
Char Mass Fraction = 10% (based on total solids)
Inorganic Mass Fraction = 45% (based on total solids)
Firing Temperature = 100°C
Solids at Ignition = 95%
Gas Temperature = 1000°C
Gas Emissivity = 0.4
f, fraction of CO as
comb. prod., = 0 (All O_2 forms CO_2)
α, O_2 that reads w/ CO H_2 = 1 (only excess O_2 penetrates)

Gas phase composition
O_2 = 5%
H_2O = 20%
CO_2 = 12%
N_2 = 63%
Fixed Veloxity Field = Mark 1

Black Liquor Spray Model

In this work black liquor spray patterns are described by a droplet diameter distribution function, nozzle exit velocity, vertical angle, and a mass flow distribution according to angle. This spray model is based on research data reported in recent IPST black liquor spray studies. The particular model used here describes a typical splashplate black liquor nozzle where the horizontal spread of the spray (spray width) is large but only a single vertical firing angle is specified. This is depicted in Figure 5.

It has previously been found that black liquor sprays from commercial nozzles follow a square-root normal size distribution. These are usually characterized in terms of a mass-median-diameter, D_M and a standard deviation, σ. The breadth of the distribution could more readily understood in terms of the maximum and minimum diameter. The nature of normal distributions makes it difficult to identify the actual maximum and minimum, so the diameters corresponding to 1.0% and 99% of the mass will be used instead. These will be designated as D1 and D99. A typical value of the median diameter, D_M, is 2.5 mm. For typical black liquor sprays the values of D1 and D99 would be 0.72 mm and 5.34 mm, respectively.

In order to study the effects of the breadth of the droplet size distribution, the standard deviation was increased or decreased by multiplying by a factor, sf. Values of $sf > 1$ leads to broader distributions and while $sf < 1$ leads to narrower distributions.

Diameters of discrete sizes were specified so that they represented an equal mass fraction of the spray. In the simulations reported here 20 different droplet diameters were specified which each contain 5% of the total mass of the black liquor spray.

Black liquor sprays have been found to have mass flow rates that are a function of horizontal spray angle, Φ. In this work a parabolic mass flow profile which gives the fraction of the mass flow as a function of the lateral angle, Φ, was used according to the relationship:

$$\text{mass flow} = 1.537 - 0.000221 \times \Phi$$

RESULTS AND DISCUSSION

Simulation Parameters Investigated

This work investigates the effects of several black liquor spray parameters on black liquor combustion. These parameters are: mass mean diameter, width of horizontal spray, vertical angle of spray injection and individual droplet diameters.

The individual effects of changes in each of these parameters about an arbitrary base case is examined as a preliminary study of sensitivity. It is recognized that these parameters will have coupled or interacting effects on combustion behavior; however, the compound effects of varying two parameters simultaneously are not examined here. A more complete study in the future will examine the interaction of these variables and the potential for optimizing firing parameters.

Base Case Description

The base case simulation was chosen to represent typical operating conditions in a recovery furnace. A relatively wide spray pattern was specified, $\Phi = 70^\circ$ (total 140° spray angle) with 57 discrete angles (2.5° separation). A mean diameter of 2.5 mm was used with a distribution of 20 individual droplet sizes. A total of 1140 droplets (57 discrete angles x 20 discrete diameters) were used to represent a spray from each of four nozzles; one in the middle of each wall at 6 m elevation. Base case conditions are summarized in Table 4.

Table 4. Base Case Black Liquor Spray Parameters

Liquor velocity	10 m/s
Vertical angle	-10°
Horizontal spray width	-70° to +70°, 57 discrete angles
Droplet size distribution	square-root normal
Median droplet diameter, D_M	2.5 mm
Diameter with 1.0% mass less than, D1	0.72 mm
Diameter with 99% mass greater than, D99	5.34 mm
Nozzle location	1 per wall, center, 6 m elevation

Simulation Output

The recovery furnace fixed-field simulations calculate the combustion product released into each cell of the grid. For the combustion simulations presented here, a uniform 30 x 30 x 60 grid was used on a 10 x 10 x 30 m furnace geometry, so that each cell had dimensions of 0.33 x 0.33 x 0.5 m. Four output arrays contain the sum of mass released from all individual droplets for each stage of combustion for each cell. Additional boundary arrays sum the droplet mass that strikes the walls for each of the four combustion stages. The model does not consider in-flight reactions of smelt, so all inorganic mass in the original black liquor ends up on one of the boundaries: the char bed, one of four walls, the bull nose, or the outlet. At the end of each simulation, the sum of component mass released into each cell is normalized with respect to the total component mass of the entire black liquor spray. This means that each of the four arrays including boundaries will sum to 1.0. The in-flight results can be thought of as normalized rates of evaporation, devolatilization (pyrolysis), or char burning at each location having units of lb./cell/hr per lb. total B.L/hr.

The in-flight combustion rate arrays can be plotted using visualization software which displays three dimensional perspective views of the data which resemble color coded clouds. Each point of the cloud would have an intensity and location corresponding to the magnitude of mass transferred and the cell location, with a different color corresponding to each of the four stages of black liquor combustion. Figure 6 shows results for the base case for water, pyrolysis, and char combustion.

The three dimensional data is often easier to interpret if it is presented in two dimensional format. This can be done by summing the data at each horizontal plane and graphing this as a function of vertical position in the furnace. The base case combustion results are presented in this manner in Figure 7. It is observed in this graph that most evaporation takes place in a narrow vertical distance between 5 and 6 meters, while pyrolysis (devolatilization) and char burning are spread out over larger vertical regions. The area under each curve represents the portion of that component which is released into the gas phase during in-flight combustion. Mass that strikes the boundaries are not represented in this graph.

Droplets that strike the wall may be fully combusted (containing only smelt) or partially combusted containing some fractions of water, volatiles, and char. This data can also be summed and presented as a function of vertical position of the furnace. The base case data for wall activity is shown in Figure 8. In the base case it is observed that most of the droplet mass that does strike a wall lands between 0 and 5 m (below the black liquor guns). The droplets striking the lower walls contain significant portions of char, volatiles and some water. This mass may account for 20 to 50% of the inorganic black liquor mass depending on mass median diameter, and can contain a significant amount of uncombusted char and/or volatiles that would burn on the wall or fall to the bed.

Additional mass impacts the walls from 6 m on up to the top of the combustion zone at 30 m at a gradually decreasing rate. Black liquor droplet mass reaching the walls above the black liquor nozzles did not contain significant portions of uncombusted char or volatiles. Combustion reactions at the walls or mass falling from the walls to the bed is not described in these simulations.

Another way to examine the data which also includes bed information is to plot cumulative component mass as a function of vertical height in the furnace. Samples of these graphs are included in Figure 9. The lower curve in each figure represents component mass that strikes the bed ($z=0$) or the walls as a function of vertical position. The upper curve represents total mass including in-flight and wall mass and will approach 1.0 for each component. The offset from 1.0 represents carryover which is usually less than .02 (i.e., 2%) for smelt and zero for water and combustibles.

Finally, a short table of values for carryover and component mass to the char bed is computed in each simulation (see Table 5).

Table 5. Summary of Droplet Fates for the Base Case Simulation

Droplet Fate	Water	Volatiles	Char	Inorganics
In-flight	0.96281	0.80371	0.67394	0
Hit Walls	0.0316	0.1439	0.21063	0.67207
Carried Out	0	0	0.0001	0.01022
Hit Bull Nose	0	0	0	0
Hit Char Bed	0.00557	0.05238	0.11535	0.31751
Totals	1	1	1	1

Mass Mean Diameter Studies

In Figure 10 the carryover is plotted as a function of the mass median diameter. A similar trend was observed by Grace, et al., in earlier simulation studies (ref.). Two different phenomena occur during black liquor combustion which resulted in most of the observed carryover. Very small droplets with diameters of about 0.5 mm burn very quickly (complete combustion in <0.5 sec.) and the small smelt bead that is left over is easily entrained in gas flow. These tiny droplets will often be captured in recirculation zones and ultimately strike either a wall or be carried out of the furnace combustion zone (see trajectories in Figure 11).

The second mode of black liquor combustion that can result in significant carryover occurs when medium-sized droplets are injected at a certain speed and angle so that they enter the high velocity channel just as they go through the final stages of pyrolysis at maximum swollen diameter (see Figure 12). For the flow field used in this study, this type of carryover phenomenon occurred for droplet diameters of about 3.25 mm injected at 10 m/s at a slight downward angle toward the center of the furnace. Larger droplets are dense enough and have enough momentum to pass through the high velocity channel, while smaller droplets are deflected before they reach the high velocity regions.

A third droplet trajectory that produced carryover was also observed. Some small droplets moving towards the char bed surface were entrained by fast moving gases from the primary and secondary air ports and were swept upward and out of the furnace in some cases. The initial size of these black liquor droplets was approximately 1 mm. Most droplets swept up in this fashion impacted a wall before they could be carried out of the furnace, however.

The various phenomena that can cause carryover of black liquor particles can result in a complex relationship when typical droplet diameter distributions are simulated. Highest carryover rates were observed for the smallest mass mean diameters, and lowest carryover rates for the largest diameter droplets. However the relationship is not a simple monotonic decreasing trend of carryover with respect to mass mean diameter. There is a local minimum carryover at about 2.5 mm. for the current simulations.

When inorganic mass accumulation on the walls is plotted versus vertical height for each mass mean diameter in the 3-D plot in Figure 13 it is observed that droplets strike the walls of the furnace in all areas, but they are concentrated in two zones. Larger droplets strike the walls lower in the furnace in a zone between 1 and 3 m. Smaller droplets are concentrated between 5 and 8 m, just below the tertiary air level. The explanation for this is that large droplets at moderately high nozzle velocities have trajectories with only small deflections, thus striking adjacent or opposing furnace walls below the liquor nozzle near the secondary jets. The smaller droplets are thrown back against the wall due to recirculating flows caused by the tertiary jets. Evidence in support of this conclusion is the fact that mass on the lower walls contains uncombusted material while mass striking the walls above the nozzle was primarily inorganic ash only.

As mass mean diameter was increased from 1 to 4mm, the amount of smelt that lands directly on the bed gradually increased from about 30% to 40%. Uncombusted char that lands directly on the bed increased linearly from 0% at 1.5mm to 30% at 4mm. Char to the bed was not significant for diameters of 1.5 mm and less.

Horizontal Spray Angle, Φ

The width of spray pattern was varied from the base case condition of -70° to +70° (spanning 140°) to a narrow spray of -15° to $+<15°$ (spanning 30° total). Simulations were run for mass mean diameters of 1.5 mm, 2.5 mm, and 3.5 mm, with typical size distributions. For the $\approx$2.5 mm Dm simulations, a more narrow spray resulted in a slight increase in carryover from about 1% to 2.5% of total inorganic (see Figure 14). This seems reasonable since a narrower spray pattern would result in a greater percentage of droplets injected straight at the high velocity gases in the channel. A similar effect was observed for the Dm = 3.5 mm case. However, just the opposite was observed for the smaller Dm = 1.5 mm simulation. A decrease in carryover from 3% to 0.25% resulted with narrowing of the spray pattern.

It can be concluded that directing the black liquor spray into the center of the furnace results in less mass to the lower walls. In the case of Dm = 1.5 mm, a more narrow spray directed into the center caused completely combusted particles to be deflected back to the walls between 5 and 10 m.

Very Narrow Droplet Size Distributions

Very narrow distributions about the mass median droplet diameters between 0.5 mm and 4.0mm were also examined at conditions of the base case ($\Phi = 70°$, $\theta = -10°$) The narrow size distribution was simulated by using standard deviations one quarter the size of normal spray distributions. 2 mm droplets resulted in the least carry over (see Figure 15). This result is consistent with typical distribution data. However, the 2mm droplets burned almost completely in-flight sending about 1% unburned char directly to the bed and 8% to the lower walls. When large sizes are used, less combustion occurs in-flight and the droplets strike opposing walls still wet.

Figure 16 shows the per cent carbon by weight in the resulting carryover as a function of initial droplet diameter for the narrow size distribution simulations. It is clear that carryover for small diameter droplets (Dm < 2.5mm) was completely combusted ash and that larger droplets, if conditions caused entrainment, could contain small portions of unburned char. This result helps to differentiate between carryover of large vs. small droplets.

Vertical Spray Angle, θ

The in-flight results for simulations with varying vertical angles are presented in Figure 17. These figures show the intuitive results that in-flight combustion zones for evaporation, pyrolysis, and char burning move upward with higher angles. The wall behavior is presented in Figure 18. At -30°, the larger droplets strike the bed rather than the walls. At +30° a very large portion of the droplet mass (70%) strikes walls between 2 and 8 m.

CONCLUSIONS

A fixed-field approach was used to investigate in-flight combustion of black liquor sprays in a recovery furnace geometry. This work supports the findings of previous investigations that found that carryover is not a monotonic function of black liquor droplet size.

Two different conditions were found to result in higher levels of carryover for the present simulations. One condition involves entrainment of ash from very small black liquor droplets of 0.5 mm to 1.0 mm caught in recirculating flow patterns. Another condition that resulted in carryover occurred when black liquor droplets with moderate original diameters (about 3 mm) were entrained in fast moving gases in the furnace as the droplets swelled during pyrolysis. This mode of carryover resulted in uncombusted carbon being carried out with the inorganic portion of the black liquor.

Changing width of black liquor spray patterns affected combustion behavior by concentrating or diffusing the zone for combustion. Opposite effects on carryover were observed for small versus large droplet diameters as width of spray pattern was decreased. Large droplets tended to be carried out at greater proportions, small droplets to a lesser degree as a more narrow spray pattern was used.

Spraying liquor at higher angles of injection moved combustion activity up in the furnace with less uncombusted volatiles and char going directly to the bed. Spraying at sharp downward angles caused more wet liquor to hit the bed.

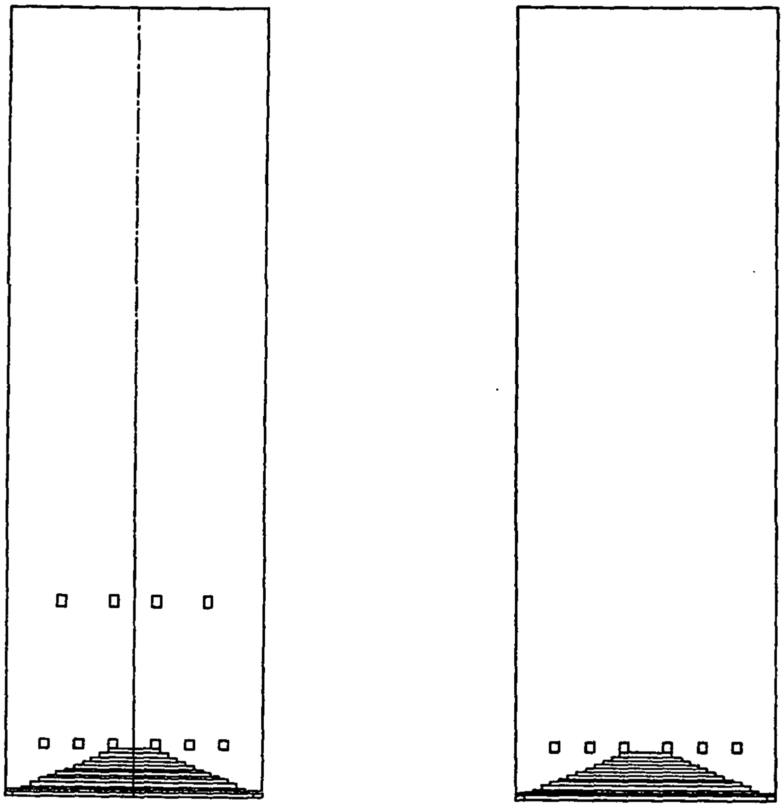

Figure 1. Front and Side Elevation Schematic of Furnace Geometry for CFD Calculations

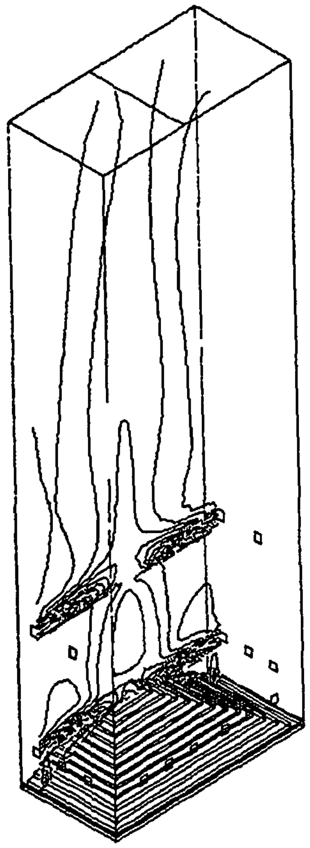

Figure 2. Velocity Magnitude Contours in a Vertical Plane Through Secondary and Tertiary Ports

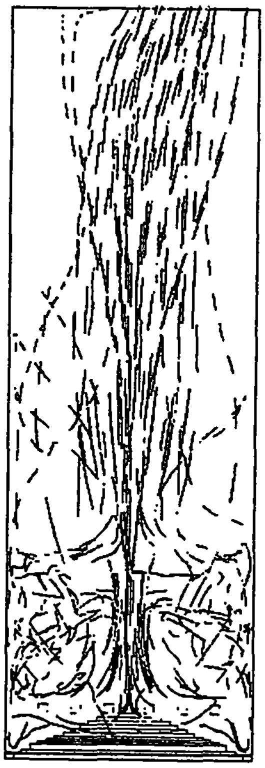

Figure 3. Trajectories of Air Parcels Released at the Secondary Air Ports

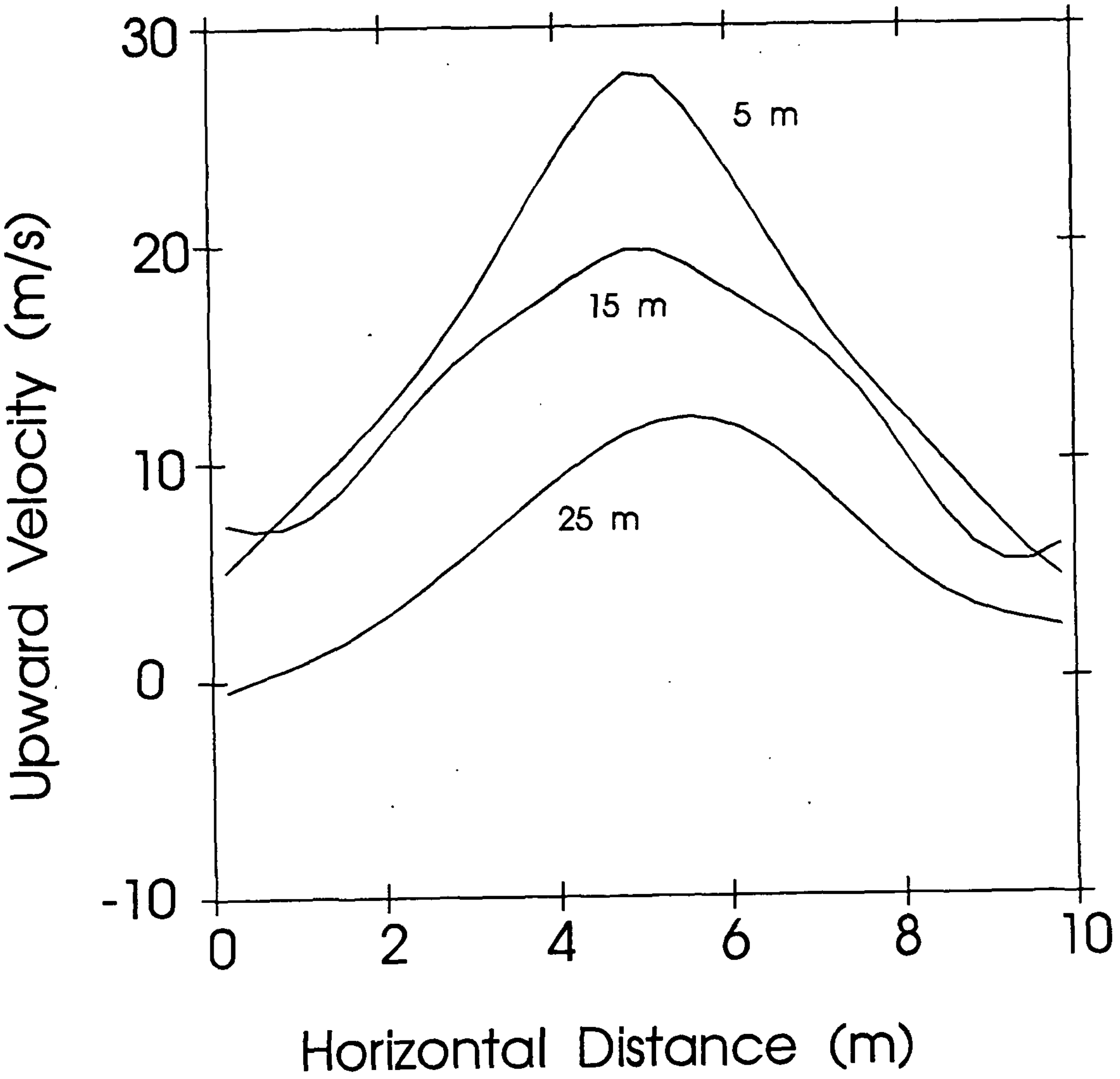

Figure 4. Vertical Velocity Components at Three Levels in the Furnace

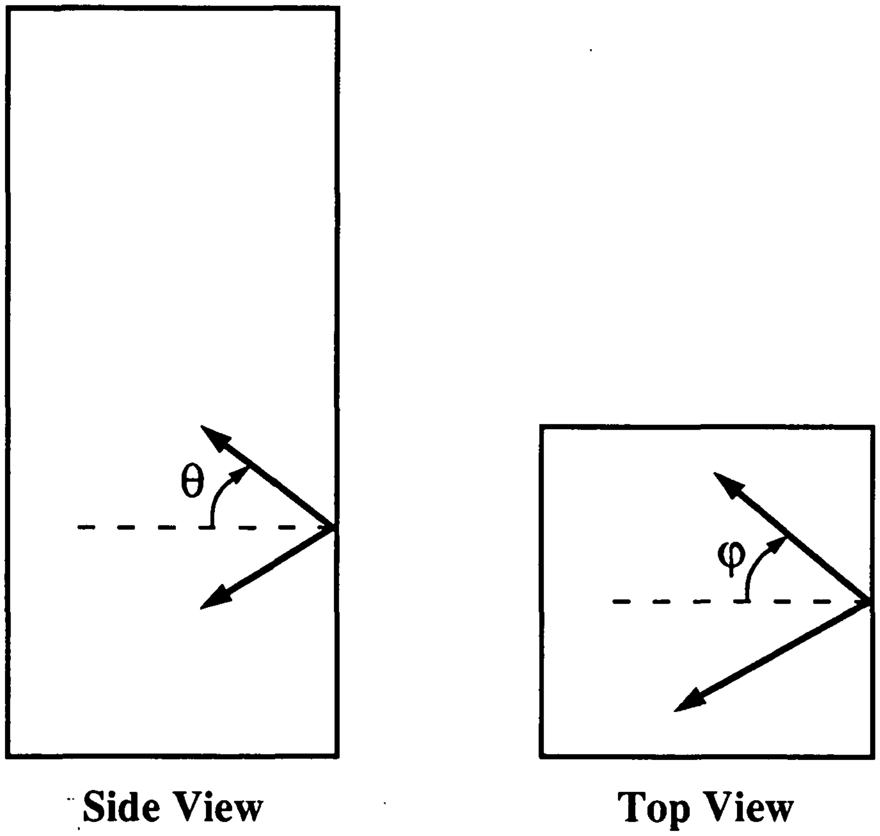

Figure 5. Top and Side Views of Black Liquor Nozzle Spray Angles

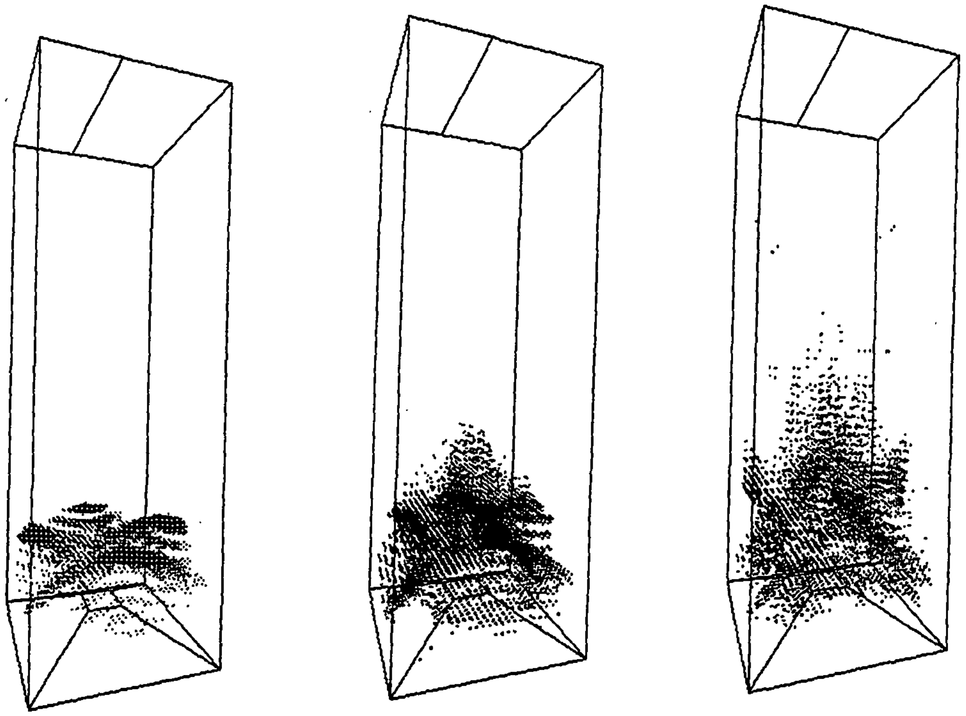

a) Evaporation Rate b) Pyrolysis Rate c) Char Burning Rate

Figure 6. Three Dimensional Views of Evaporation, Pyrolysis, and Char Burning Activity for the Base Case

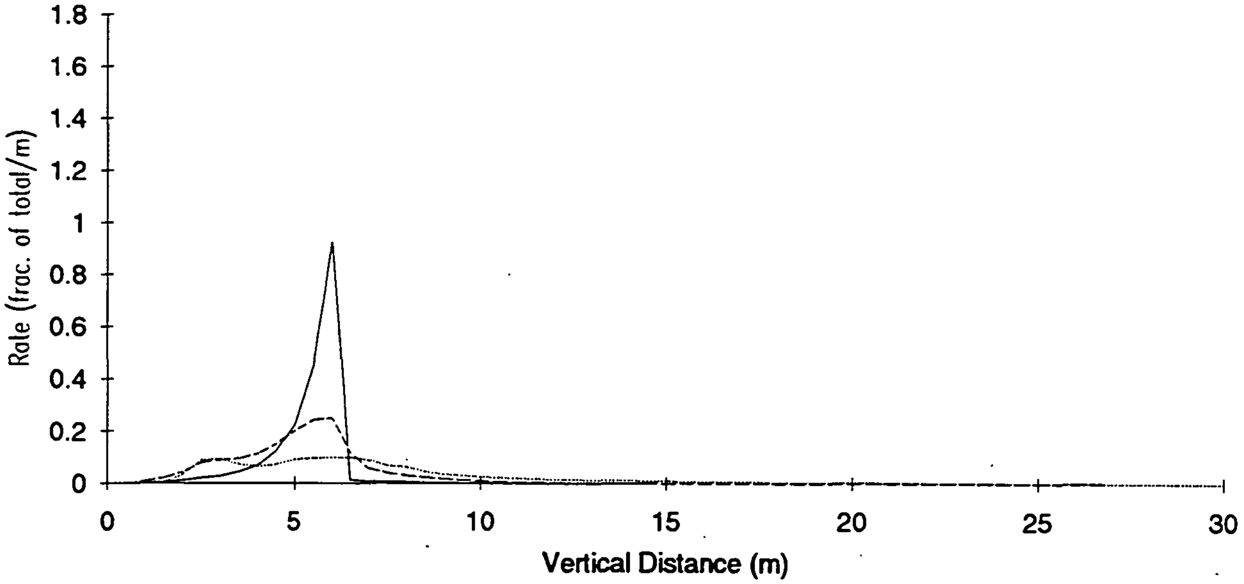

Figure 7. In-flight Combustion Rates as a Function of Vertical Position in the Furnace for the Base Case

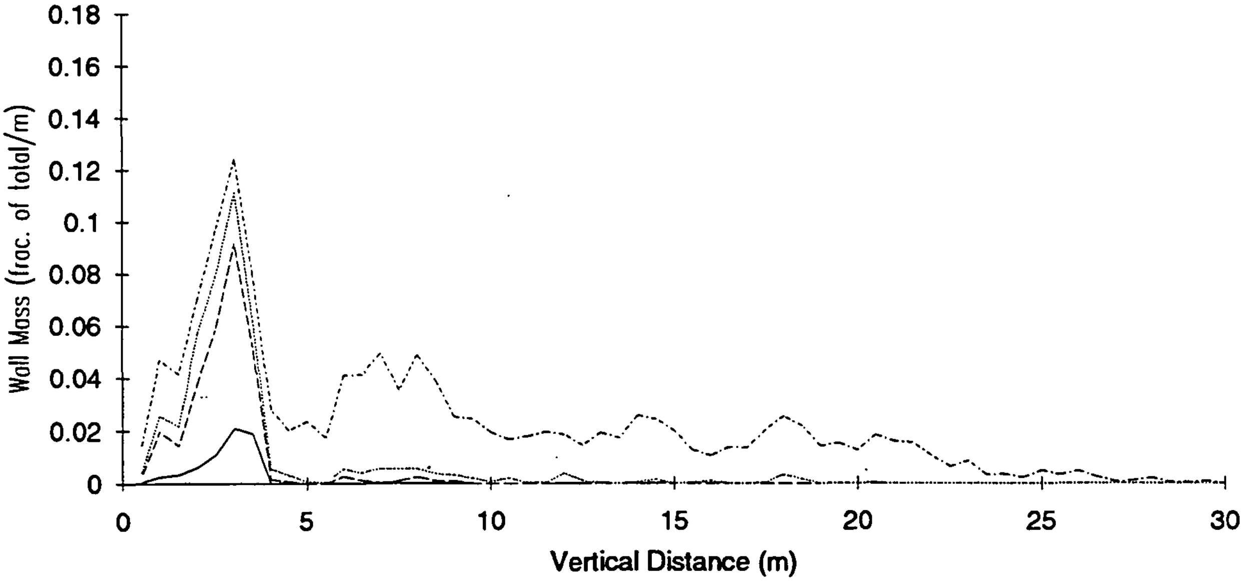

Figure 8. Black Liquor Mass that Strikes the Walls as a Function of Vertical Position in the Furnace

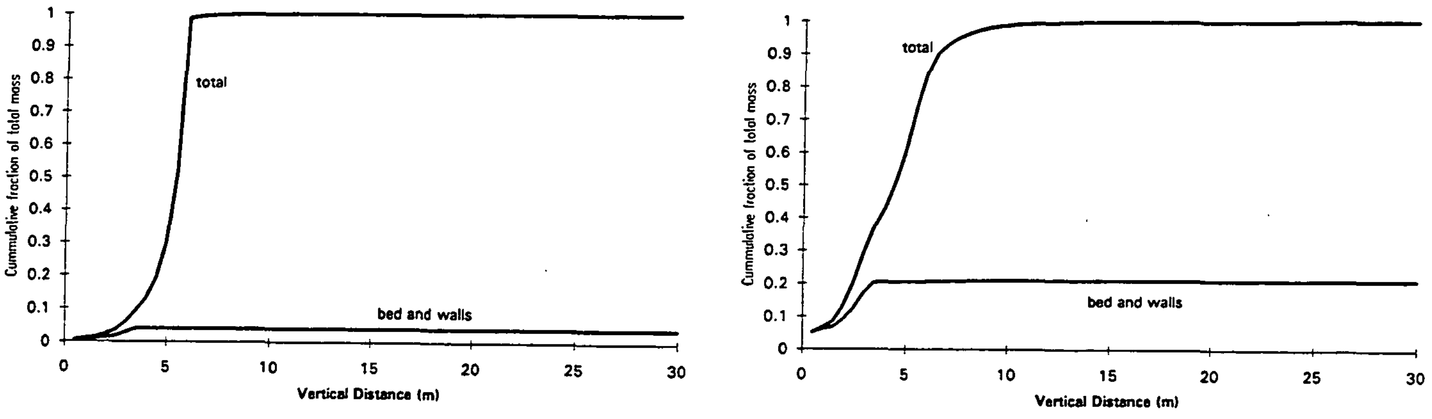

a) Evaporation

b) Pyrolysis

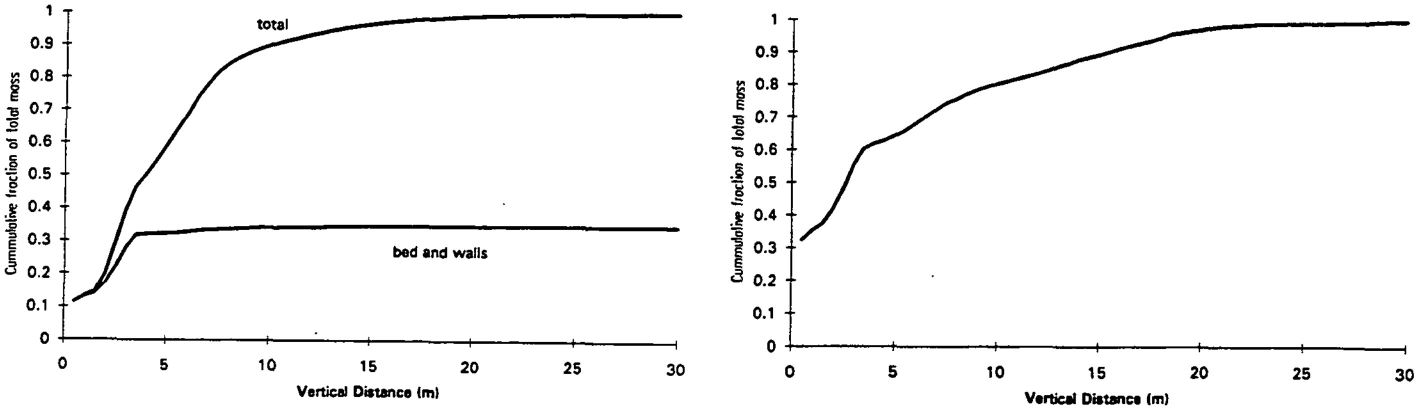

c) Char Burning

d) Inorganic Ash

Figure 9. Cumulative Mass Plots for the Four Stages of Black Liquor Combustion as a function of Vertical Position in the Furnace

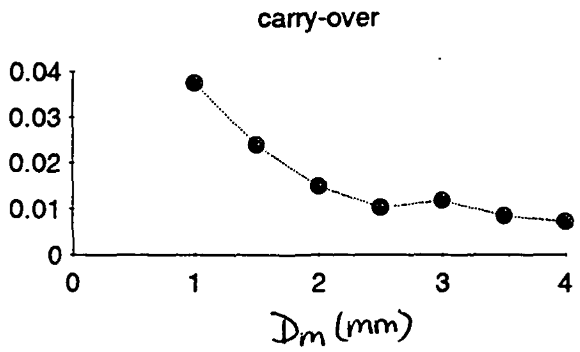

Figure 10. Carryover versus Mass Mean Diameter

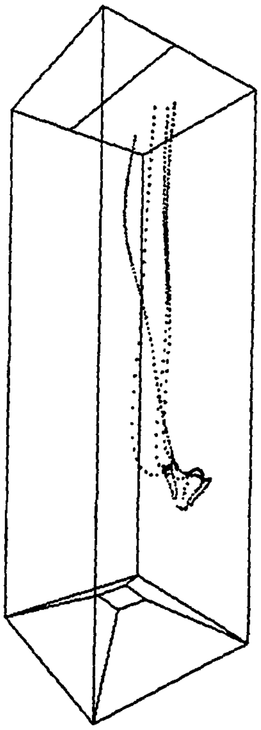

Figure 11. An Example of Small Droplet Trajectories that Result in Carryover

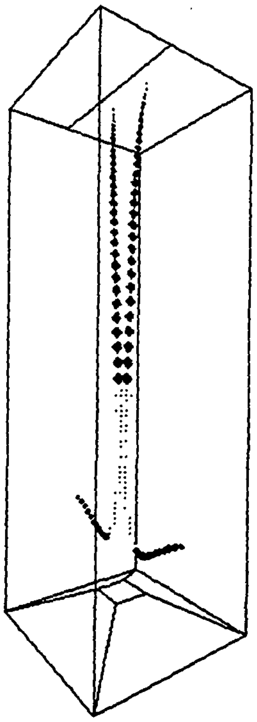

Figure 12. An Example of Large Droplet Trajectories that Result in Carryover

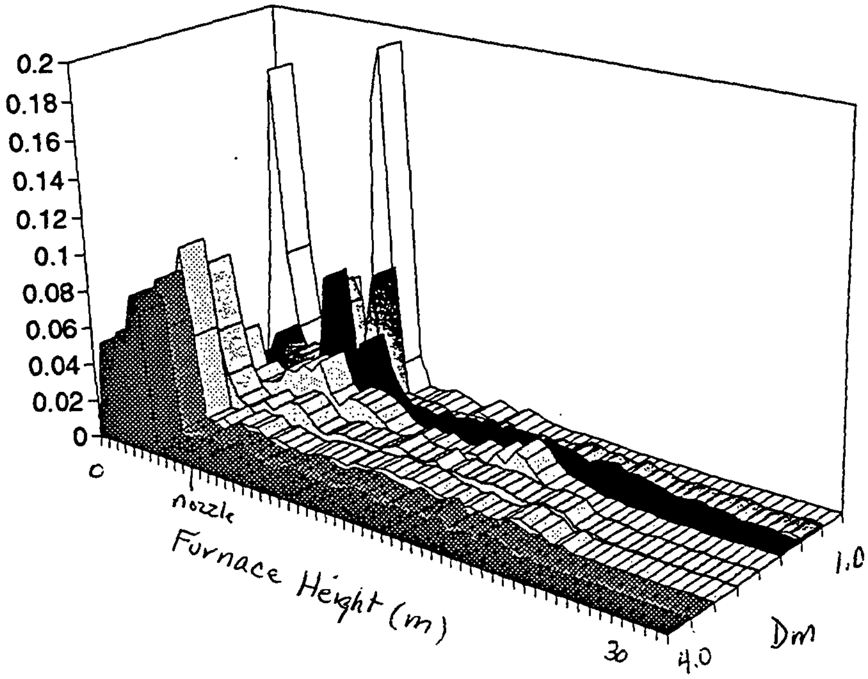

Figure 13. Inorganic Ash that Strikes the Walls as a Function of Droplet Size and Vertical Position in the Furnace

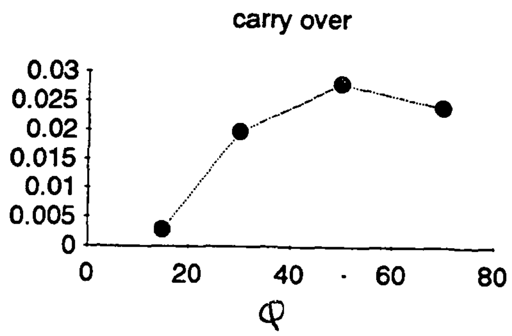

a) Dm = 1.5mm

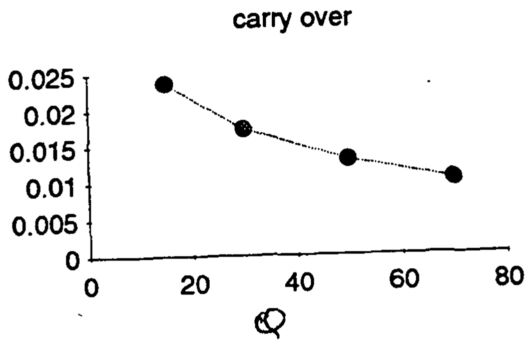

b) Dm = 2.5mm

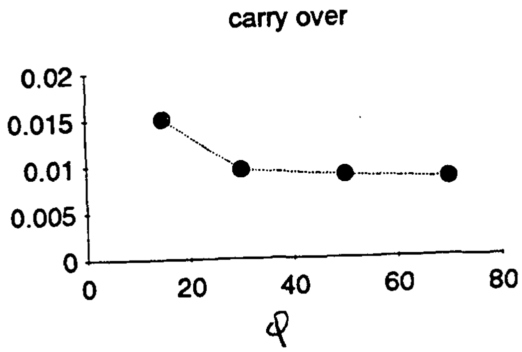

c) Dm = 3.5mm

Figure 14. Carryover versus Width of Spray Pattern for Three Mass Mean Diameters

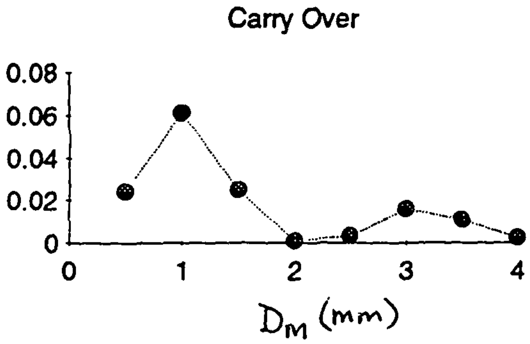

Figure 15. Carryover versus Diameter for Very Narrow Distributions

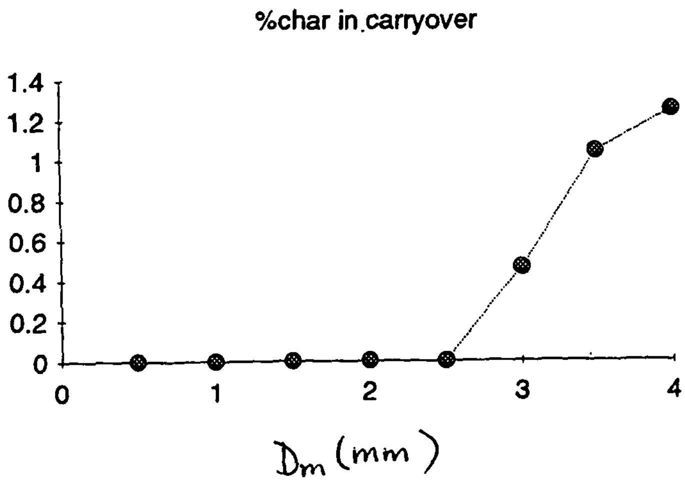

Figure 16. Amount of Char in Carryover as a Function of Droplet Size

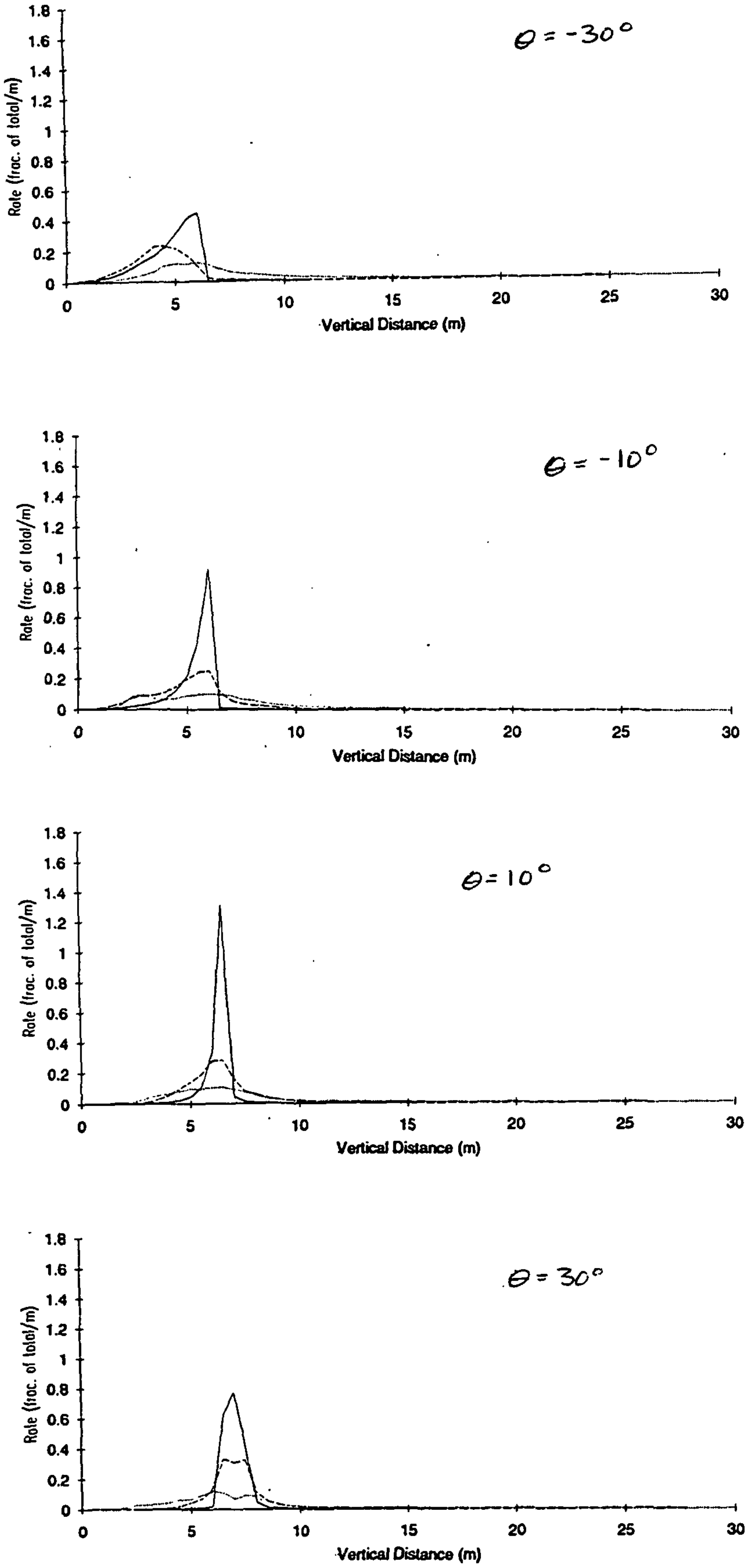

Figure 17. In-flight Combustion Rates for Several Vertical Firing Angles

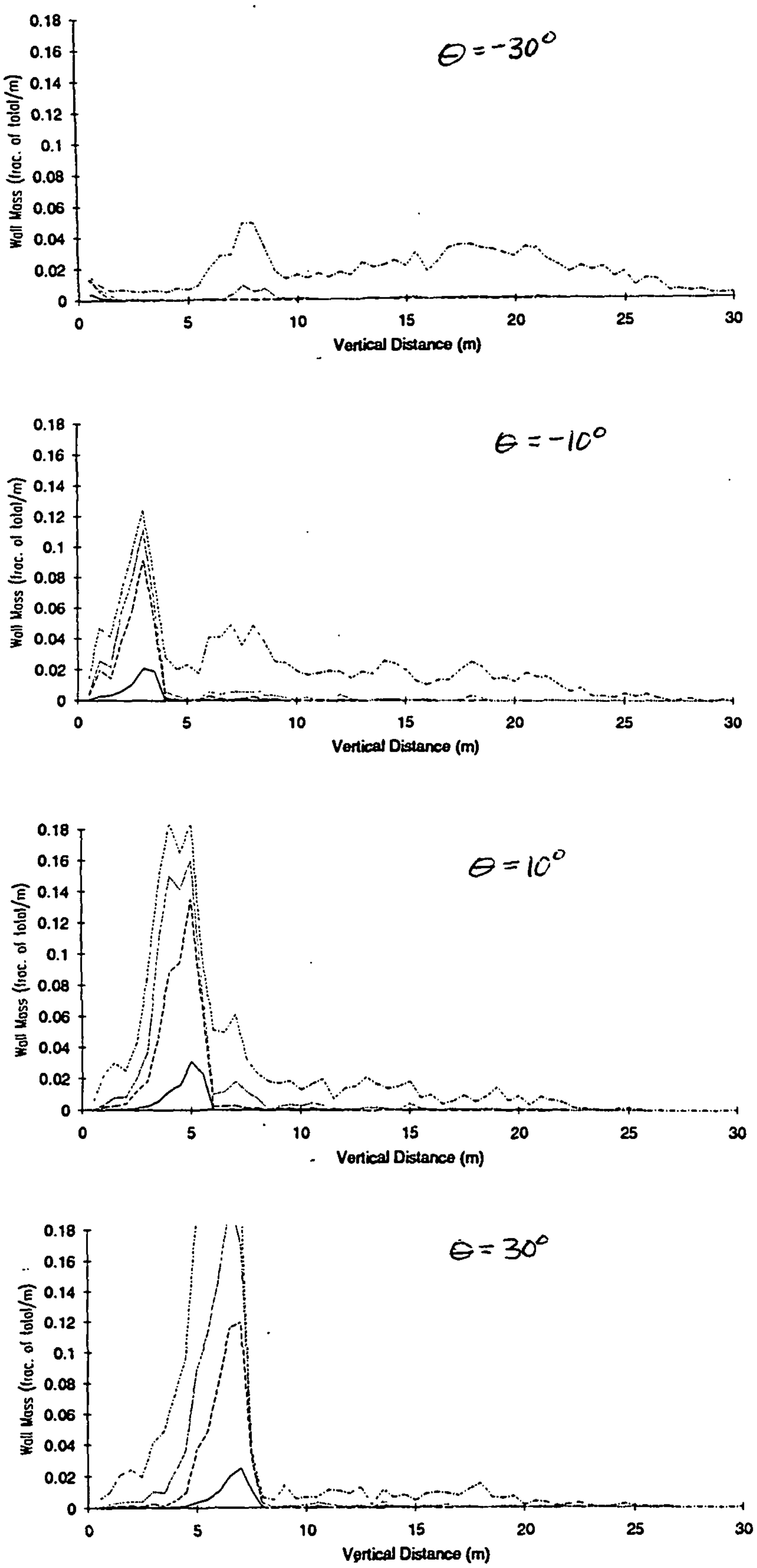

Figure 18. Black Liquor Mass that Strikes the Walls as a Function of Vertical Firing Angle

REFERENCES

1. Williams, T.J. and Galtung, F.L., "A Mathematical Model of a Recovery Furnace", Proceedings ISA/75, Milwaukee, WI, 1975.

2. Merriam, R.L. Kraft, *ver. 2.0* - Computer Model of a Kraft Recovery Furnace, A.D. Little, Inc., Cambridge, MA, 1980.

3. Shiang, N.T. and Edwards, L.L., "Kraft Recovery Furnace Capacity and Efficiency Improvement", Tappi Int.Rec.Conf., 1985.

4. Shick, P.E., "Predictive Simulation of Recovery Furnace Processes on a Microcomputer", Kraft Recovery Operations Seminar, Orlando, FL., 1986.

5. Grace, T., Walsh, A., Jones, A., Sumnicht, D. and Farrington, T., "Three-Dimensional Mathematical Model of the Kraft Recovery Furnace", CPPA/TAPPI Int. Chem. Rec. Conf., Ottawa, April 1989.

6. Horton, R.R., "In-flight Black Liquor Combustion Modeling - A Parameter Sensitivity Study", Timberline Colloquium on Recovery Boiler Modeling, Apr., 1991.

7. Karvinen, R., Hyoty, P. and Siiskonen, P., Tappi J. 74(12):171-177 (1991).

8. Blackwell, B., Oliver, R. and Briscoe, B., "Physical Flow Modelling of a Vintage Combustion Engineering Kraft Recovery Boiler", CPPA Tech.Sect.Conf., May, 1989.

9. Perchanok, M.S., Bruce, D.M. and Gartshore, I.S., "Velocity Measurements in an Isothermal Scale Model of a Hog Fuel Boiler Furnace", JPPS, 15(6):212-219, Nov., 1989.

10. Blackwell, B., "Validity of Physical Flow Modelling of Kraft Recovery Boilers", Timberline Colloquium on Recovery Boiler Modeling, Apr., 1991.

11. Jones, A.K., Chapman, P.J. and Mahaney, J., "Improved Air Port Arrangements for Secondary Air Level", 1991 CPPA Annual Meeting.

12. Siiskonen, P., "Cold Flow Measurements in a Recovery Boiler", Timberline Colloquium on Recovery Boiler Modeling, Apr., 1991.

13. Chapman, P. and Jones, A., Tappi Engineering Conference Proc., 1990.

14. Spielbauer, T.M. and Aidun, C.K., Tappi J. 75(2):136, 1992.

REFERENCES (continued)

15. Adams, T.N., Empie, H.L., Obuskovic, N. and Spielbauer, T.M., Kraft Black Liquor Delivery Systems DOE Contract No. FC02-88CE40839. Report No. 1, Feb., 1990.

16. Stockel, I.H., Research on Droplet Formation for Application to Kraft Black Liquors, Technical Report No. 1, DOE/CE/40626-T2, March, 1985.

17. Walsh, A.R. and Grace, T.M., JPPS. 15(3):84-89, May, 1989.

18. Empie, H.L., Lien, S., Yang, W. and Adams, T.N., Kraft Black Liquor Delivery Systems, DOE Report #3, DE-FC02-88CE40839, in press.

19. Frederick, W.J., Combustion Processes in Black Liquor Recovery, Report No. 1, DOE Contract No. AC02-83CE40637, Mar., 1990.

20. Empie, H., Grace, T., Frederick, W., Horton, R., Nichols, K., Medvecz, P. and Verrill, C., Black Liquor Combustion, Report No. 1, DOE Contract No. DE-FG02-90CE40936, in press.

THE EFFECT OF RECOVERY FURNACE BULLNOSE DESIGNS ON UPPER FURNACE FLOW AND TEMPERATURE PROFILES

Esa K. Vakkilainen, Terry N. Adams, and Robert R. Horton

The Effect of Recovery Furnace Bullnose Designs on Upper Furnace Flow and Temperature Profiles

Esa K. Vakkilainen, Terry N. Adams, and Robert R. Horton
Institute of Paper Science and Technology

ABSTRACT

A commercially available computational fluid dynamics code has been used to simulate temperature and flow profiles in the upper, convective heat transfer region of a recovery boiler for different bull nose designs. The convective heat transfer region of the furnace was simulated by examining a zone that begins below the bullnose and ends at the economizer. Superheater tubes and a boiler bank were included as internal wall boundaries in the problem description. A variety of inlet velocity profiles and temperature profiles were used to determine the sensitivity of the results to chosen inlet conditions. Results from this work show that predicted temperature profiles and velocity profiles at the boiler bank and superheater heat transfer surfaces were not affected significantly by these inlet conditions. Two turbulence models were used, the traditional k-ϵ model and an algebraic stress model. Differences in predicted results between turbulence models were minor.

General features of the simulated results agree well with field measurements. Recirculation zones were located above the protruding edge of the bullnose and in the uppermost corner of the upper furnace cavity. The degree to which the bullnose protruded into the furnace had a significant effect on the size of recirculation above the bullnose. A smaller bullnose results in a smaller recirculation zone which results in smoother superheater tube temperature profiles.

INTRODUCTION

Recovery of the pulping chemicals and the chemical energy in dissolved lignin is important to the economic viability of the kraft pulping process. Recovery boilers are specifically designed to carry out both of these tasks. A number of factors may limit the maximum capacity of these units and make increased capacity difficult to achieve and maintain. Pluggage of the convective section of these boilers by low-melting-point solids escaping the lower furnace is one of the most common capacity constraints on Kraft recovery boilers.

The solid material which can deposit on the superheater and boiler bank tubes and cause pluggage is derived both from submicron sodium fume volatilized in the combustion zone and by mechanical carryover of burning black liquor droplets(1). In either case it is the low melting temperatures of the mixtures of sodium compounds which compose these solids that lead to deposition and hardening of material on the tubes in the superheater and boiler bank. The melting temperatures of the fume and carryover lie between the gas temperature and the tube metal temperature existing throughout most of this region. This allows the carryover and fume to be molten or partially molten in flight, but solid when in contact with a tube.

The melting characteristics of fume and carryover materials in Kraft recovery boilers has been extensively studied(2-5). Less well studied are the gas temperatures and flow patterns in this region of the boiler. These profiles are important not only because of the impact on pluggage behavior, but also for corrosion behavior of the superheater tubes and efficient utilization of the tubes in the superheater and boiler bank for heat transfer and steam production.

There are few published studies which specifically address the gas flow and temperature profiles in the convective section of recovery boilers (6,7,8). Direct measurement of gas velocity and temperature in this region of recovery boilers is extremely difficult. High concentrations of semi-molten solid material and complex flow patterns make direct measurement of gas velocity nearly impossible. Temperature measurement is somewhat easier, but very limited access for probes into this region make comprehensive investigation of gas temperature profiles time consuming, expensive, and uncertain. The difficulty of direct measurement on operating recovery boilers suggest the use of physical or mathematical models. Previous work (6,7,8) has been enlightening and encouraged more detailed investigation with a commercially available Computational Fluids Dynamics (CFD) computer code.

CFD codes are now being developed and used to investigate many aspects of the complex flow patterns of recovery boilers (9-15). Modeling the gas flow patterns and black liquor combustion in a recovery furnace is an extremely challenging task. However, commercial CFD codes are available which can reasonably model the less challenging flows associated with the convective section of recovery boilers. This region is characterized as one with a single inlet and exit, no significant chemical reaction and heat release, entrained condensed-phase material which does not significantly impact the gas flow, and, when the sootblowers are inactive, no small localized high velocity jets. This greatly simplifies CFD investigation of this region. The code used in this work was FLUENT v3.02 from Fluent, Inc., Lebanon, N.H. It was run on an IBM RISC Workstation Model 6540.

In any CFD model investigation there are necessarily many assumptions and limitations on the predicted results. The size of grid elements and the suitability of their layout for the selected geometry being investigated is an uncertainty with all CFD investigations. The accuracy of the mathematical description of turbulence is another. More specific to the current investigation is the uncertainty in the inlet flow conditions to the region of interest. As will be discussed below under Model Description, approximately 50,000 computational nodes were used to investigate the flow in a vertical slab section of the boiler extending from below the bullnose to the economizer. A non-uniform grid spacing was used to maintain good resolution while minimizing the number of total nodes. A previous investigation (6) compared CFD predictions of gas flow patterns with isothermal physical model measurements. Satisfactory comparison between predictions and measurements when a similar node spacing was employed indicates that the current node spacing is adequate for the present investigation.

In the previous investigation (6) model results were compared for two different assumptions about the description of turbulence in the flow. One assumption was the widely used κ-ϵ model, the other a modified laminar viscosity model. In the present investigation the predictions using the κ-ϵ model will be compared to a more complex description of turbulence, the so-called algebraic stress model, in order to assess the sensitivity of the predicted results to the turbulence description.

The inlet flow conditions to the region being modeled are those of the upper region of the recovery furnace. These flow conditions are generally not well known. They depend strongly on the geometry of the char bed and the number, layout, and velocity of the combustion air jets. The flow in the upper region of the furnace may contain the remnant of a channeled flow pattern, tangential swirling flow, and recirculation zones. These features can be very strong in the lower furnace near the air jets, but dissipate somewhat due to turbulent shear in the upper furnace. Because the flow in the upper furnace is not well known, the impact of convective section "inlet" flow pattern on gas flow and temperature profiles was investigated by comparing two very different inlet conditions. These inlet conditions will be described below.

The remainder of this paper is broken into three sections. In the first section, a description of the convective section model is presented. The model geometry and physical parameters are presented along with a specification of the individual cases investigated. In the second section the result of the CFD model predictions are discussed and comparison among the cases are made. Finally, conclusions derived from the work are drawn.

Model Description

The tubes which comprise the superheater and boiler bank of a recovery furnace are generally vertical and always laid out in rows aligned with the gas flow path. The superheater tubes are frequently arranged as platens, closely spaced in-line tube bundles. This layout of recovery boiler convective tubes restricts crossflow and gives gas flow in this region a strongly two-dimensional nature. Because of this and the uniform side-to-side spacing of the 20 to 40 superheater platens which constitute a complete superheater section, a significant simplification of the flow model is possible. Instead of modeling the full side-to-side width of the boiler, only a width equivalent to two side-to-side platen spacings is modeled. The actual region contains two superheater platens along with the gas lane between them and half a lane on either side. This region is shown as a shaded area in Figure 1. The region modeled extends from 7.5 m (24 ft) below the bullnose to the outlet of the first pass of the economizer. This gives a three-dimensional region which contains all the geometric features the upper region of a recovery furnace, but is narrow enough to make effective use of 50,000 computational nodes.

One limitation of the physical model of a slab cut from the midsection of a boiler is the necessary assumption that there is little side-to-side, or rotational flow at the inlet plane of the model. The model predictions presented here would then not apply well to recovery boilers with tangential air systems.

The platens of the superheater were modeled as external wall cells with specified temperatures. Because of the grid structure, the platens are rectangular in view and are stairstep trapezoids in side elevation. The bullnose shape is also approximated by a stair step profile. Because of the limited effect of boundary layer shear on these flows, only minor differences in overall flow pattern would be anticipated for this approximation of the relatively smooth bullnose shape. A side elevation of a vertical plane passing through the superheater platens is shown in Figure 2.

Heat transfer between the gas and the superheater and boiler bank surfaces depends on the gas temperature and surface temperature as well as the overall heat transfer coefficient. Both radiation and convection occur between the gas and the surfaces and these heat transfer processes can be affected by gas and surface properties as well as the properties of the deposits which invariably cover these surfaces in a recovery boiler. Because the main emphasis of the present effort is to examine the influence of assumed inlet conditions, assumed turbulence model, and bullnose shape, both the surface temperature and overall heat transfer coefficient were simply specified for each section. The values for each section are given below in Table 1.

Table 1. Overall Heat Transfer Coefficients and Temperatures for Heat Transfer Surfaces.

Section	Heat Trans. Coeff. (Watts/M^2°C)	Temperature (°C)
1st Superheater Section	172	387
2nd Superheater Section	105	417
3rd Superheater Section	132	327
Boiler Bank	177	297

Gas properties required for the calculations are based on those for an ideal gas with a molecular weight similar to air.

All CFD codes attempt to provide a numerical solution of the Navier-Stokes equations and the energy equation. For turbulent flows, a description of the turbulent transport of energy and momentum is required. The well known κ-ϵ model is often used and its limitations and inaccuracies have been extensively studied in the literature by comparing CFD model predictions to measured results. This was done specifically for the convective section of a recovery boiler in a previous study (6). However, to further substantiate that the κ-ϵ model did not cause significant errors in the model results, an alternative, more complex turbulence model was also tried. This alternative model is the so-called algebraic-stress (ASM) model available as a standard option in the FLUENT code. Comparisons will be made below between the model results using the two turbulence models. Except as shown in this comparison all other CFD results were obtained using the standard κ-ϵ model for turbulence.

The flow profile entering the upper furnace region is not well known for any boiler configuration. However, there is good reason to believe that this profile does not significantly impact the flow profile in the convective section. This profile would only be important if the dynamic head due to the flow velocity was a substantial fraction of the actual pressure drop across the convective section of the boiler. The static pressure drop of the gas stream across the superheater section of a recovery boiler is approximately 0.2 inches of WC (50 Pa). The average upward gas velocity in the furnace is about 14 ft/s (4.3 m/s). The dynamic head is equal to one-half the product of the gas density (about 0.018 lbm/ft^3 or 0.28 kg/m^3) and the velocity squared or 0.01 inches of WC (2.6 Pa). This is quite low compared to typical pressure drops.

In order to further test the impact of inlet flow profile on the CFD model predictions the results using profiles were compared. The first profile was uniform both in inlet velocity and inlet temperature. For comparison a parabolic profile at the inlet was assumed. Comparisons of the inlet velocity and temperature profiles for the two assumptions for one firing rate are shown in Figures 3 and 4.

The main purpose of the study was to determine the effect of the bullnose size and shape on the gas flow patterns in the convective section of the boiler. Here the size of the bullnose is indicated by the horizontal flow area in the region of the bullnose compared to that of the open furnace area. Typically the ratio is about 50%. Three values were used in this study 42% (small flow area, large bullnose), 52%, and 62% (large flow area, small bullnose). The shape of the bullnose can also be changed from relatively thin sloping to thick abrupt. In all, three different nose sizes (42%, 52%, 62%) and three nose shapes (sloping, intermediate, abrupt) were examined.

The general operating conditions used in this study were for a boiler firing black liquor at a rate of 14.2 kg/s dry solids (2.7 x 10^6 lbm/d) with a heating value of 14.2 MJ/kg (6100 BTU/lbm) in a furnace of 8.2 m x 8.2 m (27 ft. x 27 ft.) crossection. This yields an average upward gas velocity of 5.1 m/s (16.7 ft/s). For comparison, some runs were carried out at 4.1 m/s (13.5 ft/s). The average gas temperature at the inlet to the region being modeled was taken as 1350°K (1077°C or 1970°F). The base case conditions are intended to correspond approximately to a heavily loaded recovery boiler.

Using the current version of the FLUENT code and configuration of the computer, each case required approximately 24 hours to converge to a point where the sum of all residuals was less than 10^{-4}.

RESULTS AND DISCUSSION

All CFD computations are characterized by voluminous output, values of temperature, pressure, all three components of velocity, and turbulence parameters at each node. For the present calculations with approximately 50,000 nodes this amounts to almost 350,000 numbers. Graphical presentation is mandatory and fortunately the flows in the present cases are predominantly two-dimensional. Both vector velocities and velocity contours will first be presented for the base case and then comparisons will be made with other cases.

The base case consists of uniform velocity and temperature profiles at the inlet, an intermediate 52% bullnose, and the κ-ϵ turbulence model. Shown in Figure 5 is a plot of the velocity contours along the center plane between the two superheater platens. Shown in Figure 6 are the corresponding temperature contours. The velocity contours indicate that the flow accelerates as it approaches the bullnose, then rises well above the bullnose before turning toward the boiler bank. A recirculation zone can be seen along the top surface of the bullnose. There is another small recirculation zone in the upper left-hand corner of the upper furnace cavity, but accurate prediction in this region would not be expected due to the low density of computational nodes in this vicinity. The tightly spaced contour lines immediately in front of and parallel to the boiler bank is due to acceleration of the gas flow in the region of the more tightly spaced boiler bank.

The temperature contours show a more consistent steady decrease in gas temperature as it passes through the convective system to the economizer. The influence of the recirculation zone above the bullnose can be seen on the temperature contours.

Two similar cases were run to investigate the influence of the turbulence model on the predicted flow and temperature patterns. The two cases both used a uniform inlet temperature but a parabolic inlet velocity profile. A direct comparison of the profiles predicted for the two turbulence models is shown in Figure 7 and a similar comparison for the temperature profiles is shown in Figure 8. In both cases the flows and temperature are very similar. Only very minor detailed difference could be found by overlaying the plots for the ASM turbulence model and the κ-ϵ turbulence model. Convergence for the ASM model was much more difficult, taking nearly ten times as long to converge as the case with the κ-ϵ model. This indicates that for these particular flows there is little accuracy benefit from the use of a turbulence model other than the κ-ϵ model, and there is a severe penalty in convergence time. All other cases in this study were carried out with the κ-ϵ turbulence model.

Shown in Figure 9 are velocity plots for four cases: 1) uniform inlet velocity and inlet temperature, 2) parabolic velocity and uniform temperature, 3) uniform velocity and parabolic temperature and, 4) parabolic velocity and temperature. Figure 10 shows corresponding plots for temperature. There are some differences between the profiles, but the very large differences depicted in Figures 3 and 4 for the inlet parabolic profiles are strongly attenuated as the gases pass through the convective section. This is particularly obvious for the velocity at the boilerbank inlet. For the temperature profiles, the 200°C (360°F) difference in inlet temperature between the uniform and parabolic profile is attenuated to only 40°C (72°) at the boiler bank.

The relative insensitivity of the predicted results indicates that uncertainty in the inlet profile should not affect the relative importance of other design parameters on convective section performance. Advantage will be taken of this for the comparison of the influence of bullnose size and shape on flow and temperature profiles.

The effect of bullnose size has been investigated for three sizes. The bullnose restricts the flow area so the bullnose size has been specified in terms of the horizontal open gas flow area at the bullnose tip compared to the plan area of the open furnace. A large bullnose with 42% open flow area has been compared to a medium bullnose with 52% and a small bullnose with 62% open flow area. Each of these cases was run with 5.1 m/s (16.7 ft/s) uniform inlet gas velocity and 1350°K (1077°C or 1970°F) uniform inlet gas temperature. The velocity and temperature contours for the 52% bullnose case were previously presented in Figures 5 and 6. Shown in Figure 11 is a comparison of the velocity contours for the 42% (large bullnose) and 62% (small bullnose) cases. Shown in Figure 12 is the corresponding comparison of the temperature contours.

In both figures it is readily apparent that the larger bullnose (42% case) causes higher upward gas velocity at the bullnose and this results in significant penetration of the flow into the open cavity in front of the superheater. Flow through the superheater in the 42% case is substantially horizontal and there is a much larger recirculation zone above the bullnose. Vertical temperature gradients are much higher for the 42% (large bullnose) case. This would lead to poor utilization of the superheater heat transfer surface, and potentially higher deposition and corrosion. Considering that the purpose of the large bullnose is to protect the superheater tubes from radiation from the lower furnace, it is clear that selection of bullnose size is very much a trade-off between radiation protection and convective heat transfer surface utilization.

The shape of the bullnose can be changed by changing the angle of the upstream face of the bullnose. Three cases were run to investigate the influence of bullnose shape. The base case discussed above had an upstream face angled into the flow at about 45°. A second shape was used which was more abrupt, at an angle of nearly 75°. A third had a sloping nose which also had a slight curve inward to an angle of about 25°. All three cases were run at 5.1 m/s (16.7 ft/s) uniform inlet gas velocity, 1350°K (1077°C or 1970°F) uniform inlet gas temperature, and a 52% open flow area bullnose size.

Shown in Figure 13 are the velocity contours for all three bullnose shapes. The shape of the bullnose is apparent in this figure as is the reason for calling the 75°angle bullnose an abrupt bullnose and the 25° angle a sloping bullnose. The corresponding temperature contours for all three cases is shown in Figure 14.

There are some significant differences between the gas flow contours for these bullnose shapes. This is easiest to see by comparing the size of the recirculation zone above the bullnose. It is larger for the abrupt bullnose than for the sloping bullnose. Likewise, the gas flow through the superheater is more horizontal for the abrupt bullnose, leading to poorer utilization of the heat transfer surface because less is exposed to the main gas flow. This is a situation where the same protection from lower furnace radiation is provided by all three bullnoses, but convective heat transfer utilization is significantly different depending on the abruptness of the upstream face.

The predicted effect of the bullnose shape on the recirculation zone and gas flow can be readily understood by reference to ordinary nozzle flow. The restriction at the bullnose elevation is similar to that for flow through a nozzle or orifice. A smooth approach to the restriction such as the sloping bullnose is similar to a flow nozzle. The abrupt bullnose looks more like a sharp-edged orifice. Well documented flow patterns for the sharp edged orifice show that there is a contraction of flow down-stream from the physical orifice. For a smooth flow nozzle the minimum flow area is at the nozzle itself. Thus for the same flow and same physical open area, the flow is slower and more uniform for the smooth flow nozzle. This is just the case for the convective section flows shown in Figures 13 and 14. The abrupt bullnose causes higher upward velocities, greater penetration of the flow into the upper furnace cavity, and a larger recirculation zone above the bullnose.

CONCLUSIONS

A commercially available CFD code has been used to investigate the flow and temperature profiles in the convective section of a recovery boiler. The uncertainty in the inlet gas flow conditions and the mathematical description of turbulent flows were first investigated. Comparison of the assumption of uniform inlet gas flows to sharply parabolic inlet flows showed that the predicted results for velocity and temperature were insensitive to the precise inlet flow condition. This is reasonable in light of the relatively low initial dynamic head of the upward furnace gas flow. Likewise, comparison of two models for the description of turbulence showed very little impact on the predicted results. As a result, the familiar κ-ϵ model for turbulence was selected for most of the study due to its near factor of ten more rapid convergences.

The effect of the size and shape of the bullnose on gas temperature and velocity was investigated for three sizes and three shapes. Both the size and shape affected the gas flow. The magnitude and direction of the effects can be easily rationalized in terms of the effect of shape and size on gas velocity in the bullnose region and penetration of the gas flow into the upper furnace cavity.

ACKNOWLEDGEMENT

Funding for this project was provided by the U.S. Department of Energy under contract DE-FG02-90CE40936.

One of the authors, Esa K. Vakkilainen, received boiler specifications for the cases run in this study from the Ahlstrom Company. This assistance is greatly acknowledged.

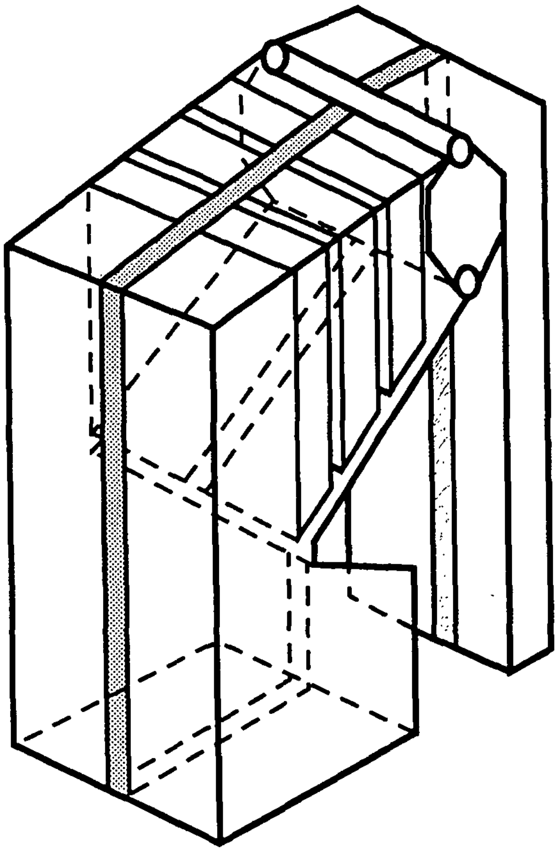

Figure 1. View of a Vertical Slice Through the Convective Section of a Recovery Furnace

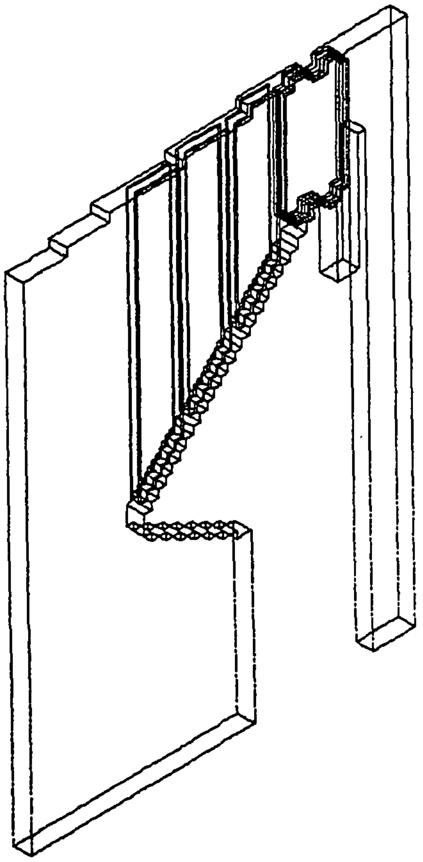

Figure 2. Side View of CFD Problem Boundaries

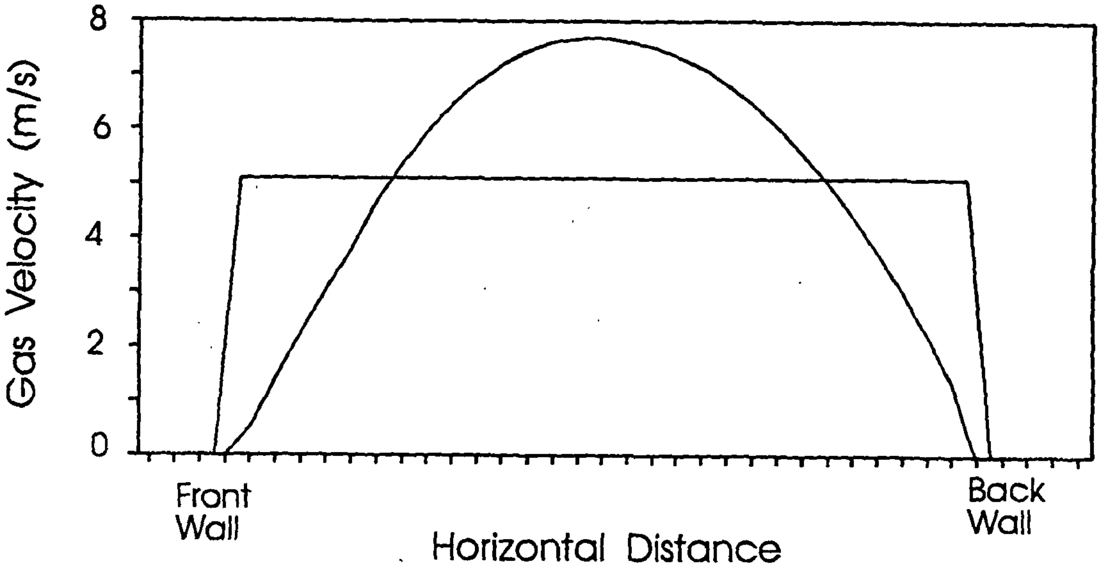

Figure 3. Uniform and Parabolic Inlet Velocity Profiles

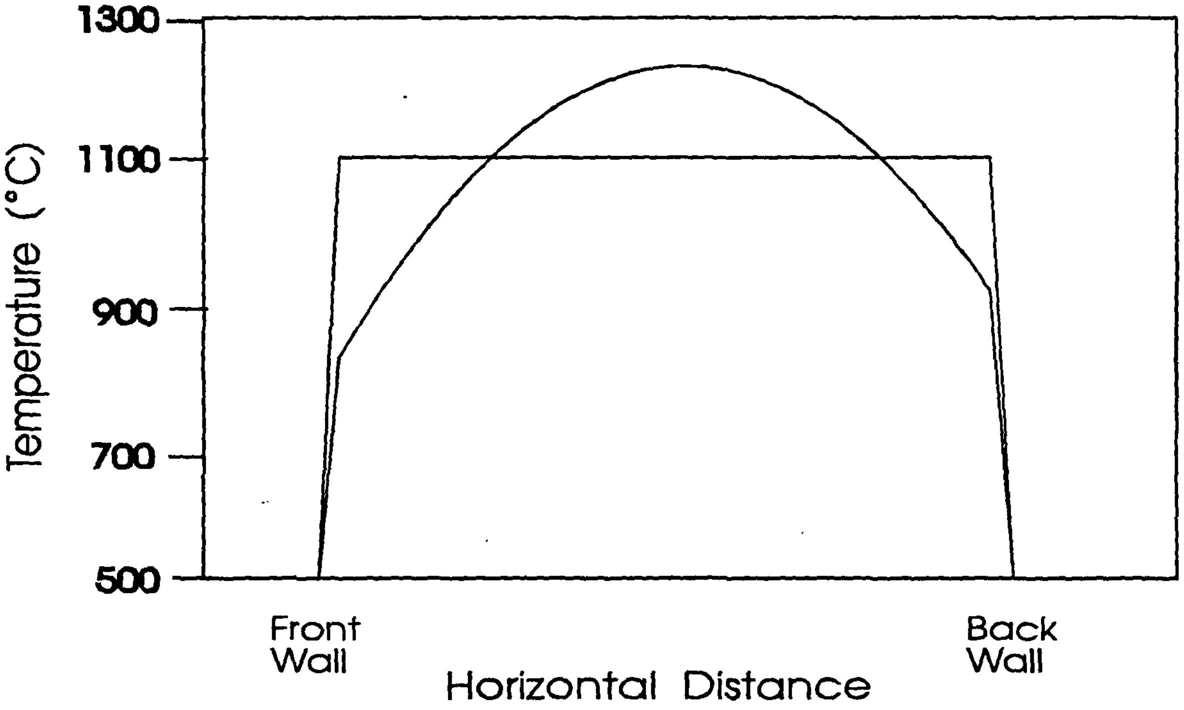

Figure 4. Uniform and Parabolic Inlet Temperature Profiles

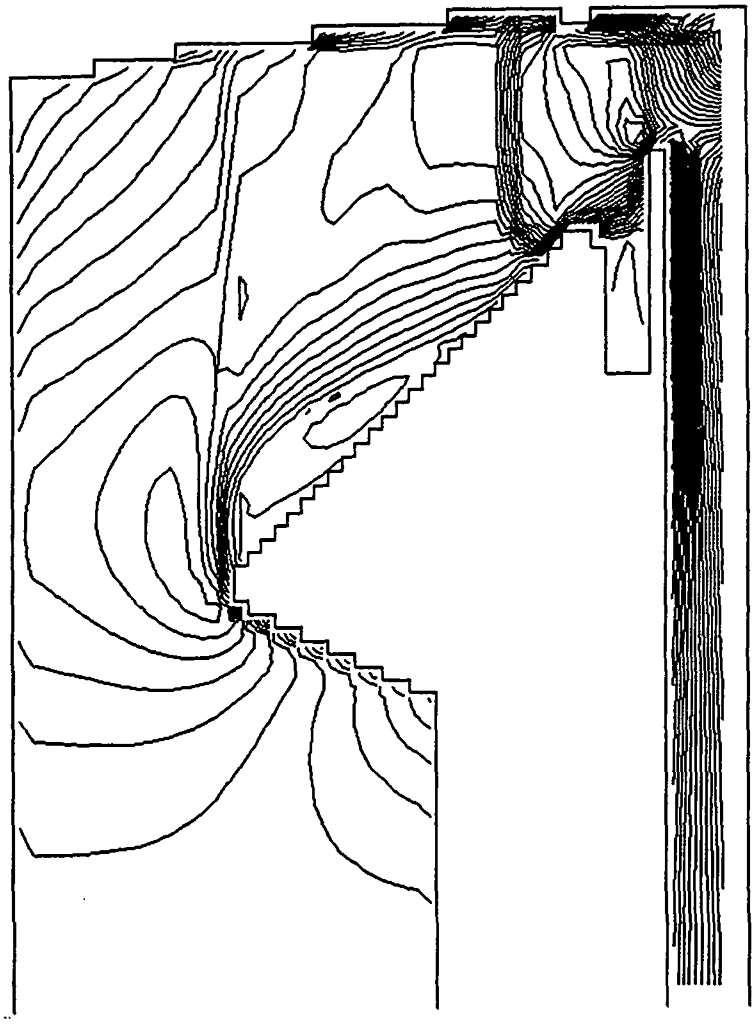

Figure 5. Velocity Contours for the Base Case Simulation with Intermediate Bullnose Size (52% Open Flow Area)

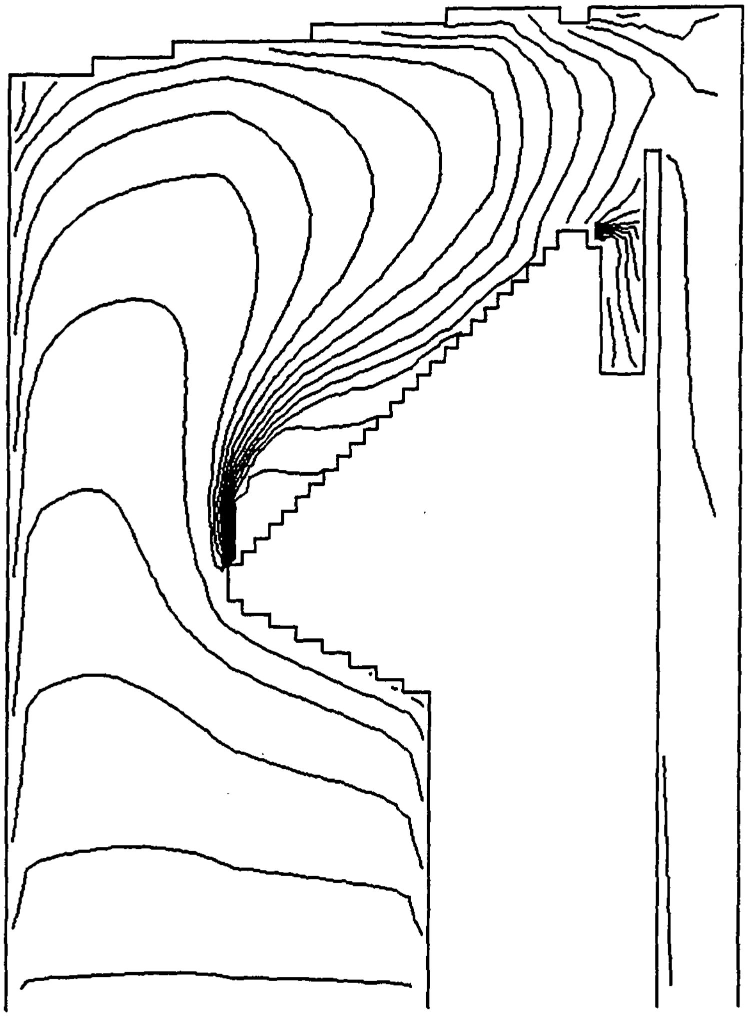

Figure 6. Temperature Contours for the Base Case Simulation with Intermediate Bullnose Size (52% Open Flow Area)

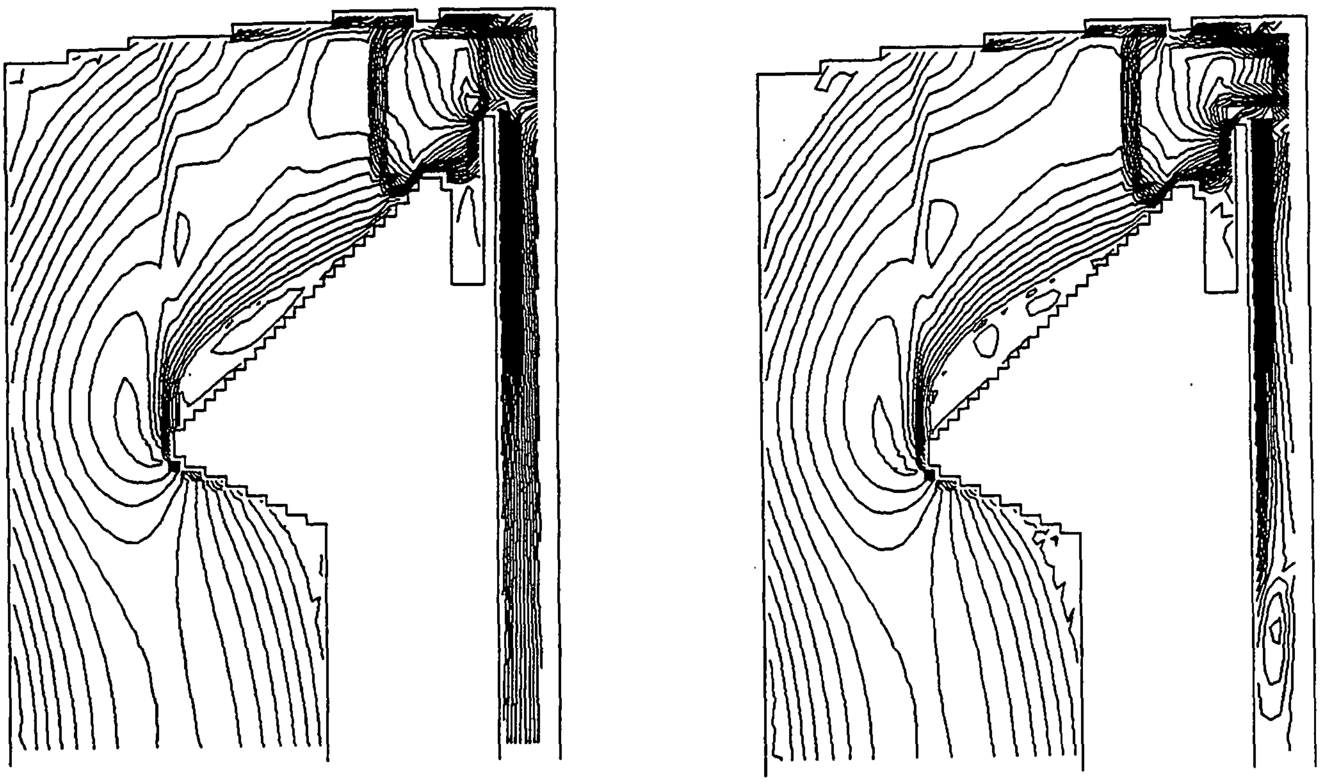

a) k-ε Turbulence Model

b) ASM Turbulence Model

Figure 7. Velocity Magnitude Contours for Two Turbulence Models

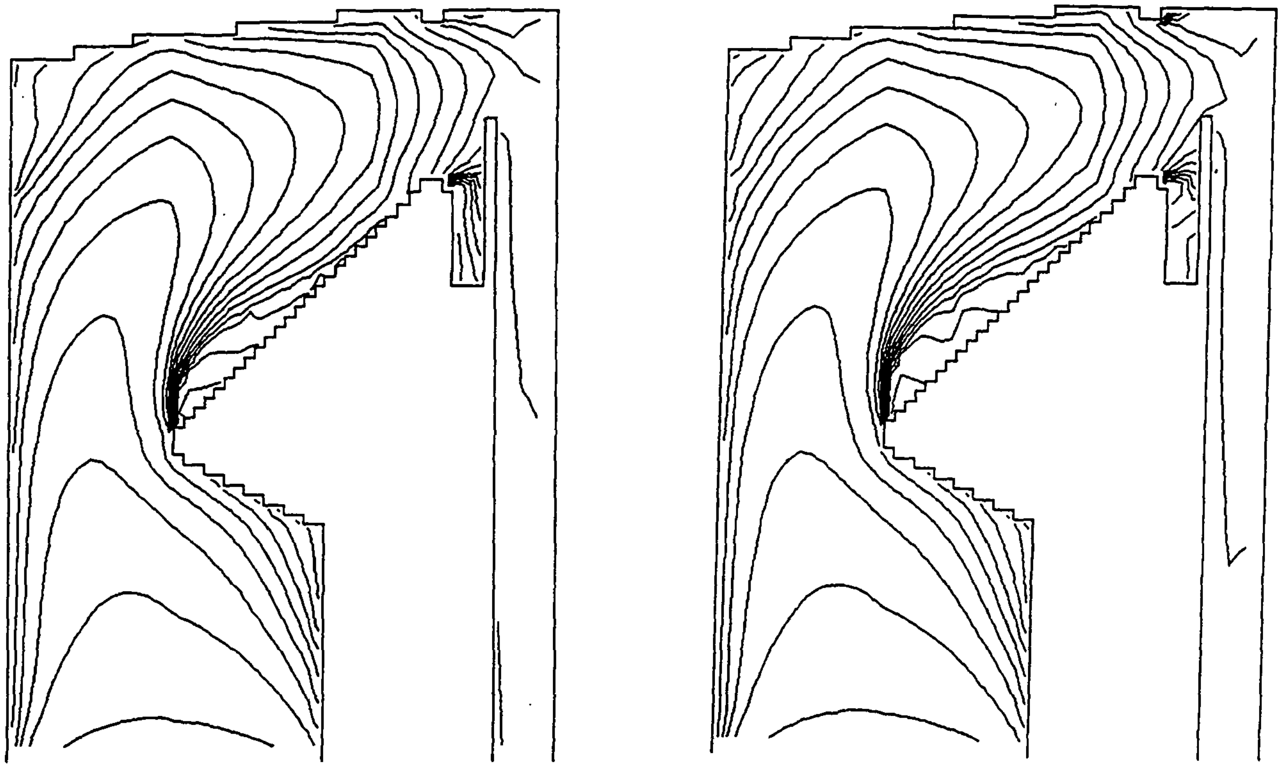

a) k-ϵTurbulence Model

b) ASM Turbulence Model

Figure 8. Temperature Contours for Two Turbulence Models

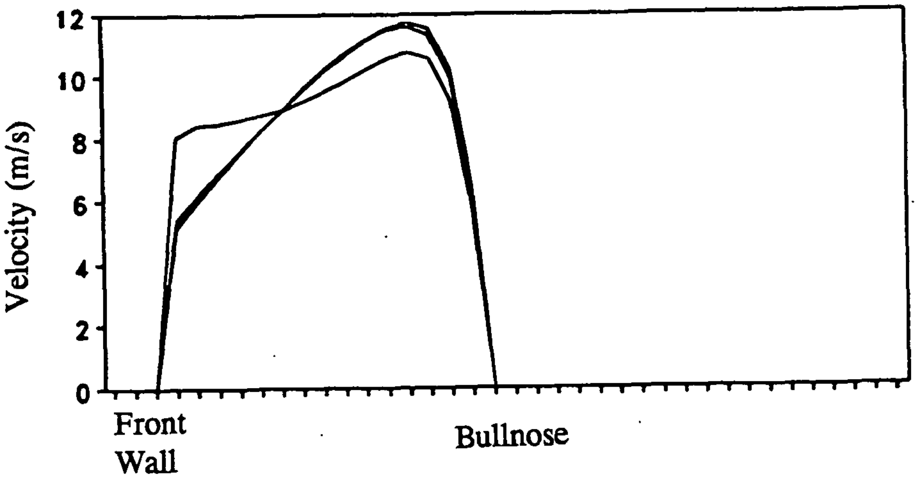

a) Velocity Profiles at the Bullnose

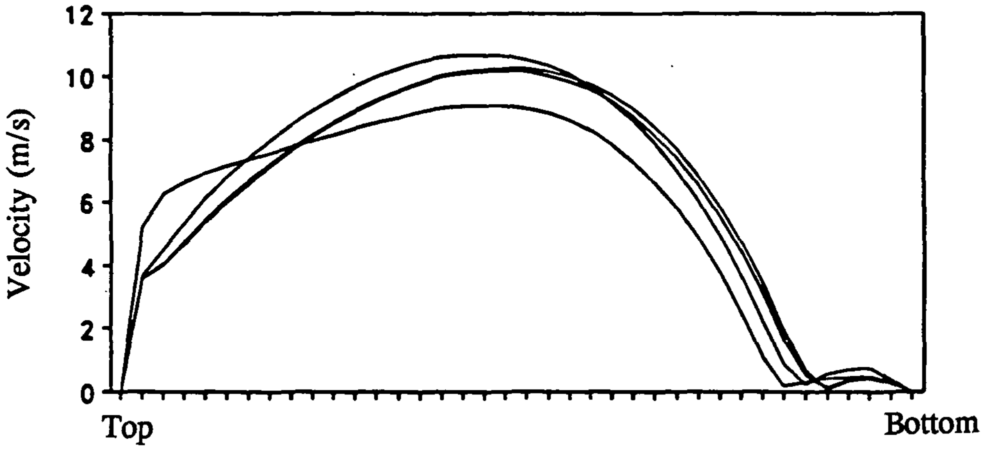

b) Velocity Profiles at the First Superheater Section

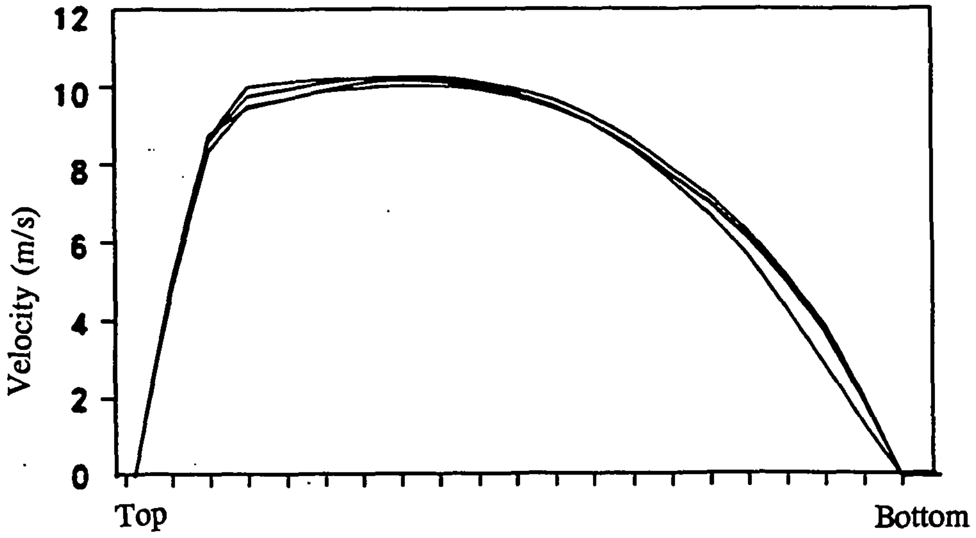

c) Velocity Profiles at the Boiler Bank

Figure 9. Velocity Profiles for Four Cases at Three Locations

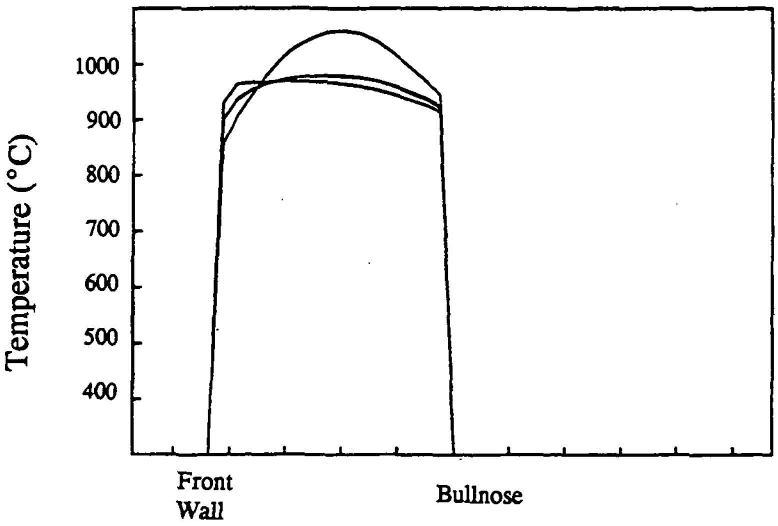

a) Temperature Profiles at the Bullnose

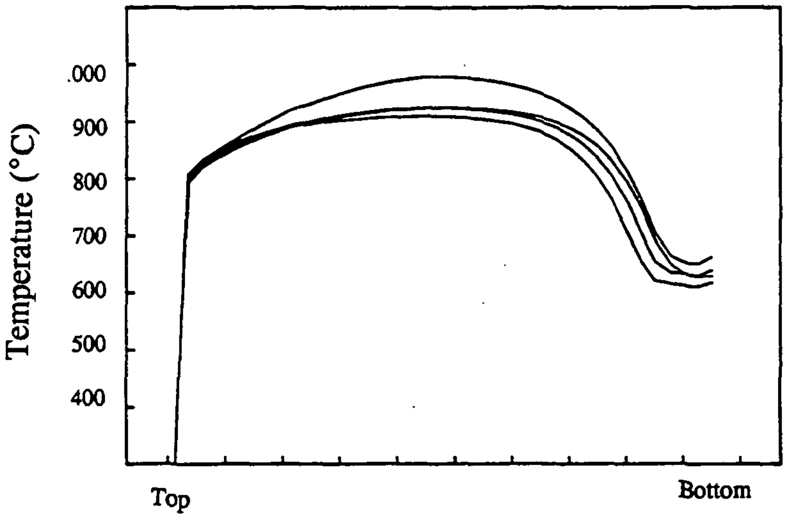

b) Temperature Profiles at the First Superheater Section

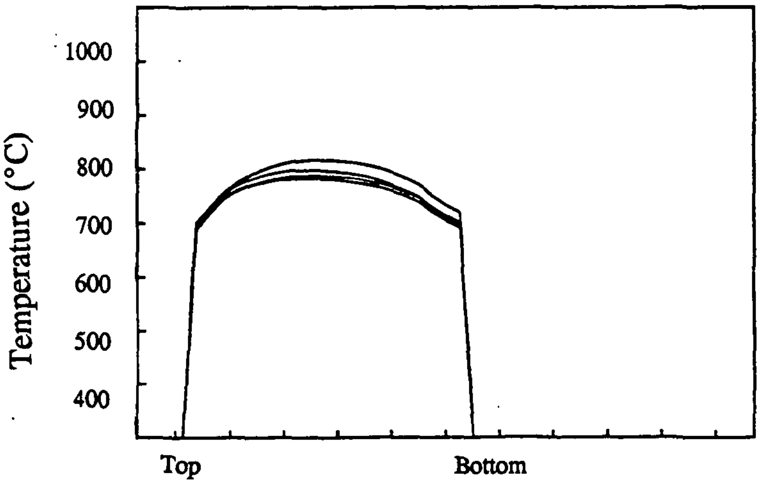

c) Temperature Profiles at the Boiler Bank

Figure 10. Temperature Profiles for Four Cases at Three Locations

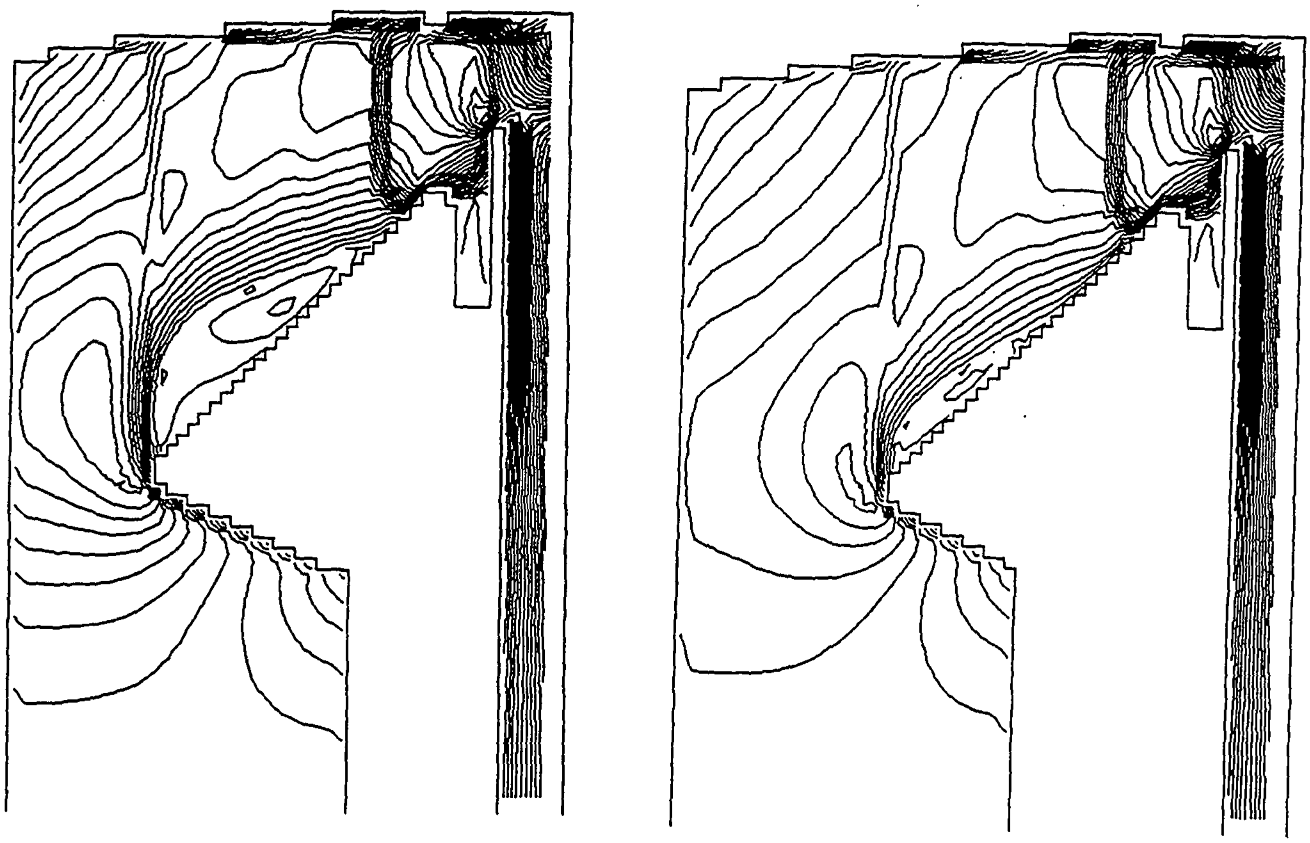

a) Velocity Contours for Large Bullnose

(42% Open Flow Area)

b) Velocity Contours for Small Bullnose

(62% Open Flow Area)

Figure 11. Velocity Contours for Large and Small Bullnose Sizes

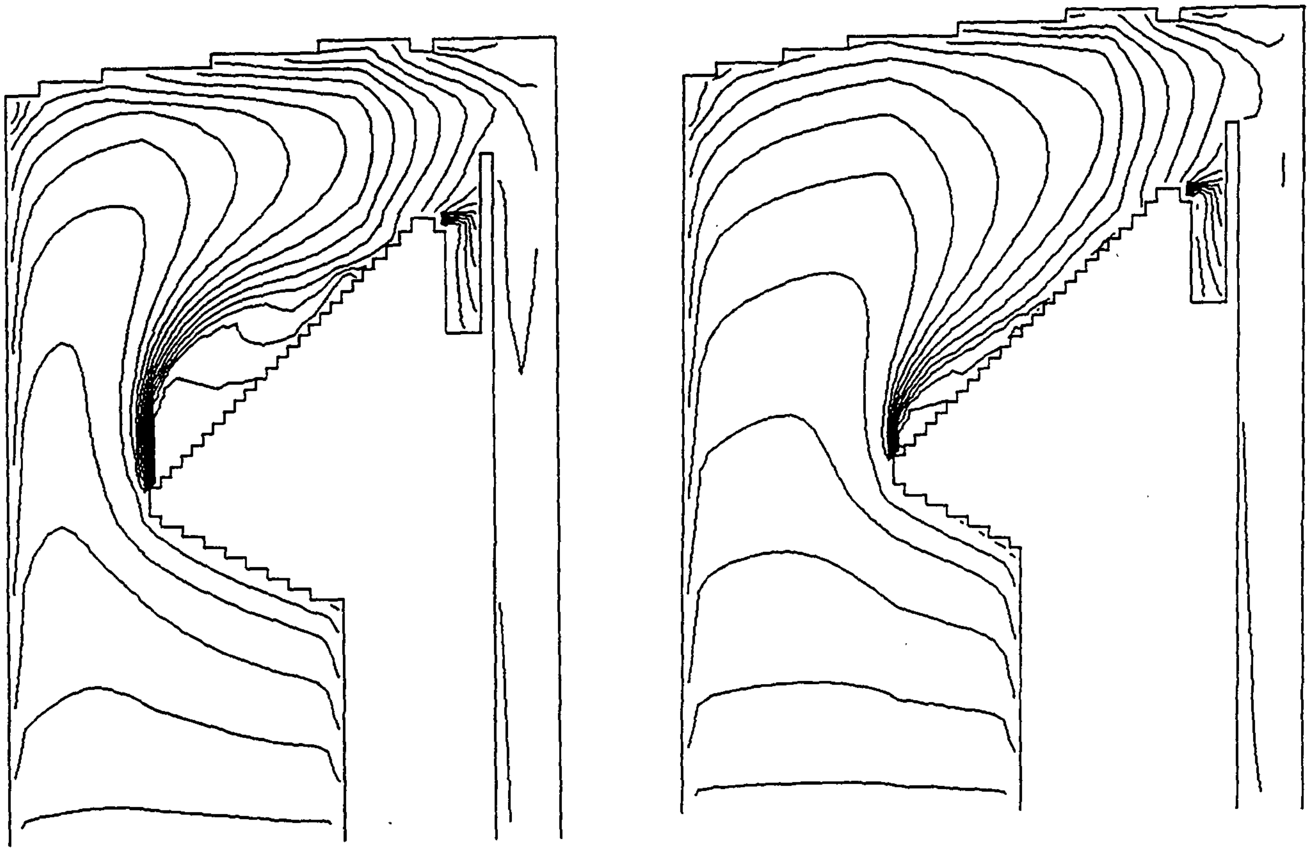

a) Temperature Contours for Large Bullnose

(42% Open Flow Area)

b) Temperature Contours for Small Bullnose

(62% Open Flow Area)

Figure 12. Temperature Contours for Large and Small Bullnose Sizes

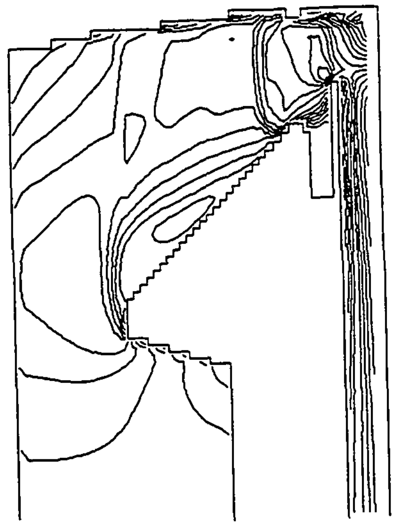

a) Velocity Contours for an Abrupt Bullnose

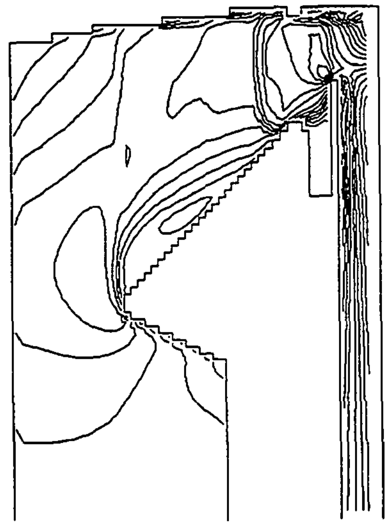

b) Velocity Contours for an Intermediate Bullnose

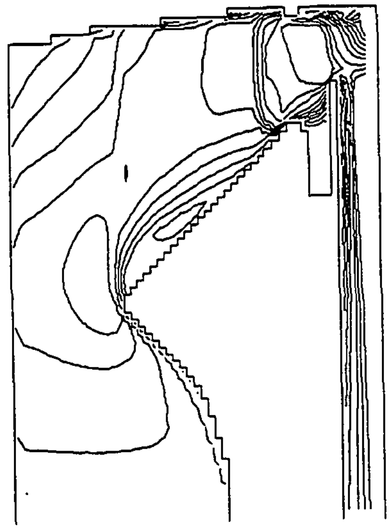

c) Velocity Contours for a Sloping Bullnose

Figure 13. Velocity Contours for Three Bullnose Shapes

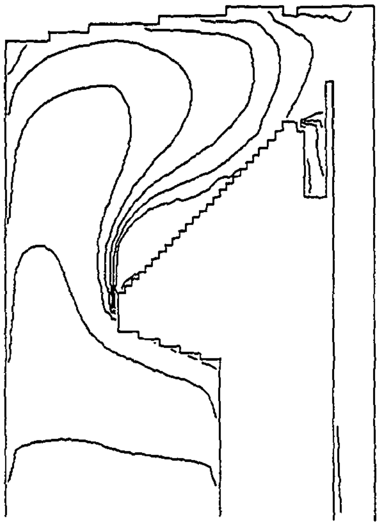

a) Temperature Contours for an Abrupt Bullnose

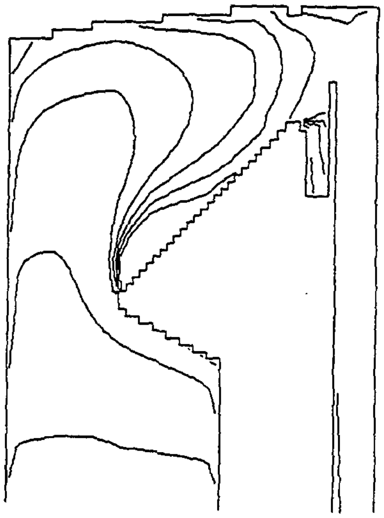

b) Temperature Contours for an Intermediate Bullnose

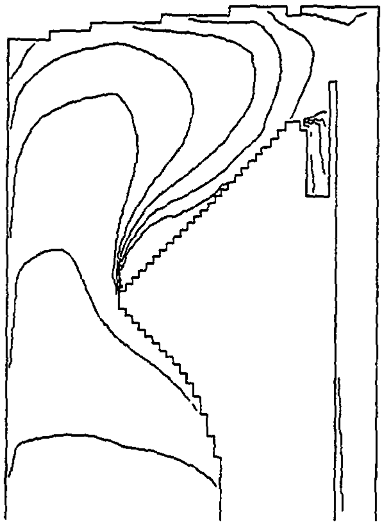

c) Temperature Contours for a Sloping Bullnose

Figure 14. Temperature Contours for Three Bullnose Shapes

REFERENCES

1. Tran, H.N., "How Recovery Boilers Become Plugged", TAPPI Kraft Rec. Op. Seminar, Orlando, FL, Jan., 1992.

2. Reeve, D.W., Tran, H.N. and Barham, D., Pulp & Paper Canada, 82(9):T315-T320 (1981).

3. Tran, H.N., TAPPI J. 69(11):102 (1981).

4. Backman, R., Hupa, M. and Uppstu, E., TAPPI J. 70(6):123-127 (1987).

5. Tran, H.N., Barham, D. and Reeve, D.W., TAPPI J. 71(4):109 (1988).

6. Vakkilainen, E.K., Nikkanen, S., Hautamaa, J. and Anttonen, T., "Flows in the Upper Region of Recovery Boilers", AIChE Annual Mtg., Los Angeles, Nov., 1991.

7. Haynes, J.B., Adams, T.N. and Edwards, L.L., TAPPI J. 71(9):81 (1988).

8. Chapman, P.J., Janik, S.G. and Jones, A.K., Tappi Eng. Conf. Proc., Nashville, Sept. 1991.

9. Grace, T., Walsh, A., Jones, A., Sumnicht, D. and Farrington, T., "Three-Dimensional Mathematical Model of the Kraft Recovery Furnace", CPPA/TAPPI Int. Chem. Rec. Conf., Ottawa, April 1989.

10. Walsh, A.R., "A Computer Model for In-Flight Black Liquor Combustion in a Kraft Recovery Furnace", Ph.D. Thesis, IPC, Jan., 1989.

11. Jones, A.K., "A Model of the Kraft Recovery Furnace", Ph.D. Thesis, IPC, Jan., 1989.

12. Sumnicht, D.W., "A Computer Model of a Kraft Char Bed", Ph.D. Thesis, IPC, Apr., 1989.

13. Karvinen, R., Hyoty, P. and Siiskonen, P., Tappi J. 74(12):171-177 (1991).

14. Chapman, P.J. and Jones, A.K., Tappi J. 75(3):133-137 (1992).

15. Salcudean, M., Gartshore, I., Abdullah, Z., Nowak, P., Aghdasi, F., Quick, J. and Tse D. Annual Report to U.S. DOE for Contract No. DE-FG02-90CE40936, Sept., 1991.

PROGRESS ON THE COMBUSTION/FLOW INTERACTION TASK

Robert R. Horton, Terry N. Adams, and Thomas M. Grace

PROGRESS ON THE COMBUSTION/FLOW INTERACTION TASK

(R.R. Horton, T.N. Adams, T.M. Grace)

The 3-D fixed-flow-field combustion model has been completed and an initial study of black liquor sprays has been carried out. The fixed-flow-field makes use of gas flow velocity fields generated by the Fluent CFD Code for isothermal, non-reacting recovery furnace flow. The particular care examined was for an idealized recovery furnace geometry incorporating: (1) a 1.8 m high char bed, (2) a four-wall primary air slot, (3) a four-wall and, (4) a two-wall tertiary with four air nozzles on both the front and back walls. This geometry was not intended to simulate a specific recovery furnace, but to provide general flow patterns which include channeled flow, localized high-velocity air jets, and multiple recirculation zones. The gas flow velocities at each location from the CFD simulation were transferred to the fixed-field model and used along with the IPST spray nozzle model and the complete black liquor droplet combustion model. The complete fixed-field model was exercised through a range of input parameters in order to examine the impact of spray parameters on the pattern of combustion and carryover in a recovery furnace for this one gas flow pattern.

Extensive parameter sensitivity studies for both the combustion model and the spray model must be carried out before complete interpretation of the initial results are possible. However, some initial insights can be drawn from this study. First, the drying stage of black liquor combustion occurs in a narrow region very near the liquor gun level. This will result in a localized heat sink at this elevation. Second, most of the release of the combustible volatiles from in-flight droplet combustion will occur in a region between the secondary air level and the tertiary air level. High intensity mixing necessary for rapid combustion occurs only in the immediate vicinity of the air jets. Release of volatiles between the two air levels will slow down release. Third, there are at least two clearly identifiable pathways for recovery furnace carryover. The first pathway is for immediate entrainment of small black liquor droplets. This results in smelt bead carryover. The second pathway is for entrainment of intermediate sized black liquor droplets during the devolatilization and swelling stage. This results in carryover of both smelt and char particles.

PROGRESS ON THE CONVECTIVE SECTION PLUGGING TASK

Terry N. Adams and Robert R. Horton

PROGRESS ON THE CONVECTIVE SECTION PLUGGING TASK

(T.N. Adams, R.R. Horton)

Work has been completed on the prediction of the gas velocity and temperature fields in the convective section of a recovery boiler. A commercially available CFD code has been used to model a three dimensional slice of the region of a recovery boiler beginning about 10 feet below the bullnose elevation and extending to the outlet of the first pass of a long flow economizer. The side-to-side depth of this slice was twice the superheater platen spacing, taking in two superheater platens, the gas lane between them and half a lane on either side of them. The superheater platens and the boiler bank were modeled as internal wall elements with prescribed surface temperatures.

The inlet flow conditions to this region in the upper furnace of the recovery boiler depend on the complex and only partially understood flow from the lower furnace. In the present work the inlet flow conditions to the upper furnace were prescribed either as uniform or as strongly peaked parabolic flow profiles. Predicted results for these two assumed inlet profile conditions were compared in order to determine the sensitivity of the results to uncertainties in inlet condition. Only a small sensitivity was found. This is consistent with estimations of flow profile sensitivity to inlet conditions based on a comparison of the dynamic head of the furnace upward gas flow to the dynamic head at the bullnose and to the static pressure drop across the superheater section.

The effect of the turbulence model on flow profile predictions was also examined. The results predicted using the familiar κ-ϵ turbulence model were compared to the alternative, more complex Algebraic Stress Model available in the flow profiles predicted with these two turbulence models. For all of the subsequent cases examined the κ-ϵ turbulence model was used because the CFD solution converged approximately ten times faster with this model.

The initial effort on convective section flow and temperature profiles examined the influence of bullnose size and shape. The bullnose size was specified in terms of the horizontal open flow area at the bullnose relative to the plan area of the furnace. Three sizes were examined: 42% (large bullnose), 52%, and 62% (small bullnose). Three bullnose shapes were also examined. The bullnose shapes examined here varied only in the angle of the upstream face with respect to the upward furnace gas flow. The three shapes were: a slopping bullnose (upstream face at an angle of ~25° to the gas flow), a 45° bullnose, and an abrupt bullnose (upstream face at ~75°).

Detailed results of this examination of the effect of bullnose size and shape have been documented in a paper prepared for presentation at the International Recovery Conference. The basic conclusion from this work is that bullnose acts like a flow restriction similar to an orifice or nozzle. The maximum gas velocity in the bullnose region for any given gas flow is affected both by bullnose size and shape. Increased bullnose size and increased bullnose abruptness increases gas velocity in the bullnose region. This increased velocity causes greater penetration of the flow into the upper furnace cavity, a larger recirculation zone above the bullnose, and consequently poorer utilization of the superheater heat transfer surface.

CHAR GASIFICATION

Stacy R. Lee (IPST Ph.D. Candidate)
and
Kenneth M. Nichols

CHAR GASIFICATION (S. Lee, K. Nichols)

SUMMARY

The CO_2 gasification rate of kraft black liquor char has been measured using a fixed bed reactor at temperatures of 600°C, 700°C, and 800°C. The rate and the activation energy (E_A = 48 kcal/gmol) compare well to rates and activation energies reported previously from thermogravimetric measurements of kraft char gasification. Mass transfer limitations on the observed rate were determined to be negligible by changing both carrier gas and flowrates. Application of the rate derived from the fixed bed reactor to a recovery furnace char bed at typical operating conditions predicts that the rate of CO_2 gasification on the recovery furnace bed is mass transfer controlled at temperatures of 770 °C or greater.

INTRODUCTION

Strong black liquor burns in air in three stages known as drying, devolatilization, and char burning (1,2). Drying involves the evaporation of most of the water present in black liquor. During devolatilization the organic compounds in black liquor solids are thermally degraded to yield combustible gases and residual char. This char is a black, porous, and friable material consisting primarily of organic carbon and the inorganic salts Na_2CO_3, Na_2SO_4, and Na_2S. Approximately one-half of the carbon and most of the sodium contained in the incoming black liquor are found in the char (3).

Char burning consists of heterogeneous reactions that can occur either in-flight or on the char bed, in which the residual carbon is oxidized to CO and CO_2. The primary source of oxygen is O_2 in the combustion air. The O_2 depletes the carbon in the char through direct oxidation and through the sulfate/sulfide cycle (1,4). However, Blackwell and King (5) report O_2 concentrations measured immediately above a recovery furnace char bed to be 2 to 4%. These low O_2 concentrations next to the char bed suggest the possibility that other oxidizer species such as CO_2 and H_2O may play an important role in carbon oxidation. The relative importance depends, at least in part, on the rates of CO_2 and H_2O gasification compared to the overall rate of char burning.

In previous studies, Li and van Heiningen (6,7) and Frederick and Hupa (8,9) have used thermogravimetric analysis to study the CO_2 gasification rate of black liquor chars. Rates and temperature dependencies of rates agreed reasonably well among these studies. These investigators found that black liquor char was gasified at a rate much greater (10-20 times greater) than rates which have been reported for gasification of activated carbon or gasification of coal chars impregnated with Na_2CO_3. The reason for this unusually fast rate has been explained as being due to the high loading and the fine distribution of sodium in black liquor chars (6,7).

However, other kraft char CO_2 gasification measurements (10,11) in a fixed bed purge reactor yielded rates which were slower than those reported in the thermogravimetric studies. A primary goal of this work has been to provide independent CO_2 gasification rate data, using experimental techniques other than thermogravimetry.

REVIEW OF PAST PROJECT ACTIVITY

Five industrial liquors, four kraft black liquors and one soda liquor, were obtained for making chars. Production of char from these liquors was accomplished by using the DOE flow reactor. This involved injecting black liquor droplets downward into the long vertical tube-furnace with pre-heated air flowing upward. The falling liquor droplets were dried and pyrolyzed. The resulting char particles were collected on a bed at the bottom of the tube-furnace. The char bed was continuously quenched with N_2 gas to prevent occurrence of heterogeneous char burning reactions.

DISCUSSION OF 1991 RESULTS

Experimental Procedure

Rate data were obtained with char made from black liquor received from a southeastern U.S. kraft mill pulping a mixture of hardwood and softwood. Partially pyrolyzed char particles were formed using the drop tube furnace as described above. The drop tube furnace temperature was approximately 950°C, the initial black liquor droplet diameter was 2 mm, the particle retention time was approximately 2 seconds, and the mean char particle diameter was 7.7 mm. The partially pyrolyzed particles were fully pyrolyzed by further heating in the cylindrical fixed bed reactor (7.1 cm diameter by 15.2 cm depth) shown in Fig. 1. This was accomplished at atmospheric pressure with a mixture of 95% N_2/5% CO flowing through the fixed bed at a flowrate of 5.45 slpm. The CO and CO_2 concentrations in the product gases were measured continuously using an infrared analyzer. Pyrolysis was considered to be complete when the CO and CO_2 concentrations in the product gas approached 5% and 0% (the levels of CO and CO_2 in the feed).

The elemental compositions of the resulting chars, shown in Table I, were significantly affected by the pyrolysis temperature used in the fixed bed. For the gasification experiments in this study, the pyrolysis temperature (and hence the char composition) was chosen to be the same as the gasification temperature. This choice of pyrolysis temperature was made primarily for convenience, as gasification of the char was initiated immediately upon completion of pyrolysis.

Gasification was initiated by replacing the CO in the carrier gas with the desired level of CO_2. The product gases were monitored continuously for CO and CO_2 concentrations. Table II contains the ranges of conditions used in the gasification experiments. The reason for using different carrier gas and carrier gas flowrates was to quantify mass transfer effects on the observed rate.

Results

A typical set of CO and CO_2 concentration profiles obtained is shown in Fig. 2. The rate of gasification was determined from the CO_2 concentration profiles according to a method outlined by Smith [12] for a fixed bed in which the solid particles contain one reactant and the second reactant is in the fluid phase. The CO_2 concentration decreased along the reactor length, and this variation of concentration with length was a function of time. Thus, the process did not operate at steady state. For isothermal plug-flow, a mass conservation equation over the fixed bed for CO_2 is written as:

$$-u\, f(\partial(CO_2),\partial z) = r r_{bed} + e_{bed}\, f(\partial(CO_2),\partial t) \qquad (1)$$

where r_{bed} = density of char bed, (kg organic C/m^3)
r = global rate of disappearance of CO_2 per unit volume of reactor, ($gmol/m^3/s$)
u = superficial velocity in the direction of flow, (m/s)
e_{bed} = void fraction of char bed,
z = axial position in the char bed, m
t = time, s

Assuming a global rate for CO_2 gasification of char (i.e., $r = k(C_{CO2})^n$), Eq. 1 was integrated and fit to the concentration data (such as that in Fig. 2) to give the rate constant. The best fit for the reaction order was approximately 1.0, indicating the reaction is first order dependent on CO_2 concentration.

Rate constants for the 600°C, 700°C, and 800°C data are shown in Fig. 3. The slope (or activation energy) between 700 and 800°C is less than the slope between 600 and 700°C, suggesting that mass transfer limitations may have been affecting the observed rate. To test for film mass transfer effects, experiments were performed using different gas velocities. To test for pore diffusion effects, experiments were completed using He as the carrier gas and compared to the results where N_2 was the carier gas. The resulting average rate constants were approximately the same indicating that neither film nor pore diffusion effects were appreciable. In addition, the average film mass transfer coefficient was calculated using a standard correlation to be 7.1 $m^3/kg/s$ at 800 °C, which is more than an order of magnitude greater than the observed rate constant. Consequently, film mass transfer and pore diffusion limitations in the fixed bed reactor were considered negligible.

Oxygen material balances suggest that take-up of oxygen by the char bed is a plausible explanation for the lower than expected rate constant values at 800°C. Assuming that the only reaction occurring was $\text{Char-C} + CO_2 \dashrightarrow 2CO$, the mass flow rate of oxygen entering as CO_2 should equal the mass flow rate of oxygen leaving as CO and CO_2. The ratio of oxygen out to oxygen in was very near unity (0.98 ± 0.03) for the 600°C and 700°C data; while the average ratio for 800°C experiments was 0.85. This suggests that approximately 15% of the oxygen was consumed by competing reactions during the high temperature experiments.

This explanation is supported by two observations which were unique to the 800°C tests: (1) the formation of smelt, and (2) corrosion of the reactor walls. After the 800°C experiments, beads of frozen smelt were found attached to the stainless steel walls of the reaction chamber. Where smelt was present, it was possible for CO_2 to react with inorganics in the smelt. For example, the Na_2S in the char would react with CO_2 to form Na_2SO_4. Measurements were made of the sulfur in the smelt. By assuming that the sulphur in the frozen smelt was present as Na_2SO_4, material balances showed that 9.6-11% of the oxygen was used to produce Na_2SO_4.

The second observation, corrosion of the stainless steel reactor walls, was quantified by weighing the reaction chamber walls after each experiment. Assuming that the weight loss was primarily Cr_2O_3, it was determined that 2.0-6.5% of the oxygen appeared in the Cr_2O_3.

Thus, smelt reactions and corrosion reactions can account for the discrepancies in oxygen material balances for the 800°C tests. This supports the conclusion that mass transfer was not limiting the observed rate; and thus it seems justifiable to use the slope between 600 and 700°C (in Fig. 3) as the true activation energy for CO_2 char gasification.

COMPARISON TO PREVIOUSLY REPORTED RESULTS

Table III summarizes the rates, activation energies, and conditions of all the available char gasification experiments, including those measured in this study. The similarities in rates and activation energies are significant considering the differences in char quantity, liquors used to produce the chars, the char production process, and the differences in the experimental reactors. The rates of this study are somewhat greater than the others reported, though differing by less than one order of magnitude from all others except the rates reported by Goerg and Cameron [10,11]. Most of these differences are likely explained by differences in chars and char production methods.

The rates reported by Goerg and Cameron [10,11] may be exceptionally low due to the unique method employed: they used a mixture of char and Na_2CO_3; whereas, char was the only solid reactant used in other studies. Goerg and Cameron heated the char-Na_2CO_3 mixture to reaction temperature in an atmosphere of N_2 gas. Li [13] has suggested that when a char-Na_2CO_3 mixture is heated to gasification temperatures, the Na_2CO_3 will react with organic carbon yielding products such as gaseous Na, CO, and some CO_2. Therefore, the initial organic carbon concentrations for the Goerg and Cameron experiments may have been low or even negligible. Since the rate of gasification is a function of the organic carbon concentration, low carbon concentrations during gasification would have resulted in slower gasification rates than the rates observed in other studies.

Implications for Recovery Furnaces

Having established a kinetic rate expression for CO_2 gasification for the fixed bed reactor, the implication of these results for kraft recovery furnaces were examined. Using the expression for mass transfer coefficient developed by Brown et al. [14] for black liquor char burning, the expression for kinetic rate of CO_2 gasification developed in this study, and the values shown in Table IV for recovery furnace conditions, values of coefficients for both mass transfer and chemical reaction were determined. These values are shown in Table V over ranges of temperatures and velocities found in recovery furnaces. The result is the same for nearly all reasonable combinations of recovery furnace parameters; the mass transfer coefficient is much smaller than the kinetic coefficient. This suggests that mass transfer is always controlling the rate of CO_2 gasification in a recovery furnace. Calculations indicate that the two coefficients take on equivalent values at a temperature of approximately 770°C.

CONCLUSIONS

The CO_2 gasification rate of kraft black liquor char was studied using a fixed bed reactor at temperatures of 600°C, 700°C, and 800°C. Experiments using different gas velocities and different carrier gases (N_2 or He) showed that neither film mass transfer effects nor pore diffusion significantly affected the observed rate.

The rate of CO_2 gasification and the activation energy (E_A= 48 kcal/gmol) compare well to rates and activation energies reported for previous thermogravimetric investigations. These similarities in rates and activation energies are significant considering the differences in char quantity, liquors used to produce the chars, the char production processes, and the experimental reactors.

Having established the CO_2 gasification rate for the fixed bed reactor, the implication of these results for kraft recovery furnaces is, that for most conditions in the recovery furnace the rate of CO_2 gasification is expected to be mass transfer limited rather than kinetically controlled.

FUTURE ACTIVITY

Future work will address H_2O gasification rates, and the subject of parallel reactions. Since CO_2 and H_2O are products of combustion reactions, and are also reactants in gasification reactions, it is not clear that the overall rate due to both (combustion and gasification) is as great as the sum of the independently determined rates.

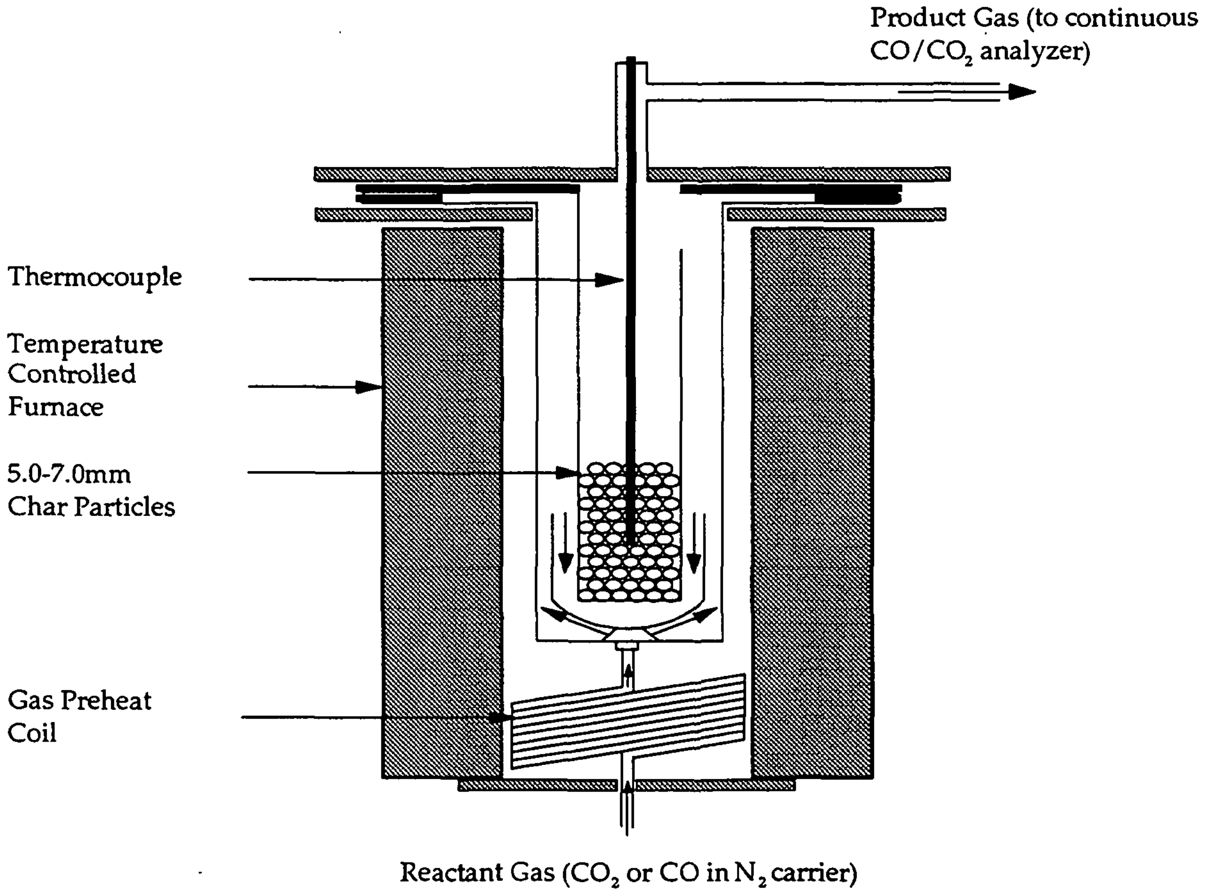

FIGURE 1: Schematic of the Fixed Bed Reactor Used for CO$_2$ Gasification of Black Liquor Char

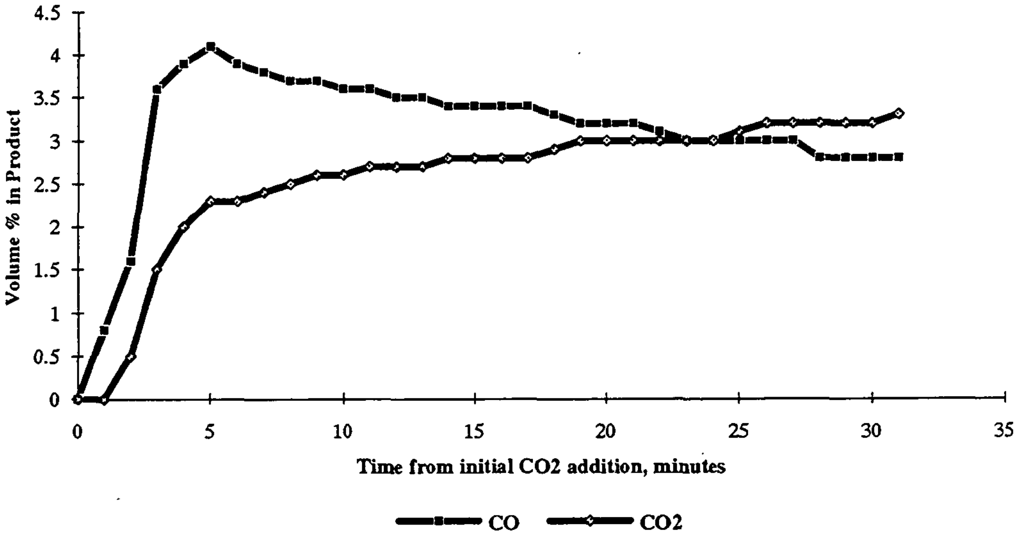

FIGURE 2: %CO and %CO_2 in Product Gas as a Function of Time for a Typical Gasification Experiment (702°C, 4.3% CO_2, 5.32 slpm total gas flow, N_2 Carrier Gas)

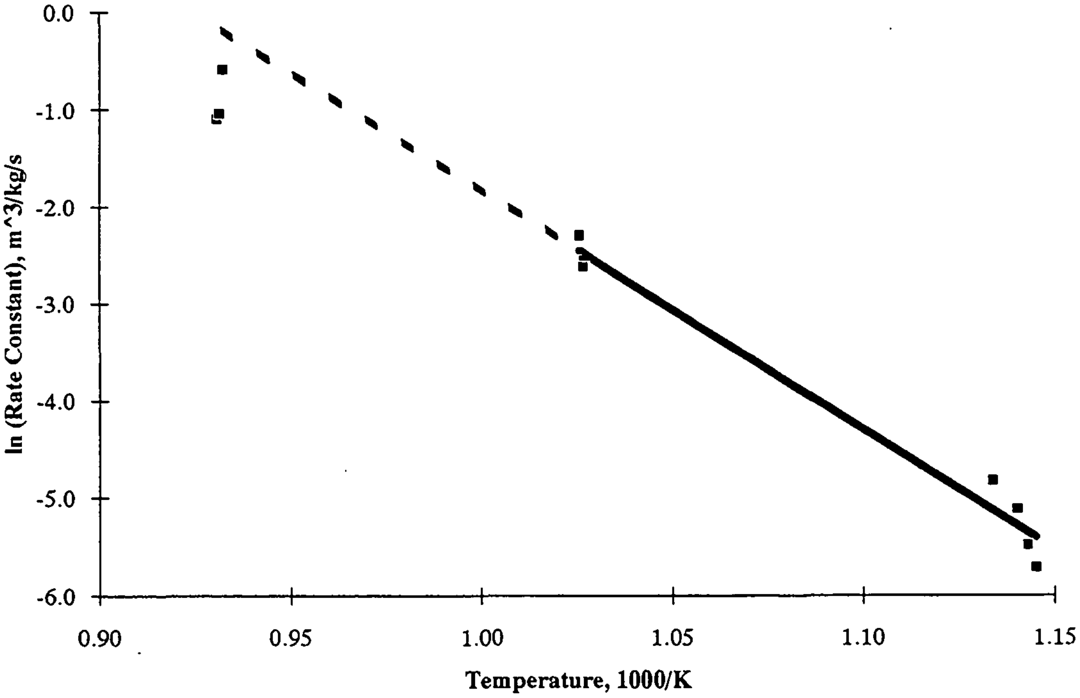

FIGURE 3: Arrhenius Plot for Data at 600°C, 700°C, and 800°C.

Table I: Composition (Weight %) of BLC used in Fixed Bed Reactor Experiments

	Pyrolysis Temperature		
Element	600°C	700°C	800°C
C	34.1	28.2	25.3
H	1.35	0.86	0.48
O	30.5	28.6	31.8
Na	25.2	27.4	26.1
S	3.75	4.23	5.54
Carbonate C	5.11	6.63	6.62
Sulfate S	1.74	1.32	2.21
Thiosulfate	0.22	0.63	0.22

Table II: Range of Conditions in the Fixed Bed Reactor Experiments

Parameter	Value
Temperature	600°C, 700°C, 800°C
Pressure	1 atmosphere
CO_2 Concentration	4.3%-10.1%
Carrier Gases	He, N_2
Gas Flow Rate	5.32 slpm, 10.10 slpm
Char Mass	10-15g

Table III: Comparison of CO_2 Gasification Rates

Rate @ 700°C (hr^{-1})	E_A (kcal/mol)	Temp. Range (°C)	Gas Pressure, (atm.)	Gas Composition, % $CO_2/CO/N_2$	Exp. Method	Char Mass, (g)	Investigator
1.9	44.4	700-900	1	20/4/76	PTG*	~0.1	Frederick& Hupa [9]
0.9	49	650-800	20	20/4/76	PTG	~0.1	Frederick & Hupa [10]
3.0-4.8	60	675-775	1	20/10/70	TGA**	~0.005	Li & van Heiningen [8]
1.1	44.7	700-775	1	20/10/70	TGA	~0.005	Li & van Heiningen [7]
0.06	46.8	927-1010	1	5/5/90	Purged Bed	1	Goerg & Cameron [11,12]
1.7	48.9	600-800	1	4.4/0/95.6	Fixed Bed	10-15	Present Study

*PTG=Pressurized Thermogravimetric

**TGA=Thermogravimetric Analysis

Table IV: Typical Furnace Conditions Used in the Application of Derived CO_2 Rate to Recovery Furnaces

Parameter	Assumed Value
Hearth Loading [17]	0.21 kg/sm^2
Boiler Cross Sectional Area [2]	100 m^2 (10mx10m)
Air Requirement	6 kg Air/kg Black Liquor Solids
Primary Air Distribution [18]	45% of Total Air Requirement
Primary Air Into One Wall	25% of Total Primary Air
Channel of Air Flow	6.67 m^2 (10mx667m)
Density of Air	0.28 kg/m^3
Density of Char	7.79 kgC/m^3
Acitve Burning Layer [16]	5 cm

Table V: The Influence of Recovery Furnace Parameters on Mass Transfer and Kinetic Rate Constants

Parameter	Low	Typical	High
Temperature (K/°F)	1030/1400	1250/1800	1480/2200
Velocity Range (m/s)	0.5	10	65
Active Char Layer (cm)	3	6	10
Kinetic Coeff. (m^3/kgC/s)	0.2	13.6	290
Mass Transfer Coeff. (m^3/kgC/s)	0.05	0.2	1.39

REFERENCES

1. Grace, T.M.; Cameron, J.H.; and Clay, D.T. Role of the Sulfate-Sulfide Cycle in Char Burning: Experimental Results and Implications. TAPPI 69(10): 108-113 (1986).

2. Adams, T.N.; Frederick, W.J. Kraft Recovery Boiler-Physical and Chemical Process, New York: The American Paper Institute (1988).

3. Grace, T.M.; Cameron, J.H.; and Clay, D.T. Char-Burning Project 3473-6, American Paper Institute (February 22, 1985).

4. Cameron, J.H.; Grace, T.M. Kinetic Study of Sulfate Reduction with Carbon. Ind. Eng. Chem. Fundam. 22(4): 486-494 (1983).

5. Blackwell, B.; King, T. Chemical Reactions in Kraft Recovery Boilers, Vancouver: Sandwell and Company Limited, (1985).

6. Li, J.; van Heiningen, A.R.P. Reaction Kinetics of Gasification of Black Liquor Char. The Canadian Journal of Chemical Engineering 67(8): 693-697 (1989).

7. Li, J.; van Heiningen, A.R.P. Kinetics of CO_2 Gasification of Fast Pyrolysis Black Liquor Char. Ind. Eng. Chem. Res., 29(9): 1776-1785 (1990).

8. Frederick, W.J.; Hupa, M. Gasification of Black Liquor Char with CO_2 at Elevated Pressures. TAPPI 74(7): 177-184 (1991).

9. Frederick, W.J.; Hupa, M. Gasification of Black Liquor at Elevated Pressures Part 2. Rate Data with CO_2 and Water Vapor. Report 90-12, Combustion Chemistry Research Group, Abo Akademi, Turku, Finland (1990).

10. Goerg, K.A.; Cameron, J.H. A Kinetic Study of Kraft Char Gasification with CO_2. AICHE Meeting. (Boston). Preprint no. 67g: (Aug. 24-27, 1986).

11. Goerg, K.A. The Gasification of Kraft Char with Carbon Dioxide. M.S. Dissertation. Appleton, WI, The Institute of Paper Chemistry, .

12. Smith, J.M. Chemical Engineering Kinetics, New York: McGraw-Hill Book Company, pp. 394-397 and 655-658 (1981).

13. Li, J. Pyrolysis and CO_2 Gasification of Black Liquor Char. M. Eng. Thesis. Montreal, McGill Univ., Feb., 1986.

14. Brown, C.A.; Grace, T.M.; and Clay, D.T. Char Bed Burning Rates-Experimental Results. 1989 International Chemical Recovery Conference: 65-73 (April 3-6, 1989).

NO$_x$ EMISSIONS FROM BLACK LIQUOR COMBUSTION

Kenneth M. Nichols,
Laura Thompson (IPST Ph.D. Candidate),
and
H. Jeff Empie

NO_x EMISSIONS FROM BLACK LIQUOR COMBUSTION (K. Nichols, L. Thompson, J. Empie)

SUMMARY

A review of NO_x formation studies shows that NO forms in recovery furnaces primarily by two independent mechanisms; thermal, and fuel. Thermal NO formation is extremely temperature sensitive; theoretical predictions show the potential for thermal NO to increase dramatically with moderate increases in recovery furnace temperature. Fuel NO formation is relatively temperature insensitive, and is related to fuel nitrogen content.

Based on theoretical predictions, it seems unlikely that temperatures in recovery furnaces are sufficiently high enough to result in significant thermal NO concentrations. Black liquors are shown to contain 0.05 to 0.24 weight percent fuel nitrogen. Conversion of just 20% of this would yield approximately 25-120 ppm NO (at 8% O_2) in the flue gas, enough to represent the majority of the total NO. Data from operating recovery furnaces show NO_x emissions ranging from near zero to over 100 ppm (@ 8% O_2); much lower than emissions from coal, oil, and gas combustion. An apparent increase in recovery furnace NO_x emissions was observed with increasing solids. This increase is much less than predicted by thermal NO formation theory, indicating that other NO formation/destruction mechanisms are important.

INTRODUCTION

Nitric oxide (NO) and nitrogen dioxide (NO_2) are formed during combustion whenever nitrogen is present in the fuel or in the combustion air. These oxides of nitrogen (collectively referred to as NO_x) are considered to be key constituents in reactions associated with photochemical smog and acid rain (1). For these reasons NO_x emissions from stationary combustion sources have been regulated by local and federal agencies.

Traditionally, recovery furnaces have been operated such that NO_x emission levels were well below typical emission standards. Surveys of NO_x emissions from kraft recovery furnaces in the late 70's (2,3) showed emissions in the range 0.05 to 0.14 pounds per million BTU (26 to 71 ppm on an in-stack concentration basis). At the same time, the emissions standard for oil-fired steam generators was 0.30 pounds NO_x per million BTU.

More recently, due to improved technologies for concentrating black liquors, recovery furnaces are operating at higher levels of liquor solids concentration. Decreases in liquor moisture will result in higher combustion temperatures, and there is some concern that increased temperatures will yield increases in NO_x emissions. In several cases, observed increases in recovery furnace NO_x emissions have been related to firing higher solids concentrations (4-7).

REVIEW OF PAST PROJECT ACTIVITY

This is a new project, with no significant activity prior to the Jan, '91 Jan, '92 time period.

DISCUSSION OF 1991 RESULTS

Most of the NO_x emitted by combustion sources is NO with only a small fraction (typically 5% or less) appearing as NO_2. The total NO emitted is formed by three independent mechanisms: thermal NO (the fixation of molecular nitrogen by oxygen atoms produced at high temperatures), fuel NO (the oxidation of nitrogen contained in the fuel during the combustion process), and prompt NO (the attack of hydrocarbon free radicals on molecular nitrogen producing NO precursors). Prompt NO is usually considered to be of minor importance for industrial furnaces (8), although it could potentially be important in recovery furnaces where total levels of NO are comparatively low. The relative importance of each of the other two mechanisms in determining the total NO emission level is dependent on furnace temperatures and fuel nitrogen levels.

Thermal NO

Thermal NO is the dominant source of NO emissions for combustion of fuels such as natural gas which contain very low levels of chemically bound nitrogen. The mechanism for the formation of thermal NO was first described by Zeldovich(9) in 1946 as the two reaction steps

$$N_2 + O \longleftrightarrow NO + N \qquad (1)$$
$$N + O_2 \longleftrightarrow NO + O \qquad (2)$$

The first step (Reaction 1) is rate-limiting and has a very high activation energy (75 kcal/gmol). This high activation energy implies high temperature sensitivity, hence the designation "thermal" NO. The Zeldovich mechanism is frequently extended (8) to more accurately describe thermal NO formation under fuel-rich conditions by including a third reaction step

$$N + OH \longleftrightarrow NO + H \qquad (3)$$

Because thermal NO is formed during the combustion of nearly all fuels, this mechanism has been studied extensively. Kinetic rate coefficients for both the forward and reverse rates (of Reactions 1-3) have been reported over a wide range of temperatures (10). The reactions involve primarily the oxygen-nitrogen system and can be, with reasonable accuracy, considered separately from the combustion process, since the time scale for NO formation reactions is generally greater than the time scale for combustion reactions. This allows the information derived from laboratory combustion studies to be applied to thermal NO formation in industrial furnaces.

From the Zeldovich mechanism (Reactions 1 and 2), a simple expression can be derived to approximate the rate of thermal NO formation. In practical flames, NO concentrations are small compared to O_2 and N_2 concentrations, and the forward rates are greater than the reverse rates. Considering only the forward reactions, and invoking the steady state assumption for atomic nitrogen (i.e., d(N)/dt = 0), the following expression is obtainable

$$f(d(NO),dt) = 2k_1 (O) (N_2) \qquad (4)$$

where k_1 is the rate constant for the forward rate of Reaction 1. By assuming equilibration of the combustion reactions, the concentration of atomic oxygen can be estimated from its equilibrium with O_2 as

$$(O) = 3.01 \text{ x } 10^3 \exp [-30{,}300 /T] (O_2)^{1/2} [P/(RT)]^{1/2} \qquad (5)$$

As shown by Bowman (10), a generally accepted expression for the forward rate constant is

$$k_1 = 1.8 \text{ x } 10^{11} \exp [-38{,}400 /T], \text{ m}^3\text{/kgmol/s} \qquad (6)$$

Substitution of these expressions (Equations 5 and 6) into Equation 4 yields

$$f(d(NO),dt) = f(3.79 \text{ x } 10^{15},T^{1/2}) \exp [-68{,}700 /T] (O_2)^{1/2} (N_2), \text{ kgmol/m}^3\text{/s} (7)$$

where T is gas temperature in Kelvins, t is reaction time in seconds, and all gas concentrations are in units of kgmol/m³. It is evident from this rate expression that thermal NO formation is highly temperature dependent, and is also dependent on oxygen concentration and residence time. This is more clearly illustrated with Figure 1, which is a graphical representation of Equation 7. Figure 1 shows the potential for moderate increases in temperature to have a significant impact on thermal NO formation.
Concentrations of thermal NO increase by an order of magnitude for each 100-140 °F (55-80 °C) increase in furnace temperature. The dependencies on oxygen concentration and residence time are less pronounced than the temperature dependency.

Considering the typical ranges of oxygen concentration and temperature in the lower recovery furnace (indicated by the shaded box in Figure 1) it is clear that essentially all of the thermal NO formation in recovery furnaces must occur in those areas where the highest temperatures exist. This suggests that the region of primary air sweeping across the char bed surface may be the key region (or at least one of the key regions) in the furnace for production of thermal NO.

Caution should be used in employing Figure 1 (or Equation 7) to predict the precise levels of thermal NO in recovery furnaces. This prediction does not account for local temperatures which can be much higher (by 200 °C or more) than average temperatures due to exothermic combustion reactions at burning particle surfaces, and due to turbulent fluctuations. Actual concentrations of oxygen atoms may exceed equilibrium. Mixing in recovery furnaces is imperfect and may lead to local oxidizing and reducing zones. These factors could lead to thermal NO levels in recovery furnaces which are greater than those shown in Figure 1. In

1. Approximate temperature and oxygen dependency of thermal NO, as determined by Equation 7 for residence times of 2 and 3 seconds.

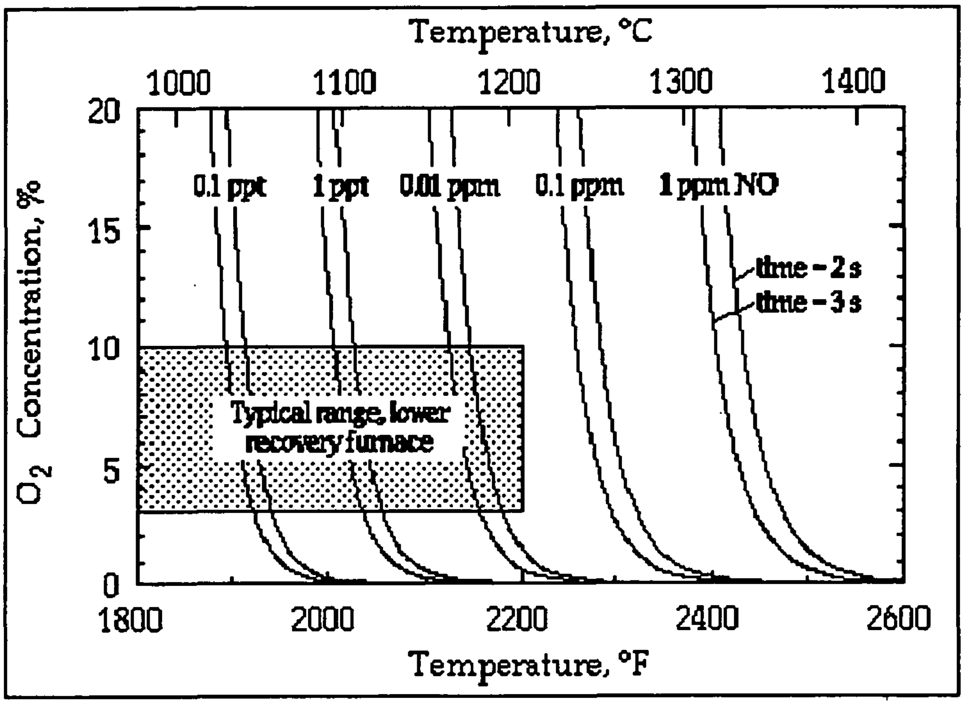

spite of these simplifying assumptions, however, it seems unlikely that temperatures in recovery furnaces are sufficiently high to result in significant thermal NO concentrations.

Figure 1 and Equation 7 also illustrate that strategies for reducing thermal NO formation must bring about reductions in one or more of furnace temperatures, oxygen concentrations, or residence times at high temperature. As discussed by Anderson and Jackson (11), demonstrated strategies include biased firing, off-stoichiometric combustion (or air staging), and low excess air firing.

Fuel NO

Fuel NO is formed during combustion as a result of the oxidation of nitrogen contained in the fuel. A great deal of research has been focused on understanding the elementary steps and reaction mechanisms leading from fuel nitrogen to fuel NO. General reviews of this research are available (12, 13). A large number (hundreds) of reactions are involved, and many of these contain difficult-to-measure intermediates and radical species. Though an exact determination of the complete mechanism is presently not available, it is generally accepted (10, 13-15) that the fuel NO mechanism includes a rapid (not rate limiting) conversion of fuel nitrogen compounds into intermediate nitrogen compounds (HCN, CN, NH_2, NH, N) which can either be converted to NO by attack of oxygen containing species or be converted to N_2 by reaction with NO itself. This is often represented by an overall reaction pathway as

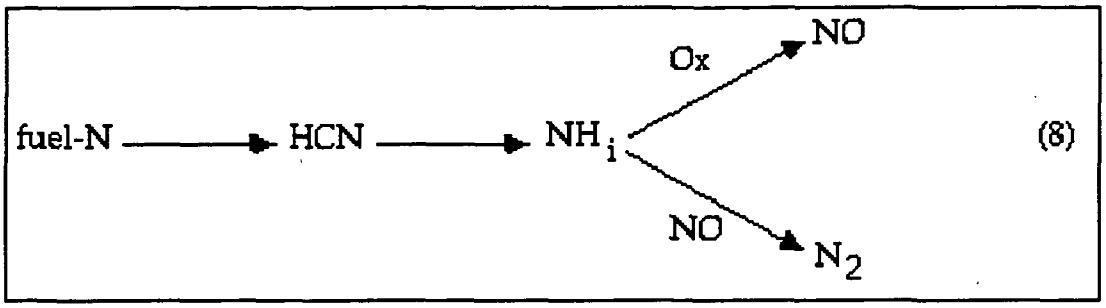

(8)

Overall reaction rates of NO and N_2 formation from fuel nitrogen have been determined for laboratory hydrocarbon flames doped with simple nitrogen compounds such as ammonia, cyanogen, and pyridine (14, 15). These overall reaction rates measured on simpler combustion systems have also been applied with encouraging success for the prediction of fuel NO formation during coal combustion (16).

Factors affecting fuel NO formation are fuel nitrogen content and concentration of oxygen in the gas. Unlike thermal NO, the formation of fuel NO is relatively insensitive to temperature changes caused by changes in air preheat or changes in fuel heating value (17). Increased fuel nitrogen content can lead to higher emissions of fuel NO, although fuel NO cannot be correlated with nitrogen content alone. The relationship between weight percent of nitrogen in fuel, and the percent of fuel nitrogen conversion to NO in practical combustors has been reported for a variety of fossil and synthetic fuels with nitrogen contents up to 2% (1, 10). On average, fractional conversion to NO increases with decreasing nitrogen content. The data, however, are widespread; for example, fuels containing less than 0.2% nitrogen showed conversions to NO ranging from a minimum of 20% to as high as 80%.

There are little to no data showing the fractional conversion of black liquor nitrogen to NO. Researchers investigating nitrogen dioxide pretreatment of pulp (the Prenox process) found that 5% or less of the nitrogen in nitrate added to black liquor was found as NO_x in the recovery boiler flue gases (18). This may not be representative, however, since the inorganic form of the nitrogen bound in nitrate may behave very differently than the chemical forms of nitrogen found in black liquor.

Measurements of nitrogen content for a number of kraft black liquors are shown in Table I. Expressed as a weight percentage of the dry liquor solids, the values are in the range 0.05-0.24 with the average being 0.11. Using the minimum fuel nitrogen to NO conversion value of 20% discussed above, a recovery furnace burning black liquor with the range of nitrogen contents in

I. Nitrogen levels in thirteen kraft black liquors.

Mill	wood	N, % of dry solids
1	mxd	0.05 Canton mxd
2	swd	0.06 Canton 100% pine
3	swd	0.06 Phenix swd
4	mxd	0.06 Newbern
5	swd	0.1 Longview (KK)
6	NA[a]	0.1 Valiant (KK)
7	NA	0.14[b] Thorn A
8	NA	0.05[b] Thorn B
9	NA	0.14[b] Thorn C
10	NA	0.24, 0.20, 0.08[b]
11	NA	0.12, 0.19, 0.10[b]
12	NA	0.1 Esa V
13	NA	0.1 Esa V
Average		0.11
Standard Dev.		0.06

[a] not available

[b] samples collected on different days

Table I would yield NO emission levels of approximately 25-120 ppm in the flue gas (@ 8 % O_2). This estimate suggests that fuel nitrogen is an important source of recovery furnace NO_x.

Additional support for this is provided by residual oil combustion studies (19, 20). Fuel NO was shown to be responsible for greater than 50% of total NO emissions during residual oil combustion at conditions of high air preheat (530 °F) and about 80% of total NO without air preheat (because thermal NO was lower). The residual oil contained 0.20% nitrogen, which is within the range of black liquor nitrogen values shown in Table I.

A question of importance to fuel NO formation is during which stage of combustion the fuel nitrogen is released (or converted) from its chemical form in the fuel to the gas phase intermediates in Equation 8. This will affect when and where in the furnace the reaction of the intermediates will occur, and will affect the distribution of products formed (i.e., NO versus N_2). In combustion of coal, the release of fuel nitrogen occurs primarily during devolatilization, although additional nitrogen release occurs during char combustion (21). Thus, the majority of the coal nitrogen is chemically bound in a manner so as to be readily volatile.

For coals, the rate at which nitrogen is released is normally slightly more rapid (by a factor of 1.2-1.5) than the rate at which carbon is burned from the fuel (21). The chemical form of nitrogen in coal is thought to be primarily heterocyclic aromatic ring structures such as pyridine, though this is difficult to ascertain, since removal of the nitrogen containing compounds from coal without their destruction is difficult. There are no data available for black liquor to show the chemical form of the fuel nitrogen, or to show how much is released during the respective stages of devolatilization and char burning.

Recovery Furnace NOx Emissions

Published data on NO_x emissions from recovery furnaces are somewhat limited. Table II provides a summary of reported NO_x emissions along with the sources of the data. Emission levels (adjusted to a common basis of ppm at 8% O_2 in flue gas) range from near zero to over 100 ppm. These emissions are relatively low when compared to NO_x emissions from coal, oil, and gas fired furnaces (22, 23) and illustrate why NO_x emissions from recovery furnaces have not been given as much consideration as NO_x emissions from other combustion sources.

II. Summary of published NO_x flue gas concentrations from kraft and NSSC recovery furnaces.

Source	% solids	(NO_x), units as reported	(NO_x), ppm @ 8% O2
Galeano and Leopold (1971)	NA[a]	0-53 ppm	33
Galeano and Leopold (1971)[b]	NA	13-65 ppm	35
Galeano, et al. (1973)[b]	62	10-50 ppm	30
Hood and Miner (1981)	NA	0.05-0.14 lb/10^6 BTU (data from 10 furnaces)	20-55[c]
Bjorklund, et al. (1989)	64.6[d]	95 ppm	73
Bjorkland, et al. (1989)	76.5[d]	155 ppm	120
Brannland, et al. (1990)	65.0	57 mg/MJ	60
Casale & Fritz (1990)	74.0	77 ppm (emission limitation)	77
Anderson and Jackson (1991)	NA	80 ppm (emission limitation)	80
IPST data (1991)	67.6[d]	70 ppm[e]	59
IPST data (1991)	67.9[d]	110 ppm[e]	91

a not available
b NSSC liquor
c based on approximate conversion factor of (390 ppm @ 8% O2)/(lb/10^6 BTU)
d before salt cake addition
e represents average of 6 to 10 one day tests

By considering those data in Table II for which liquor solids concentrations are available, a trend is apparent. These data (plotted in Figure 2) suggest that NO_x levels increased approximately four fold as solids increased from 62 to 77%. Some useful implications result from comparing this observed increase to that predicted for thermal NO formation. Integration of Equation 7 shows that for given values of O_2 and N_2 concentrations, temperature, and residence time, a four fold increase in thermal NO would require approximately a 40 °C increase in temperature. Yet it is likely that furnace temperatures increased by much more than 40°C for an increase in solids from 62 to 77%. Theoretical flame temperature estimations for black liquor combustion (24) show a 230 °C temperature increase over this range. Equation 7 and Figure 1 show an increase of thermal NO by a factor of several hundred for a 230 °C temperature increase.

2. NO_x emissions observed in flue gases from recovery furnaces, effect of increasing solids, all values normalized to a common basis of 8% O_2 in flue gas, sources of data as given in Table II.

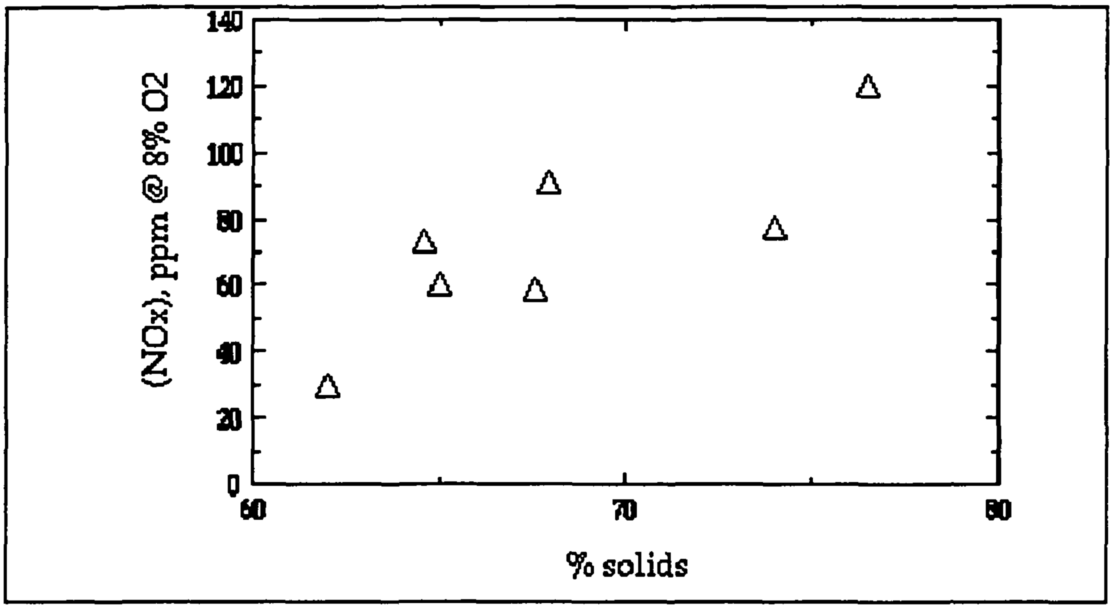

The fact that the observed temperature dependency is much less than approximated by thermal NO formation theory suggests that mechanisms other than thermal NO formation play an important role in determining recovery furnace NO_x emissions. Two possibilities are: 1) a substantial portion of the total recovery furnace NO originates as fuel NO which is not temperature sensitive, and 2) NO destruction reactions are occurring and tending to mask or partially mask the temperature dependency. The first of these possibilities has been discussed above. The second is discussed below.

NOx Destruction Reactions

Levels of NO emissions depend not only on the rate of formation of NO, but also on the rate of destruction. Once NO is formed, it can be partially destroyed before leaving the furnace. Measurements of NO profiles as a function of distance from the flame have been made in several instances (21, 25) in laboratory and pilot scale combustion. Results showed that NO is rapidly formed and then slowly destroyed. Concentrations pass through a maximum in or near the flame zone and undergo reduction in the post flame gases. The effluent or flue gas concentration does not necessarily represent the maximum level of NO concentration formed in the furnace. The reduction can be up to 50% or more of the maximum level reached in the furnace, with fuel rich flames and particle laden flames giving the most destruction, and fuel lean and homogeneous flames giving less destruction (25, 26).

This NO reduction is due partially to gas phase reaction of NO with nitrogen containing intermediates to form N_2 (as shown in Equation 8). The fact that the extent of NO reduction is greater in coal combustion than in gas or liquid combustion (26) showed that char and ash species are also responsible for NO reduction. Kinetic rates of reduction of NO to N_2 by chars have been measured (25-27). Rate expressions are generally reported in the form

$$f(-d(NO),dt) = A \exp [-E/(RT)] A_E (NO) \qquad (9)$$

showing the dependence on char external surface area (A_E), NO concentration, temperature, and residence time.

Returning to the apparent trend in Figure 2, it is possible that NO formation in the recovery furnaces increased by much more than four fold as solids increased from 62 to 77%, but that NO destruction due to air staging served to counter or dampen the increase such that only some of the increase was seen in flue gases. As discussed by Galeano and Leopold (22), the conventional kraft recovery furnace, in order to promote formation of sulfide, uses the concept of air staging which is coincidentally a proven method for reducing NO emissions from utility boilers. Less than stoichiometric air in the lower furnace will decrease thermal NO formation by decreasing concentrations of atomic oxygen, and will decrease conversion of fuel nitrogen to NO while increasing conversion to N_2 (as indicated by the overall pathway shown in Equation 8).

A destruction mechanism which may be especially important in recovery furnaces is the reaction of NO_x with fume species. Fume particulates represent a tremendously large surface area for reactions with gas phase species. Sulfur gases including oxides of sulfur are known to react with fume species. Oxides of nitrogen may also undergo similar reducing reactions. Several possible reactions of nitrogen oxides with sodium species have been suggested (28) based on thermodynamic feasibility. If such reactions are occurring, burning black liquor at higher solids concentrations and higher combustion temperatures may serve to increase the fuming rate, and increases in fume-NO_x interactions would counter the increases in thermal NO formation.

CONCLUSIONS/RECOMMENDATIONS

Recovery furnace NO_x is formed primarily by thermal and fuel NO formation mechanisms. Little to no data are available to show the relative importance of each in black liquor combustion. This is an important question to answer and identifies a strong research need since the temperature dependence is very different for each mechanism.

Thermal NO is highly temperature sensitive. Theory predicts that moderate increases in furnace temperature (100-140 °F or 55-80 °C) will yield order of magnitude increases in thermal NO concentrations. Due to this sensitivity, it can be concluded that the zones in the recovery furnace controlling thermal NO formation are those of highest average temperature.

Fuel NO is relatively temperate insensitive, and thus fuel NO in recovery furnaces is not expected to be affected by increasing solids concentrations. Black liquor solids contain 0.05 to 0.24 weight percent nitrogen, which represents a significant potential for fuel NO formation. The fact that fuel NO accounts for the majority of total NO in combustion of residual fuel oil containing nitrogen at a similar level to black liquors (0.2%) also suggests that fuel NO may be important in recovery furnaces.

No information is available concerning the chemical form of nitrogen in black liquors, or concerning how much is released during devolatilization versus during char combustion. This identifies a second research need, as this will affect when and where in the furnace the fuel nitrogen is released and will affect the relative distribution of NO and N_2 formed.

Published NO_x emissions data from operating recovery furnaces show values of near zero to over 100 ppm (@ 8% O_2), which are much lower than typical values from coal, oil, and gas combustion. The data show approximately a four fold increase in NO_x as solids increased from 62 to 77%. This increase is much less than predicted by the temperature dependence of thermal NO theory, suggesting the possibility that NO destruction reactions are occurring in recovery furnaces. This identifies a third area of research need, to evaluate the impact of potential NO_x destroying mechanisms.

FUTURE ACTIVITY

Combustion experiments will be performed at IPST using the black liquor combustion reactor, to determine the relative contributions of fuel NO and thermal NO for black liquor combustion. The percentage of total NO emissions that is formed by the oxidation of fuel bound nitrogen will be determined by replacement of the combustion air with a mixture of 21% oxygen in argon.

Work will be done to examine the destruction of NO_x by reactions in the furnace with other species, such as fume.

Experimental efforts will also be concentrated on the question of the form and the fate of nitrogen in black liquors. Some of the key questions to be answered here are where does the black liquor nitrogen come from (from nitrogen in wood, or from other sources in the pulping process), what is the chemical structure of the nitrogen containing compounds, and when during the combustion process is the nitrogen evolved (during devolatilization only, or during devolatilization and char combustion).

REFERENCES

1. Seinfeld, J. H. *Atmospheric Chemistry and Physics of Air Pollution.* John Wiley & Sons, New York, NY (1986).

2. Hood, K. T. A Study of Nitrogen Oxides Emissions From Kraft Recovery Furnaces. Technical Bulletin No. 105, National Council of the Paper Industry For Air and Stream Improvement (December 1979).

3. Hood, K. T., and Miner, R. A. NO_x Emissions From Combustion Sources in the Pulp and Paper Industry. Proc. 1981 Tappi Environmental Conference, TAPPI Press, 113-118 (1981).

4. State of Maine Department of Environmental Protection, Permit No. A-215-71-B-A/R, Georgia Pacific Corporation, Woodland, Maine, Issued April 12 (1989).

5. Barsin, J. A., Johnson, R. L., and Rissler, C. E. The St. Francisville Recovery Low Odor Conversion and Capacity Upgrade. Proc. 1989 International Chemical Recovery Conference, Ottawa, Ontario, 29-37 (1989).

6. Bjorklund, H., Warnqvist, B., and Pettersson, B. Inside a Kraft Recovery Boiler-Combustion of (High-Sulphidity) Black Liquor at High Dry Solids. Proc. 1989 International Chemical Recovery Conference, Ottawa, Ontario, 177-181 (1989).

7. Casale, F. S., and Fritz, P. A. Start Up and Operation of a High-Solids Recovery Boiler at S. D. Warren Company, Westbrook, Maine. Proc. TAPPI 1990 Engineering Conference, 687-688 (1990).

8. Hayhurst, A. N., and Vince, I. M. Nitric Oxide Formation From N_2 in Flames: The Importance of "Prompt" NO. *Progress in Energy and Combustion Science..* 6:35-51 (1980).

9. Zeldovich, J. The Oxidation of Nitrogen in Combustion and Explosions. *Acta Physiochimica U.R.S.S.* 21(4):577-628 (1946).

10. Bowman, C. T. Chemistry of Gaseous Pollutant Formation and Destruction, Chapter 4 of *Fossil Fuel Combustion: A Source Book.* Bartok, W., and Sarofim, A. F., editors, John Wiley & Sons, Inc., New York, NY (1991).

11. Anderson, P. H., and Jackson, J. C. An Analysis of Best Available Control Technology Options for Kraft Recovery Furnace NO_x Emissions. *Tappi Journal.* 74(1):115-118 (1991).

12. Nichols, K. M. Nitrogen Pollutant Formation in a High Pressure Entrained-Coal Gasifier. Ph. D. Dissertation, Chemical Engineering Department, Brigham Young University, Provo, UT (1987).

13. Boardman, R. D. Development and Evaluation of a Combined Thermal and Fuel Nitric Oxide Predictive Model. Ph. D. Dissertation, Chemical Engineering Department, Brigham Young University, Provo, UT (1990).

14. Fenimore, C. P. Reactions of Fuel-Nitrogen in Rich Flame Gases. *Combustion and Flame.* 26:249-256 (1976).

15. de Soete, G. G. Overall Reaction Rates of NO and N_2 Formation From Fuel Nitrogen. *Fifteenth Symposium (International) on Combustion.* 1093-1102 (1975).

16. Hill, S. C., Smoot, L, D., and Smith, P. J. Prediction of Nitrogen Oxide Formation in Turbulent Coal Flames. *Twentieth Symposium (International) on Combustion.* 1391-1400 (1984).

17. Pershing, D. W., and Wendt, J. O. L. Pulverized Coal Combustion: The Influence of Flame Temperature and Coal Composition on Thermal and Fuel NO_x. *Sixteenth Symposium (International) on Combustion.* 389-399 (1977).

18. Brannland, R. Norden, S., and Lindstrom, L. Implementation in full scale-the next step for Prenox. *Tappi Journal.* 73(5):231-237 (1990).

19. Pershing, D. W., Martin, G. B., and Berkau, E. E. Influence of Design Variables on the Production of Thermal and Fuel NO from Residual Oil and Coal Combustion. AIChE Symposium Series, No. 148, Vol. 71 pp. 19-29, (1975).

20. Pershing, D. W., Cichanowicz, J. E., England, G. C., Heap, M. P. and Martin, G. B. The Influence of Fuel Composition and Flame Temperature on the Formation of Thermal and Fuel NO_x in Residual Oil Flames. *Seventeenth Symposium (International) on Combustion.* 715 (1979).

21. Nichols, K. M., Hedman, P. O., and Smoot, L. D. Release and Reaction of Fuel-Nitrogen in a High-Pressure Entrained-Coal Gasifier. *Fuel.* 66(9):1257-1263 (1987).

22. Galeano, S. F., and Leopold, K. M. A Survey of Emissions of Nitrogen Oxides in the Pulp Mill. *Tappi Journal.* 56(3):74-76 (1973).

23. Galeano, S. F., Kahn, D. C., and Mack, R. A. Air Pollution: Controlled Operation of a NSSC Recovery Furnace. *Tappi Journal.* 54(5):741-744 (1971).

24. Adams, T. N., and Frederick, W. J. *Kraft Recovery Boiler Physical and Chemical Processes.* American Paper Institute, New York, NY (1988).

25. Wendt, J. O. L., Pershing, D. W., Lee, J. W., and Glass, J. W. Pulverized Coal Combustion: NO_x Formation Mechanism Under Fuel Rich and Staged Combustion Conditions. *Seventeenth Symposium (International) on Combustion.* 77-87 (1979).

26. Levy, J. M., Chan, L, K., Sarofim, A. F., and Beer, J. M. NO/Char Reactions at Pulverized Coal Flame Conditions. *Eighteenth Symposium (International) on Combustion.* 111-120 (1981).

27. Suuberg, E. M., Teng, H., and Calo, J. M. Studies on the Kinetics and Mechanism of the Reaction of NO with Carbon. *Twenty-Third Symposium (International) on Combustion.* 1199-1205 (1990).

28. Thompson, L. M. The Formation of Oxides of Nitrogen in Kraft Recovery Boilers. A390 Preparation For Research Problem, The Institute of Paper Science & Technology, Atlanta, GA (1990).

FUME FORMATION

Chris Verrill (IPST Ph.D. Candidate)
and
Kenneth M. Nichols

FUME FORMATION (C. Verrill, K. Nichols)

SUMMARY

Recent studies indicate that sodium evolution during drying and devolatilization of black liquor may produce a significant amount of the fume in an operating recovery furnace. In this investigation, single droplets of industrial black liquor were exposed to a flowing gas stream over a temperature range of 500 - 900°C. After 3 - 30 seconds in the pyrolytic environment, the char particles were withdrawn and quenched. Approximately 10 - 30% of the sodium present in the black liquor solids was released during drying and devolatilization. After swelling is complete, continued sodium release appears to occur only at temperatures above 800°C.

The mechanism of sodium loss during drying and devolatilization of black liquor may involve the vaporization of volatile organo-sodium compounds as well as the physical transport of alkali-containing material by eruptions of gases through the surface film of the pyrolyzing droplets.

INTRODUCTION

The inorganic aerosol generated during kraft black liquor combustion is known as fume. The submicron-sized fume particles consist primarily of Na_2CO_3, with Na_2SO_4, NaCl, and the analogous potassium salts. Fume composition varies with location in the recovery furnace and is dependent on the conditions of combustion.[1,2] Furnace dust samples and equilibrium calculations indicate that about 10% of the sodium in the black liquor is vaporized and becomes fume.[3] The principal benefit of fume formation is that the alkali aerosol reacts with environmentally undesirable sulfur gases in the flue gas; the resulting Na_2SO_4 dust is removed by the electrostatic precipitator and returned to the system by mixing with the black liquor. Fume has detrimental effects on recovery boiler operation because it deposits on the heat transfer surfaces which reduces thermal efficiency, requires process steam to remove the deposits, and contributes to blockage of air passages.

It is normally considered that there are four distinct stages of black liquor droplet combustion: drying, devolatilization, char burning, and inorganic reactions of the residual smelt.[4,5] Fume generation has historically been attributed to sodium vaporization during char burning and smelt reactions.[4,6] However, recent experimental data from the single droplet furnace at IPST, as well as data from other investigators[7,8,9] indicate that sodium emission occurs prior to char burning. These data show that sodium release during devolatilization may represent a significant portion (or even a majority) of overall fume formation.[9]

REVIEW OF PAST PROJECT ACTIVITY

Previous efforts were focused on design, construction, and validation of an experimental furnace and fume collection assembly for the purpose of burning a single droplet of black liquor and collecting inorganic emissions on a filter.[10] The filter was mounted on a platform which moves during the droplet combustion, so that the fuming rate and composition can be correlated with the combustion events occurring in a droplet: namely; drying, pyrolysis, and char combustion. The furnace was demonstrated at operating conditions of 600 - 900°C and mean gas velocities of 0.30 - 1.5 m/s. Successful operation of the moving filter assembly was demonstrated. Numerous (approximately 40) droplet combustion trials were conductged with two industrial liquors. Several problems with filter rupture and with inaccurate determination of filter weight were encountered and dealt with.

DISCUSSION OF 1991 RESULTS

Experimental

Individual droplets of an industrial kraft black liquor, weighing 2 to 10 mg, were formed on nichrome wire hooks and inserted into the quartz reaction chamber of the droplet furnace. A constant average gas velocity in the quartz reaction chamber of 0.61 m/sec was maintained by adjusting the gas flow rate. After 3 to 30 seconds, the char was withdrawn from the pyrolytic environment into the quench stream and allowed to cool. Observation of droplet pyrolysis in the furnace was recorded on video tape.

Times for drying and swelling were calculated from the elapsed time indicated on the video tapes of the liquor pyrolysis trials. The first appearance of the droplet in the field of view was used to denote the start of drying; the first sign of swelling indicated the onset of devolatilization; the maximum swollen volume of the char particle was taken as the end of devolatilization. These times do not correspond exactly with the drying and devolatilization stages, because there is almost always some overlapping of the stages during droplet combustion.[11]

Results

Droplet Pyrolysis Behavior

A large number of droplet burns (more than 450) were performed with one black liquor. To illustrate the behavior during pyrolysis of the droplets, drying times versus initial droplet mass are shown in Figure 1, and Figure 2 is a plot of swelling time versus the calculated mass of droplet solids. The gas composition was 5% CO and 95% N_2 for all cases except for the 500°C data where it was 5% O_2 and 95% N_2. Simple linear regression models were used to group the data in Figures 1 and 2; these lines do not imply that statistical correlation exists between the variables. The mean liquor solids content during the second experiment at 600°C was somewhat lower than in the other experiments; accordingly, the mean drying times were longer, as indicated in Figure 1.

Both the drying and devolatilization times were reduced by increasing furnace temperature, though the effect was more pronounced for drying. Average drying times were 5.8 and 0.9 seconds at 500°C and 900°C respectively; while average pyrolysis times were 2.8 and 1.2 seconds at these two temperatures.

Mass Loss During Pyrolysis

Total char mass losses for all experiments are plotted against exposure time in Figure 3. Char mass loss is defined as percent difference between the initial mass of liquor solids and the mass of residue (from the droplet) remaining after exposure in the furnace. The initial mass of liquor solids was calculated from the sum of each droplet's measured mass and the solids content of the black liquor. To account for evaporation loss, the solids content was determined periodically during each experiment. No significant char mass loss is expected to occur until the particles begin to swell; accordingly, average drying times were used as origins of the curves in the Figure 3. Lines are shown in the figure to group the data; they are not based on statistical regression.

The apparent increase in mass during pyrolysis at 900°C is a result of partial oxidation of highly reduced char immediately upon removal from the quench stream. This conclusion is supported by the observation of spontaneous combustion exhibited by many of these char particles when they were removed from the nitrogen quench and exposed to ambient laboratory air. Micrographs of several intact char particles, pyrolyzed at 900°C for 30 seconds, reveal changes in morphology, that indicate that all highly reduced particles underwent rapid oxidation after being removed from the furnace.

It is interesting that the ultimate mass losses for the low temperature trials, shown in Figure 3, are very similar despite the difference in gas composition. There were, however, substantial differences in char formation observed at the two conditions. The swelling behavior of droplets exposed to 95% N_2 with 5% O_2 at 500°C was like that observed during combustion at higher temperatures and oxygen concentrations.[10] These droplets underwent random serpentine expansion and formed hollow char particles with delicate but resilient external films.. Particles produced in 95% N_2 with 5% CO at 600°C were porous and brittle with more internal structure. The swelling of these particles during devolatilization was uniform and spherical.

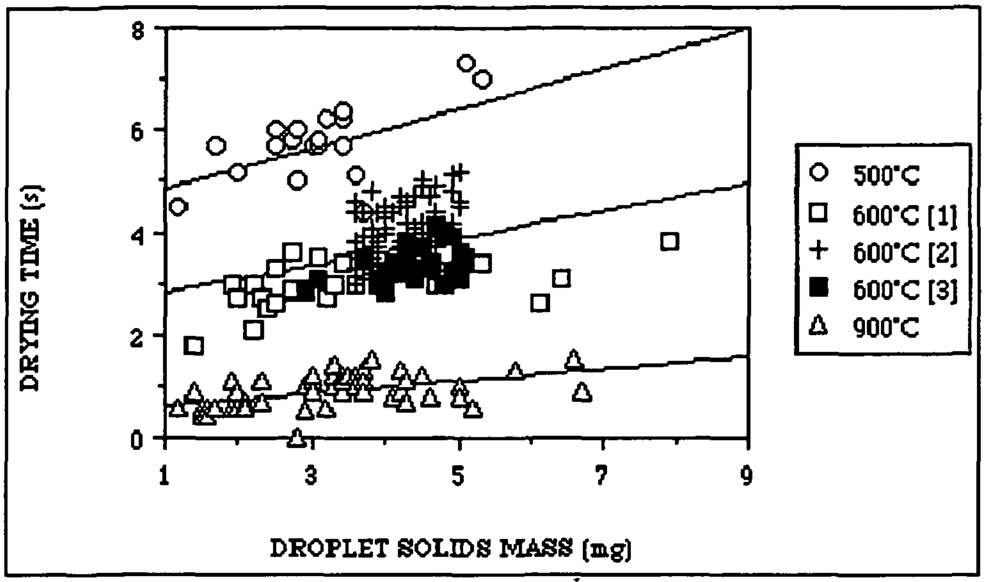

Figure 1. Drying time during droplet pyrolysis

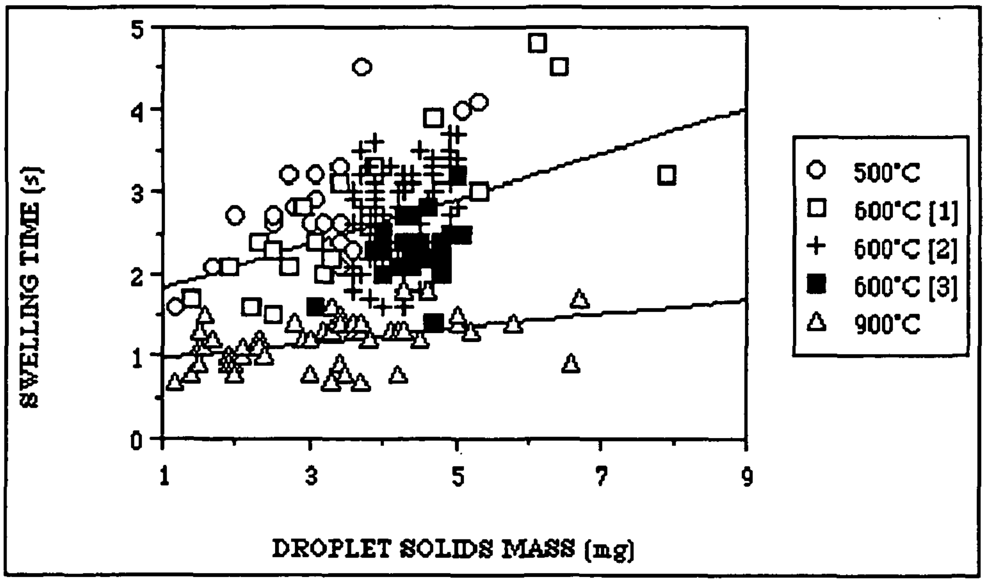

Figure 2. Devolatilization time during droplet pyrolysis

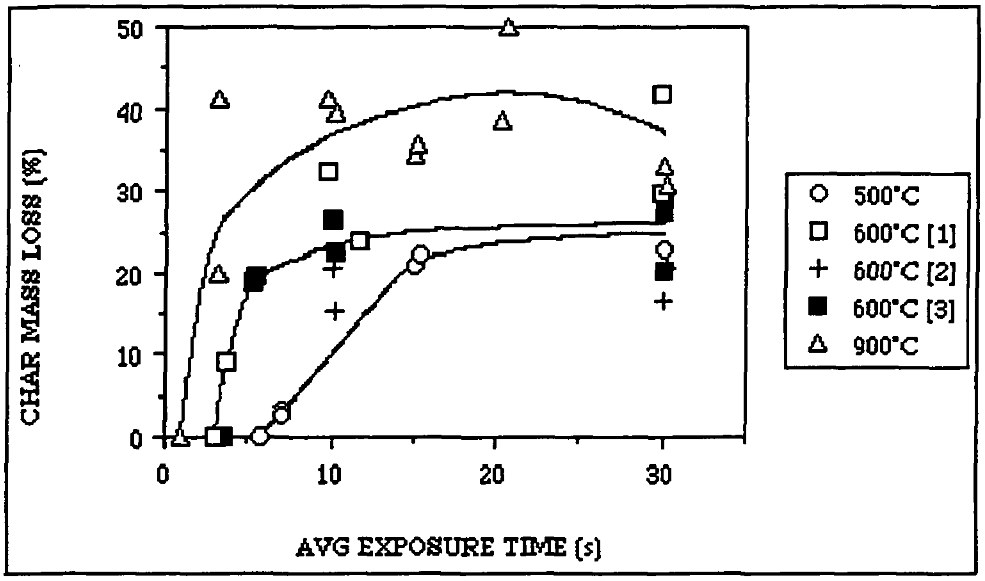

Figure 3. Char mass loss during pyrolysis

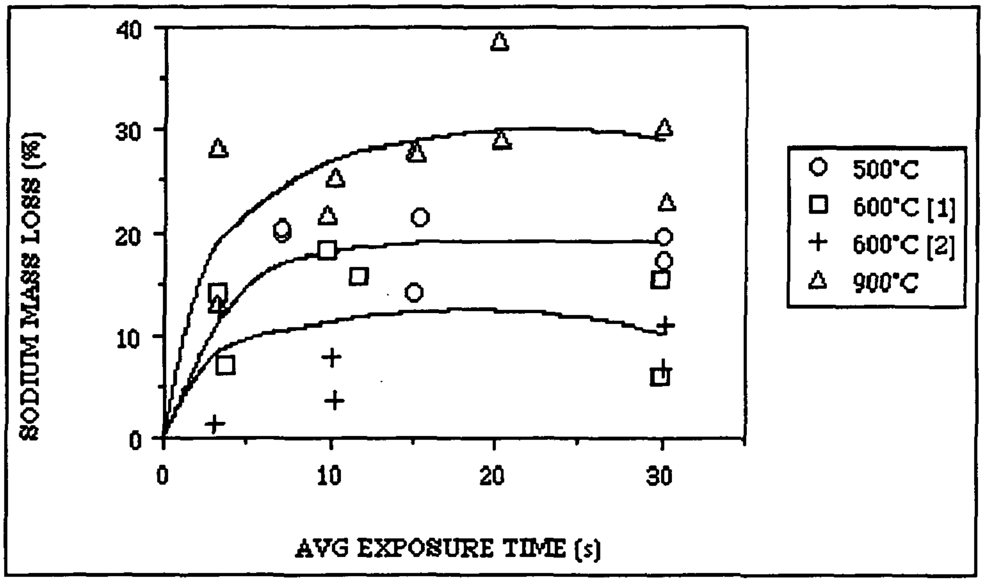

Figure 4. Sodium mass loss during pyrolysis

Sodium Mass Loss During Pyrolysis

The amounts of sodium remaining in the char are plotted versus exposure time in Figure 4. Note that the experiments at 600°C and 900°C were conducted in an atmosphere of 5% CO in 95% N_2; the carrier gas contained 5% O_2 during the 500°C experiment. Because there was significant sodium loss at the shortest exposure times in all experiments, the origin of the curves in Figure 4 were not assumed to be at the average drying time, as in Figure 3. The moisture content of the char samples would not affect the accuracy of these results because the sodium was determined from the concentration of a dissolved sample.

The data in Figure 4 indicate that, for all conditions, there is a rapid initial loss of approximately 10 - 30% of the sodium in the black liquor solids. The significant change in sodium mass at the shortest exposure times suggests that sodium evolution may be occurring during drying. After swelling is complete, sodium loss appears to continue only during pyrolysis at 900°C. Frederick and Hupa[9] presented curves which indicated similar behavior of sodium loss during pyrolysis of black liquor droplets in 95% N_2 with 5% CO at 700 - 800°C.

From Figure 4, it is apparent that about 10% of the sodium was evolved during the first 10 seconds of pyrolysis at 600°C, and about 25% of the sodium was evolved during the first 10 seconds at 900°C. Frederick and Hupa[9] reported average sodium mass losses of 23 - 33% during pyrolysis of 8 - 20 mg droplets of five kraft liquors for 10 seconds at 800°C. Within experimental error, good agreement exists between their data and the sodium losses indicated in Figure 4. Li and van Heiningen[8] conducted a thermogravimetric study of sodium evolution during kraft liquor char pyrolysis at a heating rate of 20°C/min. They reported 18% sodium mass losses after exposure to 88% He with 12% CO at 750 - 800°C for 30 minutes.[8] These values agree remarkably well with those of both droplet studies despite two orders of magnitude difference in the heating rates.

A comparison of the mass loss in the environment of 95% N_2 with 5% O_2 at 500°C with the 600°C data reveals significant differences in sodium emission during devolatilization between inert and oxidative environments. After exposure to the low temperature oxidative atmosphere for 7 seconds, approximately 19% of the sodium had evolved from the partially swollen char. Char particles withdrawn from the inert environment at 600°C after 3 seconds had swollen to approximately the same extent, but the mass of sodium had only decreased by 9%.

In a related combustion study, Volkov et al.[17] exposed droplets of kraft black liquor to oxidizing conditions over a temperature range of 900 - 1100°C. Char residue was extracted through a nitrogen quench after a fixed exposure time. The total sodium evolved during combustion ranged from 30 - 50% of the sodium present in the liquor. At the minimum exposure time of three seconds, they reported a 20% sodium loss for 2 mm diameter droplets burnt in air at 900°C.[7] Model predictions indicate that drying and devolatilization of similar-sized droplets in air at 800°C would be complete in about three seconds;[12] therefore, it is likely that part or all of the initial sodium loss reported by Volkov occurred before char combustion commenced.

The Fate of Sodium During Pyrolysis

Two mechanisms are being considered to explain sodium loss before black liquor char combustion begins: vaporization of volatile alkali compounds and physical transport of alkali-containing material.

Elemental sodium and NaCl are the most volatile inorganic species, the vapor pressure of other sodium salts are very low, even at 900°C.[12] It is unlikely that the sodium evolves as NaCl during devolatilization because chlorine has been found to volatilize as HCl at relatively low temperatures from pulverized coal.[13] The particle temperature may be high enough to produce a vapor pressure of elemental sodium during devolatilization and swelling; however, this would not explain the sodium loss during drying. It is proposed that, if vaporization is the mechanism of sodium loss, the fugitive sodium must be associated with volatile organic compounds that are stable at the temperatures of droplet drying and devolatilization. If a relatively low molecular weight organic sodium compound had a substantial vapor pressure at 200°C, then it could easily be swept from the boundary layer surrounding the devolatilizing particle into the bulk phase where it would be decomposed to pyrolysis gases and volatile sodium (Na or NaOH).

During the first observations of spent pulping liquor droplet combustion in laboratory furnaces, researchers noted that the droplets bubbled violently during drying as water vapor erupted through a surface film.[4,14] Bubble formation and erupting jets of gases were also observed in high speed photographic images of pyrolyzing coal particles.[15] When Miller[16] investigated the swelling of kraft black liquor, he found behavior similar to that of coal; bubbles began to form when the liquor solids were heated to 250°C. Smith et al.[17] proposed that bursting fly ash particles are responsible for a large fraction of the submicron-sized aerosol formed during pulverized coal combustion. They explained that gas evolution during rapid heating causes the slag films surrounding fly ash particles to burst which liberates volatile substances that subsequently condense as fume.[17] Raask[18] observed that some particles were ejected during slag film rupture, but indicated that very few submicron-sized particles were formed as a result of these gas explosions.

The physical transport of sodium-containing material explains sodium loss during both drying and devolatilization. The eruptions of water vapor and pyrolysis gases from the surface film of the liquor droplets eject tiny droplets of liquor into the gas phase surrounding the particle. Under non-combustive conditions, the organic alkali compounds in the ejecta would be rapidly decomposed to low molecular weight gases and sodium carbonate aerosol. If the gaseous environment supports combustion, then the mechanisms of char during and sulfide oxidation, discussed in the introduction, would produce sodium vapor from the burning bits of ejected liquor. The sodium vapor would further react and condense as submicron-sized fume.

CONCLUSIONS

Approximately 10 - 30% of the sodium present in the black liquor solids is released during drying and devolatilization of single droplets of black liquor. After swelling is complete, continued sodium release appears to occur only at higher temperatures above 800°C, additional sodium may then evolve as a result of thermal decomposition of Na_2CO_3.

Sodium mass loss during pyrolysis in 95% N_2 with 5% CO is a strong function of furnace temperature. The remarkable agreement between Volkov's data for combustion in air at 900°C and the sodium loss results from the experiment at 500°C in 95% N_2 with 5% O_2 suggests that the effect of temperature on sodium release during devolatilization may be attenuated by the presence of oxygen. The physical behavior of char during pyrolysis is also greatly affected by the gas composition.

Sodium loss during black liquor drying and devolatilization probably involves the vaporization of volatile organo-sodium compounds as well as the physical transport of alkali-containing material by eruptions of water vapor and pyrolysis gases through the surface film of rapidly heated droplets.

FUTURE ACTIVITY

In order to understand the nature of sodium evolution during drying and devolatilization, experiments will be performed to investigate the effects of process variables on the rate of sodium loss. If the alkali release is a result of physical ejection of sodium-containing material, then the particle heating rate should affect the extent of sodium loss. Liquor composition should have a similar effect, if vaporization of sodium compounds is responsible for fume formation during the initial stages of black liquor droplet combustion.

REFERENCES

1. Tran, H. How does a kraft recovery boiler become plugged? Tappi Kraft Recovery Operations Seminar Notes. Orlando, FL, January 22-27, 1989:183-191.

2. Rizhinshvili, G.V.; Kaplun, L.V. Bumazh. Prom. (1):26-28(1983).

3. Borg, A.; Teder, A.; Warnqvist, B. Tappi 57(1):126-129(1974).

4. Hupa, M.; Solin, P.; Hy_ty, P. Combustion behavior of black liquor droplets. Proceedings of the TAPPI/CPPA International Chemical Recovery Conference. New Orleans, LA, April, 1985:335-344.

5. Grace, T.M.; Cameron, J.H.; Clay, D.T. Char Burning, Project 3473-6 Summary Technical Report. Appleton, WI, The Institute of Paper Chemistry, 1985.

6. Lang, C.J.; DeHaas, G.G.; Gommi, J.V.; Nelson, W. Tappi 56(6):115-119(1973).

7. Volkov, A.D.; Evseev, O.D.; Ibatullina, R.I.; Dravolina, E.I. Mezhuz. Sb. Nauchn. Tr. Ser. Khim. Tekhol. Tsellyul. (7):72-75(1980).

8. Li, J.; van Heiningen, A.R.P. Tappi 73(12):213-219(1990).

9. Frederick, W.J.; Hupa, M. Tappi 74(11):192-194(1991).

10. Verrill, C.L. Inorganic Aerosol Formation During Kraft Black Liquor Droplet Combustion. Ph.D. thesis in progress. Atlanta, GA, The Institute of Paper Science and Technology, 1992.

11. Frederick, W.J. Combustion Processes in Black Liquor Recovery: Analysis and Interpretation of Combustion Rate Data and an Engineering Design Model. Report No. One for U.S. Dept. of Energy, DOE/CE/40637-T8 (DE90012712), March, 1990.

12. Adams, T.N.; Frederick, W.J Kraft Recovery Boiler Physical and Chemical Processes. The American Paper Institute, New York, 1988.

13. Srinivasachar, S.; Helble, J.J.; Ham, D.O.; Domazetis, G. Prog. Energy Combust. Sci. 16:303-309(1990).

14. Monaghan, M.T.; Siddall, R.G. Tappi 46(2):89-91(1963).

15. Oh, M.S.; Howard, J.B.; Peters, W.A. Modeling volatiles trasport in softening coal pyrolysis. AIChE Ann. Mtg. Nov. 25-30, 1984, San Fransico, CA.

16. Miller, P.T.; Swelling of kraft black liquor. An understanding of the associated phenomena during pyrolysis. Ph.D. Dissertation. Appleton, WI, The Institute of Paper Chemistry, 1986.

17. Smith, R.D.; Campbell, J.A.; Nielson, K.K. Atmos. Environ. 13:607-617(1979).

18. Raask, E. J. Inst. Energy:231-239(1984).